Title
An Exploration of Quantum Materials: From Topological Semimetals to Antiferromagnetic Memory

Author
Nair, Nityan L.

Publication Date
2019

Peer reviewed|Thesis/dissertation

An Exploration of Quantum Materials: From Topological Semimetals to Antiferromagnetic Memory

by

Nityan L. Nair

A dissertation submitted in partial satisfaction of the

requirements for the degree of

Doctor of Philosophy

in

Physics

in the

Graduate Division

of the

University of California, Berkeley

Committee in charge:

Professor James G. Analytis, Chair
Professor Joseph Orenstein
Professor Junqiao Wu

Fall 2019

An Exploration of Quantum Materials: From Topological Semimetals to Antiferromagnetic Memory

Abstract

An Exploration of Quantum Materials: From Topological Semimetals to Antiferromagnetic Memory

by

Nityan L. Nair

Doctor of Philosophy in Physics

University of California, Berkeley

Professor James G. Analytis, Chair

This dissertation presents the results of several research projects on condensed matter systems that fall within the broad scope of quantum materials. These are compounds which possess emergent phenomena that would not be expected from conventional solid state theory. These include the topological semimetals Cd_3As_2, TaAs, and $ZrTe_5$, as well as the frustrated antiferromagnet $Fe_{1/3}NbS_2$. In Cd_3As_2, a Dirac semimetal, focused ion beam microstructured devices were found to exhibit a new type of coherent electron orbit. This "Weyl orbit" involves the Fermi arc surface states. Although these states are a necessary consequence of the topological nature of Cd_3As_2, they had not previously been observed in electronic transport. In the Weyl semimetal TaAs, the same focused ion beam microstructuring techniques were found to induce superconductivity on the device surface due to the differential sputtering of tantalum and arsenic. Instead, mechanical polishing techniques were used to thin devices in order to observe signatures of surface-driven transport, likely stemming from Fermi arc states as well.

In $ZrTe_5$, magnetization and magnetic torque measurements found a paramagnetic to diamagnetic crossover at the quantum limit magnetic field. This is the result of charge carriers entering a chiral, zeroth Landau level pinned at zero energy. This is a direct consequence of a topological band crossing, and therefore points to $ZrTe_5$ as a Dirac semimetal. A possible transition out of this topological phase was also observed as a function of temperature.

Finally, at sufficiently low temperatures and high current densities, $Fe_{1/3}NbS_2$ was found to be a switchable antiferromagnet. A spin transfer torque produced by an applied current was found to rotate the antiferromagnetic order. The rotation of these moments is reflected in the anisotropic magnetoresistance, changing the resistance of the device. In this manner, microstructured devices of $Fe_{1/3}NbS_2$ form an antiferromagnetic memory bit with electronic write-in and read-out. The low current densities involved and tunability of the device response point to $Fe_{1/3}NbS_2$ as a promising platform for antiferromagnetic spintronics.

Contents

List of Figures

List of Tables

Acknowledgments

There are many people I need to thank for helping me get to this point. Ph.D. programs are challenging and long and without the appropriate mentoring and support, they are impossible. First and foremost, I need to thank my family: my mom, my dad, and my brother. They always believed in me even though I did not always believe in myself. Your support over the past six years has meant more to me than you know.

Of course, I need to thank my advisor, Professor James Analytis. Without him the research presented in this dissertation would not have been possible. Under his supervision I learned the challenges and rewards of building a new laboratory, and the opportunities and risks of embarking on new research directions. He always remained positive, even when research projects did not go as planned. Thank you for guiding me through this process, and showing me the endlessly fascinating field of quantum materials.

I would also like to thank Professor Philip Moll, who was a postdoc in the Analytis group during the early stages of my graduate studies. Philip taught me many experimental techniques, including focused ion beam fabrication which would become a cornerstone of my research. More importantly, however, he taught me how to be a good scientist, how to find engagement in any project, and that the details matter. Thank you for your mentorship over the years and your patience as I destroyed countless FIB devices.

Science is never done in a vacuum and the research environment is as important as the researcher. I want to thank the students and postdocs of the Analytis group for creating an intellectually stimulating environment in which to discover new physics, new experimental techniques, and old equipment. I have truly enjoyed sharing a single office with all of you. Thank you for the long discussions, the late nights, and the beers.

Finally, I need to thank my friends, both old and new, within the university and without. Thank you for all the adventures and making the Bay such a memorable place to live.

Chapter 1

Introduction

The term quantum materials encompasses many different condensed matter systems in which quantum mechanical effects give rise to new emergent phenomena that would not be expected from the conventional theory of solids. This includes materials in which topological order is present, magnetic systems with strong correlations and frustrations, and strongly correlated materials which cannot be described using a single particle bandstructure. This dissertation will deal primarily with the first two: topological materials in which topological order parameters lead to phase transitions outside of the standard paradigm of broken symmetries, leading to phenomena such as protected surface states and chiral Landau levels, and frustrated antiferromagnetic materials in which complex interactions with conduction electrons allow for the manipulation of the antiferromagnetic order and subsequent storage of information. These two branches of condensed matter physics are unified by the experimental techniques used to probe them. Their emergent physics, in this work, has been pursued using similar electronic transport measurements and device microfabrication techniques.

Micro- and nanofabrication have proven to be incredibly useful, not just in producing devices for integrated circuits, but in pursuing new phenomena in condensed matter physics. In 1972 Philip W. Anderson published a paper titled "More Is Different", in which he discussed the role of emergent phenomena [1]. In short, understanding the behavior of a single particle, atom, or individual, is not equivalent to understanding the behavior of a macroscopic collective. Although both obey the same fundamental laws, the collective may show new emergent phenomena that are difficult, if not impossible, to predict. Superconductivity is one such famous example.

More than a decade earlier, Richard P. Feynman gave a talk titled "There's plenty of room at the bottom" in which he advocated for the miniaturization of devices and machines [2]. He envisioned new techniques that would enable scientists to directly manipulate atoms. This would allow for the creation of new materials and devices on scales previously not thought possible, and miniaturization of everything from computers to information to motors.

The devices fabricated and measured in this dissertation fall between these two limits. They are large enough that they maintain the emergent phenomena associated with their large numbers of atoms, such as topological surface states and antiferromagnetism. By fabri-

cating them down to the small length scales, however, those properties can be observed and manipulated in ways not possible at the macroscopic level. These observations are performed through standard electronic transport measurements. Applying electrical currents and detecting voltages on a sample can measure properties such as electrical resistance, providing an understanding of how charge carriers move through the material as a function of magnetic field, temperature, device geometry, etc. Although a very simple and straightforward measurement, it is amazing how much information can be extracted. Carrier densities and types, Fermi surface shapes, magnetic orders, and so on can be understood. Extracting these values from device resistivities is discussed in Chapter 1. The microscopic device fabrication was primarily done using focused ion beam fabrication techniques and is discussed in detail in Chapter 3.

In topological materials, introduced in Chapter 2, these techniques were used to observe the presence of surface states in Cd_3As_2 and TaAs, a Dirac and Weyl semimetal, respectively [3, 4]. Thinning the materials to the micrometer scale significantly enhances the surface-to-bulk ratio. This allows surface states to carry a larger proportion of the current, increasing their contribution to the overall transport, making their experimental signatures more easily resolvable. Moreover, it allows for interactions between states on opposite surfaces of a device. In Cd_3As_2, this led to the discovery of a new quantum orbit and associated resistivity oscillations involving the topological Fermi arc surface states, as discussed in Chapter 4 [3].

In TaAs, the same microfabrication techniques caused the surface of the device to become superconducting due to an excess of tantalum [5]. Modifying the fabrication process to make use of mechanical polishing techniques overcame this difficulty, and, in sufficiently thin samples, two dimensional quantum oscillations and an anomalous thickness dependence were observed. These indicate the presence of Fermi arc surface states and is discussed in Chapter 5 [4].

$ZrTe_5$ is a material that has been alternately shown to be topological and trivial, leading to some ambiguity. Bulk magnetization and magnetic torque measurements making use of the unique Landau level quantization spectrum of topological Dirac semimetals found a transition between paramagnetic behavior below the quantum limit to diamagnetic behavior above. In general, this would not be expected from conduction electrons in a non-magnetic system. The origins of this can be traced to the chiral Landau level in Dirac semimetals pinned at zero energy. The magnetization and magnetic torque measurements therefore point to $ZrTe_5$ as being a topological Dirac semimetal, albeit with a complicated bandstructure and possible topological phase transition. $ZrTe_5$ is discussed in Chapter 6 [6].

In the frustrated antiferromagnet $Fe_{1/3}NbS_2$, microfabrication was used to create multi-contact devices and increase current densities by decreasing device cross-sections. At these large current densities, the conduction electrons exert a spin transfer torque on the local iron moments, reorienting the antiferromagnetic order at low temperature. The ordering direction of the Néel vector can be read out via the device resistance. In this manner, $Fe_{1/3}NbS_2$ forms a fully electronically-accessible magnetic memory bit. Electronically-accessible magnetic memory storage, especially in antiferromagnets, has significant application in commercial devices, making $Fe_{1/3}NbS_2$ a very promising platform. Antiferromagnets are predicted

to have faster switching times, reduced crosstalk, and increased resilience to magnetic perturbations compared to ferromagnets, in addition to being non-volatile. The details of this switching behavior are discussed in Chapter 7 [7].

Quantum materials represent the forefront of research in condensed matter and modern microfabrication techniques allow their properties to be rapidly explored. New emergent phenomena such as topological surface states and antiferromagnetic switching are not only interesting from a basic science perspective, but promise device applications in areas such as quantum computing and memory storage. Harnessing the capabilities of quantum materials will allow researchers to answer fundamental physical questions and make devices for the 21st century.

1.1 Semiclassical motion of electrons in magnetic fields

Measuring the response of electrons to electric and magnetic fields can be extremely useful to understanding their behavior and interactions at the microscopic level. This class of measurements is called electronic transport and has proven to be extremely useful in exploring new materials. Among other things, transport measurements can be used to determine charge carrier densities and types, measure Fermi surface structure, observe many-body quantum mechanical states, and ascertain topological character.

When an electric field is applied to charge carriers in a metal, they will be accelerated along the field direction. Scattering events, however, will cause momentum to be dissipated into the lattice. Averaging over scattering events, gives the charge carriers an overall drift velocity defined by $\vec{v} = \mu\vec{E}$, where μ is the carrier mobility. This makes the current density, $\vec{j}$, directly proportional to the applied electric field, $\vec{j} = \overleftrightarrow{\sigma}\vec{E}$, where $\overleftrightarrow{\sigma}$ is the conductivity tensor. This is Ohm's law and can be alternatively written in terms of the resistivity tensor, $\overleftrightarrow{\rho}$, the inverse of the conductivity tensor.

In a time reversal symmetric system, $\overleftrightarrow{\sigma}$ will be a symmetric tensor. The breaking of time reversal symmetry, such as by the application of a magnetic field, will introduce antisymmetric off-diagonal components to the conductivity tensor. This is the Hall effect and is given by $\rho_{xy} = \pm B/ne$ in a single-band system, where B is the magnetic field, n is the carrier density, e is the electron charge, and $\pm$ is for holes and electrons, respectively.

As can be seen, magnetic fields can be useful in determining the carrier density and type in a metal via the Hall effect. At large magnetic fields, however, quantum mechanical effects become apparent and transport measurements can be used to extract information about the shape of the Fermi surface and nature of quasiparticle excitations.

Charge carriers in a crystal lattice under the influence of electric and magnetic fields are

governed by the following equations of motion:

$$\hbar\frac{\partial\vec{k}}{\partial t} = e\left[\vec{E} + \vec{v}\times\vec{B}\right] \tag{1.1}$$

$$\frac{\partial\vec{x}}{\partial t} = \vec{v} = \frac{1}{\hbar}\vec{\nabla}_k\varepsilon(\vec{k}) \tag{1.2}$$

where $\vec{k}$ is the wavevector associated with the crystal momentum, $\vec{E}$ and $\vec{B}$ are applied electric and magnetic fields, and $\vec{v}$ is the band velocity. In the presence of a constant magnetic field, Eq. 1.1 shows that charge carriers will move in a trajectory perpendicular to the applied field and band velocity. Given that the band velocity is proportional to the gradient of the band energy, particles will travel on trajectories that map out constant-energy contours of the electronic Fermi surface in a plane normal to the magnetic field.

In free space, this describes a circular cyclotron orbit. In a crystal lattice, this will take on the more complex cross-sectional shape of the Fermi surface. In either case, the total amount of time, T, to complete an orbit is found by integrating Eq. 1.1

$$T = \oint \frac{dk}{\partial k/\partial t} = \oint \frac{\hbar}{ev_\perp B}dk \tag{1.3}$$

where $v_\perp$ is the component of the band velocity perpendicular to the magnetic field. Inserting Eq. 1.2 allows the integral to be performed and yields an expression for the period of a cyclotron orbit, which can then be inverted to find the cyclotron frequency, ω_c.

$$\omega_c = \frac{2\pi}{T} = \frac{2\pi eB}{\hbar^2}/\left(\frac{\partial A_k}{\partial\varepsilon}\right) \tag{1.4}$$

where A_k is the area of the cyclotron orbit in k-space. Given that the cyclotron frequency is $\omega_c = eB/m$ in free space, Eq. 1.4 provides an expression for an effective mass

$$m^* = \frac{\hbar^2}{2\pi}\frac{\partial A_k}{\partial\varepsilon} \tag{1.5}$$

Particles in a lattice will behave as their free space counterparts with a modified effective mass, m^*. Note, this is the cyclotron effective mass and may differ from the band effective mass defined as $m^* = \hbar^2(\partial^2\varepsilon/\partial k^2)^{-1}$.

In any real crystal lattice, impurities and phonons are present that will act to scatter charge carriers and relax momentum to the lattice. Assuming that the scattering events are isotropic and act to relax the charge carrier's crystal momentum back to its field-free, thermal value, the scattering can be parameterized by a characteristic time scale τ. Eq. 1.1 can then be modified to incorporate τ as

$$\hbar(\frac{\partial}{\partial t} + \frac{1}{\tau})\vec{k} = e\left[\vec{E} + \vec{v}\times\vec{B}\right] \tag{1.6}$$

In steady-state, with the application of a constant electric and a magnetic field along the $\hat{z}$-direction, this equation can be solved for the conductivity tensor

$$\overleftrightarrow{\sigma} = \frac{ne^2\tau}{m^*}\frac{1}{1+(\omega_c\tau)^2}\begin{bmatrix} 1 & \omega_c\tau & 0 \\ \omega_c\tau & 1 & 0 \\ 0 & 0 & 1+(\omega_c\tau)^2 \end{bmatrix} \tag{1.7}$$

The conductivity tensor can be inverted to find the resistivity tensor. Note, however, that in this simple treatment, there will be no magnetoresistance in ρ_{xx} due to the perfect compensation of the off-diagonal elements. A more rigorous derivation involving more realistic anisotropic scattering would yield the quadratic magnetoresistance, $\rho_{xx} \propto B^2$, typically observed in metallic systems [8, 9].

1.2 Landau levels

In the presence of strong magnetic fields, electrons can no longer be treated semiclassically, and must instead be treated as quantum mechanical objects. The periodic circular motion of electrons in the plane normal to the magnetic field imposes a requirement that the orbit accumulate a phase which is an integer multiple of 2π, otherwise the electron wavefunctions will destructively interfere. This requirement leads to the quantization of allowed energy states into Landau levels. A more complete derivation can be found in [10].

For a parabolic band, the exact energy spacing of the Landau levels is given by

$$\varepsilon_n = \hbar\omega_c(n+1/2) + \frac{\hbar^2 k_\parallel^2}{2m^*} \tag{1.8}$$

where $\omega_c = eB/m^*$ is the cyclotron frequency, $k_\parallel$ is the component of the wavenumber parallel to the applied field, m^* is the effective mass, and ε_n is measured from the band bottom. Figure 1.1 shows the transformation of this spherical Fermi surface into a series of Landau tubes in the presence of a magnetic field. These energy levels will have a degeneracy per unit area of $D = eB/2\pi\hbar$.

In two dimensions, $k_\parallel = 0$ and Landau quantization leads to the quantum Hall effect [11]. In three dimensions, Landau quantization transforms an otherwise spherical Fermi surface into a series of cylinders parallel to the direction of the applied magnetic field. As these cylinders are pushed through the Fermi level, sharp changes in the density of states cause oscillations periodic in inverse magnetic field in many material parameters. When observed in magnetization this is the de Haas-van Alphen (dHvA) effect. When observed in resistivity, this is the Shubnikov-de Haas (SdH) effect.

To see that these oscillations are periodic in inverse field, consider the n^{th} Landau level as it passes the Fermi energy, ε_F. Its passage through the Fermi energy will lead to a drop in the density of states, which manifests in magnetization and transport measurements as an oscillation. The passage of the $(n-1)^{th}$ Landau level will similarly lead to an oscillation.

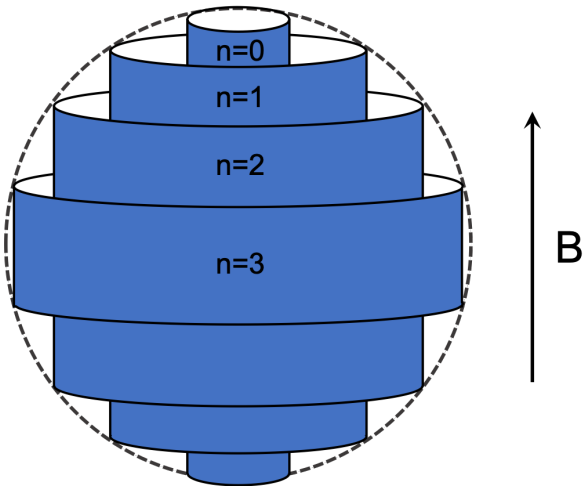

Figure 1.1: **Landau level quantization.** In the presence of a magnetic field, an otherwise spherical Fermi surface becomes quantized into Landau tubes parallel to the field direction. As the field is increased these tubes are pushed out of the Fermi surface, leading to quantum oscillations. The Landau level indices are labelled.

The period of these oscillations is given by the difference in the fields at which they pass through the Fermi level.

$$\varepsilon_n = \frac{\hbar e}{m^*} B_n(n + 1/2) = \varepsilon_F \quad , \quad \varepsilon_{n-1} = \frac{\hbar e}{m^*} B_{n-1}(n - 1/2) = \varepsilon_F \tag{1.9}$$

where $\varepsilon_F = \hbar^2 k_F^2/(2m^*) = \hbar^2 A_k/(2\pi m^*)$ for a parabolic dispersion, and A_k is the extremal cross-sectional area of the Fermi surface normal to the field direction. Solving the above system of equations yields the familiar Onsager relation for quantum oscillations periodic in inverse magnetic field,

$$\Delta\left(\frac{1}{B}\right) = \frac{1}{B_{n-1}} - \frac{1}{B_n} = \frac{2\pi e}{\hbar A_k} \tag{1.10}$$

$$F = \frac{\hbar A_k}{2\pi e} \tag{1.11}$$

The oscillatory period, $\Delta\left(\frac{1}{B}\right)$, is inversely proportional to the extremal cross-sectional area of the Fermi surface. Conversely, the oscillatory frequency, F, will be proportional to the cross-sectional area of the Fermi surface. Note, only the extremal Fermi surface areas contribute to the overall response due to the destructive interference of all other orbits. Quantum oscillations have proven extraordinarily useful in determining the Fermi surface structure of complex materials.

1.3 Landau levels in topological semimetals

The previous section assumes a parabolic energy dispersion of the charge carriers. In a topological semimetal, however, the electrons have a linear dispersion given by the Hamiltonian $H = \hbar v_F \vec{\sigma} \cdot \vec{k}$, where $\vec{\sigma}$ are the Pauli matrices (see Chapter 2). Solving for the eigenvalues of this Hamiltonian in the presence of a magnetic field gives the energy dispersion relation

$$\varepsilon_n = \pm v_F \sqrt{2\hbar e B n + \hbar^2 k_\parallel^2} \tag{1.12}$$

There are two important things to note in this modified Landau level dispersion. First, the Onsager relation (Eq. 1.11) will remain unchanged. This can be shown by once again comparing the fields at which the ε_n and ε_{n-1} pass through the Fermi level. As a result, Fermi surfaces corresponding to linear bands will also be expected to produce quantum oscillations in material parameters proportional to their extremal areas, given sufficiently low temperatures and scattering rates.

The second feature is that the $n = 0$ Landau level behaves very differently. The energy of this level is $\varepsilon_0 = \pm v_F \hbar k_\parallel$, where $\pm$ comes from the sign of the Hamiltonian and is associated with the chirality of the underlying band crossing. This Landau level does not disperse with magnetic field and will instead remain pinned at the energy of the band crossing. Moreover, it has a fixed band velocity either parallel or antiparallel to the magnetic field. Charge carriers in this Landau level will travel along the magnetic field direction seemingly forever. This is resolved either by large angle scattering events that scatter carriers from one band crossing to another, or by the surface of the crystal. At the surface, the chiral $n = 0$ states are terminated by Fermi arc surface states, which connect Landau levels of opposite chirality. In this manner, an orbit can be formed as carriers move between chiral Landau levels via the Fermi arcs. This orbit is a key transport signature of Fermi arcs and is discussed in detail in Chapter 4.

1.4 The Lifshitz-Kosevich formula

Although the treatment of Sections 1.2 and 1.3 motivates why periodic quantum oscillations should be expected in strong magnetic fields, the form of the oscillations themselves is quite complicated and must take into account experimental considerations such as non-spherical Fermi surfaces, finite temperature, finite scattering times, and the presence of spin. The first derivation of the Lifshitz-Kosevich functional form of quantum oscillations was done in 1954 by I. M. Lifshitz and A. M. Kosevich [12].

dHvA and SdH oscillations can be derived from calculating the thermodynamic grand

potential, Ω. Ω is obtained from summing over all the available energy states of the system

$$\Omega = -k_B T \sum_{\varepsilon} \ln\left(1 + \exp\left(\frac{\mu - \varepsilon}{k_B T}\right)\right) \tag{1.13}$$

$$= -k_B T \int_{-\infty}^{\infty} dk_{\parallel} \left(\frac{eBV}{\hbar 2\pi^2}\right) \sum_{n} \ln\left(1 + \exp\left(\frac{\mu - \varepsilon_n}{k_B T}\right)\right) \tag{1.14}$$

where ε_n are the energy levels of the Landau levels and the Landau level degeneracy has been inserted. At zero temperature and without scattering, this integral can be solved as outlined in [13]. Keeping only the oscillatory component, $\widetilde{\Omega}$, it becomes

$$\widetilde{\Omega} = \frac{e^{5/2} V B^{5/2}}{2^{3/2}\pi^{7/2}\hbar^{1/2} m^*} \left|\frac{\partial^2 A_k}{\partial k_{\parallel}^2}\right|^{-1/2} \sum_{p=1}^{\infty} \frac{1}{p^{5/2}} \cos\left[2\pi p\left(\frac{F}{B} - \frac{1}{2}\right) \pm \frac{\pi}{4}\right] \tag{1.15}$$

where V is the volume of the sample, F is the oscillatory frequency as defined in Eq. 1.11, and the sum is taken over all harmonics, p. Orbits from various slices of the Fermi surface will, in general, have different frequencies and add destructively. This is not the case at the extremal points. At the local maximum (minimum) orbits of higher (lower) frequency are not available to interfere. As a result, F is set by the maximal and minimal cross-sectional areas of the Fermi surface normal to the magnetic field.

The oscillatory component of the magnetization parallel to the field direction is related to the grand potential by $M_{\parallel} = -\frac{\partial \Omega}{\partial B}|_{\mu=\epsilon_F}$. Keeping only the leading order term, this becomes

$$\widetilde{M}_{\parallel} = -\frac{e^{5/2} V B^{1/2} F}{2^{1/2}\pi^{5/2}\hbar^{1/2} m^*} \left|\frac{\partial^2 A_k}{\partial k_{\parallel}^2}\right|^{-1/2} \sum_{p=1}^{\infty} \frac{1}{p^{3/2}} \sin\left[2\pi p\left(\frac{F}{B} - \frac{1}{2}\right) \pm \frac{\pi}{4}\right] \tag{1.16}$$

The magnetization (and associated measurements such as magnetic torque) will show oscillations with a principal frequency set by the extremal area of the Fermi surface. These de Haas-van Alphen (dHvA) oscillations were first observed in elemental bismuth in 1930 and have since become an invaluable tool in exploring the Fermi surfaces of materials [14].

In addition to magnetization, quantum oscillations can be observed in conductivity (or resistivity). This is the Shubnikov-de Haas (SdH) effect. Although not a thermodynamic property itself, the conductivity is related to the density of states at the Fermi energy. The probability of an electron scattering will be proportional to the number of states available for the electron to scatter into. As a result, oscillations in the density of states should also be present in the conductivity

$$\frac{\widetilde{\sigma}}{\sigma_0} \propto \frac{\widetilde{D}(\epsilon_F)}{D_0(\epsilon_F)} \tag{1.17}$$

The exact constant of proportionality between the two will depend on the details of the Fermi surface, the scattering mechanisms, and the number of carrier pockets in the system. A detailed analysis, however, is not necessary if only the oscillatory component of the conductivity, $\widetilde{\sigma}$, is considered.

The density of states is related to the magnetization by

$$\widetilde{D}(\epsilon_F) = \frac{m^{*2}B^2}{e^2\hbar^2F^2}\frac{\partial\widetilde{M}_{\|}}{\partial B} \tag{1.18}$$

Performing this derivative leads to an expression for the oscillatory component of the density of states and therefore the conductivity.

$$\widetilde{D}(\epsilon_F) = -\frac{2^{1/2}e^{1/2}VB^{1/2}m^*}{\pi^{3/2}\hbar^{5/2}}\left|\frac{\partial^2 A_k}{\partial k_{\|}^2}\right|^{-1/2}\sum_{p=1}^{\infty}\frac{1}{p^{1/2}}\cos\left[2\pi p\left(\frac{F}{B}-\frac{1}{2}\right)\pm\frac{\pi}{4}\right] \tag{1.19}$$

Compared to the magnetization, oscillations in the density of states will be phase shifted by 90° where once again F is determined by the extremal cross-sections of the Fermi surface.

So far, the derivation of dHvA and SdH oscillations has been performed at zero temperature, without scattering, and without spin. All three of these factors introduce additional terms into the oscillations which act to reduce the overall amplitude.

The effect of finite temperature

At finite temperature, the probability of finding a particle in a state of energy ϵ is given by the Fermi-Dirac distribution

$$f(\epsilon) = \frac{1}{1+\mathrm{e}^{(\epsilon-\mu)/k_BT}} \tag{1.20}$$

where k_B is the Boltzmann constant, and μ is the chemical potential. The Fermi surface at temperature T can be represented as a distribution of Fermi surfaces at zero temperature whose Fermi energies are distributed around the original Fermi energy, ϵ_F, and each weighted by the derivative of Eq. 1.20 [13]. Due to the spread in Fermi energies, each Fermi surface will have a slightly different frequency leading to a smeared phase given by

$$\phi = \frac{2\pi pm^*}{e\hbar B}(\epsilon_F-\mu) \tag{1.21}$$

Combining this with the aforementioned weighting and integrating over all values of μ gives the reduction factor associated with finite temperature:

$$R_T = \frac{2\pi^2pk_BTm^*/(e\hbar B)}{\sinh(2\pi^2pk_BTm^*/(e\hbar B))} \tag{1.22}$$

All of the temperature dependence of the quantum oscillations is contained in Eq. 1.22. Experimentally, this means that measuring the temperature dependence of dHvA or SdH oscillations provides a means of determining the only material-specific parameter in Eq. 1.22, the effective mass, m^*. Figure 1.2 shows R_T plotted against temperature for three different values of the effective mass.

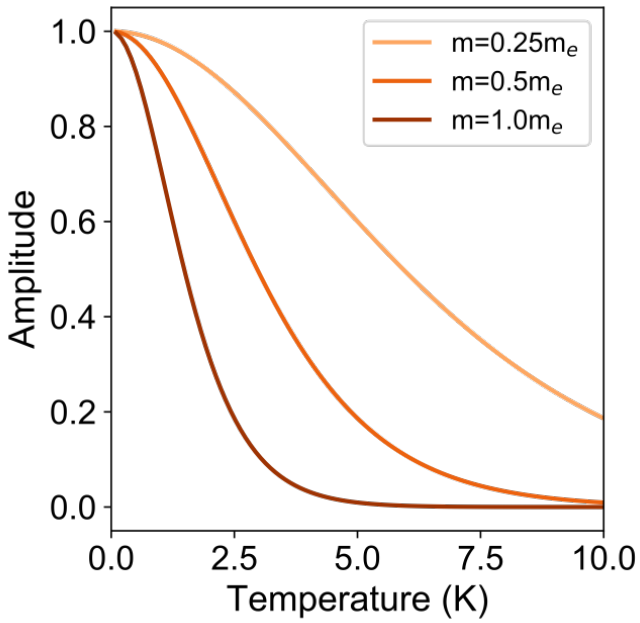

Figure 1.2: **The thermal reduction factor.** The oscillatory amplitude is reduced by increasing temperature as shown for three different values of the effective mass. Fitting the temperature dependence of measured oscillations can be used to experimentally extract the effective mass.

The effect of finite relaxation time

In addition to temperature, a finite relaxation time, typically due to impurity scattering, can reduce the amplitude of quantum oscillations. Relaxation acts to broaden the Landau levels in accordance with the Heisenberg uncertainty principal, $\Delta\varepsilon \propto \hbar/\tau$, where τ is the characteristic relaxation time. This broadening gives the otherwise sharp energy levels a Lorentzian density of states. In a similar manner to the thermal reduction, the broadened Landau levels can be thought of as a series of sharp levels with a spread of frequencies with a Lorentzian distribution. Integrating the phase smearing term (Eq. 1.21) with a Lorentzian gives an expression for the Dingle reduction factor, R_D, associated with the finite scattering time.

$$R_D = \exp(-2\pi^2 p k_B T_D m^*/(e\hbar B)) \tag{1.23}$$

where T_D is the Dingle temperature, named after R. B. Dingle, who first derived it in 1952 [15]. It is defined as

$$T_D = \frac{\hbar}{2\pi k_B \tau} \tag{1.24}$$

where τ is the scattering time. Note, τ here is the scattering time associated with the dephasing of charge carriers undergoing cyclotron motion. It is different from the scattering

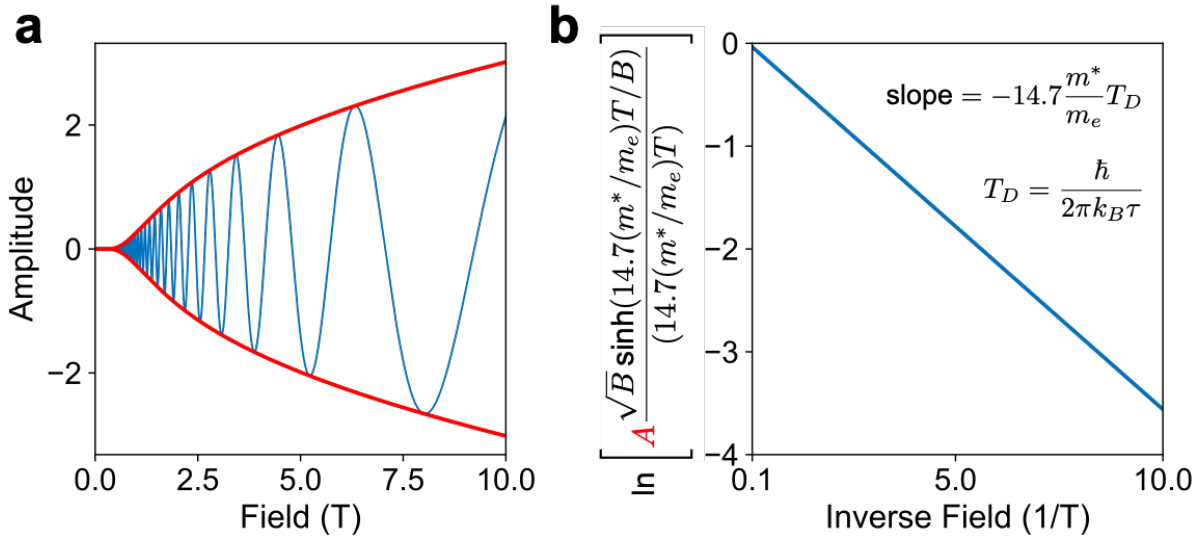

Figure 1.3: **The Dingle reduction factor.** (a) The field dependence of SdH oscillations with a frequency of 15T, effective mass of $0.1m_e$, temperature of 1.8K, and scattering time of 5ps. Both the thermal and Dingle reduction factors have been included, and the envelope of the oscillations has been highlighted in red. (b) When plotted in a Dingle plot, the oscillatory envelope becomes a line and the Dingle temperature can be extracted from its slope, assuming the effective mass has already been determined.

time presented in Section 1.1, which is associated with large-angle scattering events that relax momentum from the electronic system into the lattice. τ here is called the quantum lifetime and is associated with scattering events that change a charge carrier's quantum state. The quantum lifetime, therefore, is always smaller than the transport lifetime.

The Dingle temperature can be extracted from an analysis of the amplitude of the oscillations as a function of magnetic field. For the SdH oscillations shown in Figure 1.3, plotting $\ln\left[A\frac{\sqrt{B}\sinh(14.7(m^*/m_e)T/B)}{(14.7(m^*/m_e)T)}\right]$, where A is the measured oscillatory amplitude, against inverse magnetic field gives a line whose slope is $-[2\pi^2 k_B m_e/(\hbar e)]\frac{m^*}{m_e}T_D$ or $-14.7\frac{m^*}{m_e}T_D$. Assuming the effective mass is known from the temperature dependence, the Dingle temperature, and therefore the quantum lifetime, can be extracted from this plot.

The effect of spin

So far, the role of electron spin has been ignored. Application of a magnetic field will cause the otherwise degenerate spin-up and spin-down Landau levels to split according to the

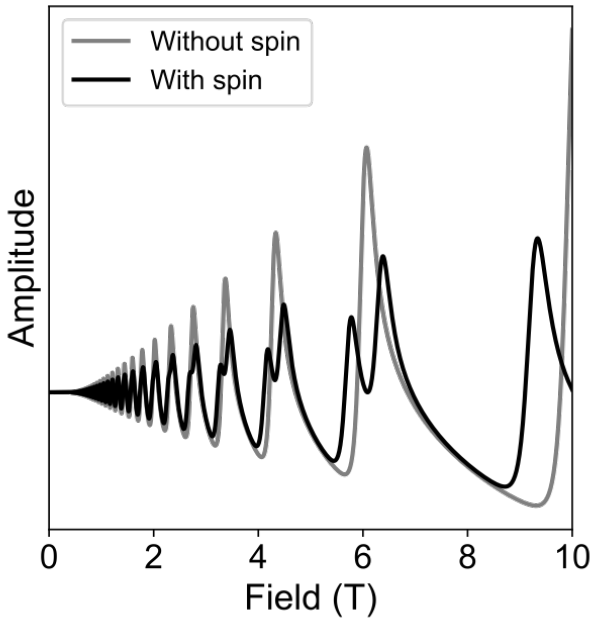

Figure 1.4: **The spin reduction factor.** The presence of electron spin reduces the oscillatory amplitude of each harmonic of the SdH oscillations. When summed over all harmonics, a splitting of the peaks is observed. The summation over all harmonics is also responsible for the asymmetric nature of the oscillations at high field. The frequency, effective mass, temperature and scattering time are the same as in Figure 1.3. The g-factor has been set to 5.

Zeeman energy

$$\Delta\varepsilon = g\mu_B B \tag{1.25}$$

where g is the Landé g-factor and μ_B is the Bohr magneton. This splitting of each Landau level will lead to a phase difference in the oscillations from spin-up and spin-down, reducing the overall oscillatory amplitude. In free space g has a value of 2.0023. In materials, however, it is renormalized by spin-orbit interactions and can take on values far from 2.

With the Zeeman energy splitting, the oscillatory component of the density of states becomes

$$\widetilde{D} \propto \sum_p \frac{1}{p^{1/2}} \left[\cos\left(\Psi + \frac{1}{2}\Delta\varepsilon\frac{\partial\Psi}{\partial\varepsilon}\right) + \cos\left(\Psi - \frac{1}{2}\Delta\varepsilon\frac{\partial\Psi}{\partial\varepsilon}\right)\right] \tag{1.26}$$

where Ψ is defined as $2\pi p(F/B - 1/2) \pm \pi/4$ (from Eq. 1.19). $\partial\Psi/\partial\varepsilon$ can be evaluated using Eqs. 1.5 and 1.11.

$$\frac{\partial\Psi}{\partial\varepsilon} = \frac{p\hbar}{eB}\frac{\partial A}{\partial\varepsilon} = \frac{2\pi p}{eB\hbar}m^* \tag{1.27}$$

Using trigonometric identities and the relationship above to simplify Eq. 1.26 gives an expression for the spin reduction factor, R_S

$$R_S = \cos\left(\frac{\pi}{2} p g m^*/m_e\right) \tag{1.28}$$

When summed over all harmonics, this spin reduction factor will lead to a splitting of the oscillations and associated amplitude reduction. Assuming the effective mass is known, the splitting can be used to experimentally extract the g-factor.

The three reduction factors are summed over all harmonics, p, in the Lifshitz-Kosevich expression for the grand potential (Eq. 1.15). Doing so gives final expressions for the oscillatory components of the magnetization and conductivity.

$$\tilde{M}_{\parallel} = -\frac{e^{5/2} V B^{1/2} F}{2^{1/2}\pi^{5/2}\hbar^{1/2} m^*} \left|\frac{\partial^2 A_k}{\partial k_{\parallel}^2}\right|^{-1/2} \sum_{p=1}^{\infty} \frac{R_T R_D R_S}{p^{3/2}} \sin\left[2\pi p\left(\frac{F}{B} - \frac{1}{2}\right) \pm \frac{\pi}{4}\right] \tag{1.29}$$

$$\tilde{\sigma} = -\frac{2^{1/2} e^{1/2} V B^{1/2} m^*}{\pi^{3/2}\hbar^{5/2}} \left|\frac{\partial^2 A_k}{\partial k_{\parallel}^2}\right|^{-1/2} \sum_{p=1}^{\infty} \frac{R_T R_D R_S}{p^{1/2}} \cos\left[2\pi p\left(\frac{F}{B} - \frac{1}{2}\right) \pm \frac{\pi}{4}\right] \tag{1.30}$$

Measuring either of these parameters in a large magnetic field, therefore, is a powerful tool to determine the shape of the Fermi surface and the masses, scattering times, and anisotropies of the charge carriers.

Chapter 2

Topology in Condensed Matter

2.1 Introduction

Until recently, phases of matter were primarily defined by their symmetries. A crystal consisting of a periodic array of atoms could be characterized by its translational symmetries, rotational symmetries, mirror planes, and so on. Phase transitions occurred when these symmetries were broken. For example, when a ferromagnet is cooled below its Curie temperature, the local magnetic moments align and point in the same direction, spontaneously breaking the previous rotational symmetry. In 1972, however, it was predicted that new types of phase transitions may exist identified not with symmetry breaking, but with changes in the topology of the system. In 2016, David J. Thouless, Duncan M. Haldane, and J. Michael Kosterlitz were awarded the Nobel prize in physics for their work pioneering this field [16, 17, 18, 19, 20].

To understand how phase transitions may occur in the absence of symmetry breaking, consider a conventional band insulator. In this material, the conduction and valence bands are separated by a band gap. This gap prevents electrons from being easily excited into the conduction band, and it therefore does not conduct electrical current. If the atoms in this crystal are gradually moved apart, the electron wavefunctions will become localized as the orbital overlap decreases. This is an adiabatic deformation that does not change any of the original crystal symmetries. As a result, although the electron wavefunctions have changed, the same valence band states that were previously occupied remain occupied, and the same conduction band states that were previously unoccupied remain unoccupied.

Contrast this to a topological insulator where strong spin-orbit coupling leads to a band inversion between the valence and conduction bands. As the atoms are brought together, the valence band will become higher in energy than the conduction band. This band inversion means that the adiabatic deformation leads to a change in the occupied/unoccupied states compared to the localized limit. There is a phase transition, even though no symmetries of the lattice have been changed. Instead, the system has picked up a non-trivial topology. The non-trivial topology of systems such as these leads to interesting new phenomena such

as protected surface states, modified Landau level quantization, and the emergence of new quasiparticle excitations such as Majorana fermions.

Topological phases were first identified in two-dimensional mercury telluride quantum wells [21, 22]. In these systems, tuning the carrier density realizes a quantum spin Hall state in which the bulk is insulating, but quantized conductance can be observed on the device edges. The quantized conductance onsets as the bulk becomes insulating and is due to protected edge states that are a direct consequence of the topology of the bulk bandstructure. The presence of protected boundary states is a hallmark of topological materials and their observation is critical in verifying new topological systems.

2.2 Dirac semimetals

Although topological insulators were the first predicted topological electronic phase, many other topological phases have been discovered since, such as Weyl and Dirac semimetals. Both are three dimensional systems that are closely related to topological insulators, but have only been recently observed. Dirac semimetals can be thought of as topological insulators where crystal symmetries prevent the inverted gap from fully opening, leading to discrete crossing points in the bulk bandstructure.

As previously mentioned, topological insulator states are produced by the inversion of the bulk bandstructure. Consider a system in which the spin-orbit coupling strength can be continuously tuned in the presence of time reversal and inversion symmetries. For weak spin-orbit interactions, the conduction and valence bands will not invert and a conventional insulator state will be present. For strong spin-orbit interactions, however, the bands will invert and hybridization between them will lead to the reformation of a gap, albeit inverted, producing a topological insulator state. Between these two regimes is a critical point where valence and conduction bands touch. At this crossing point, the bands can be approximated as linear and the quasiparticle excitations will be massless Dirac fermions. This is known as a Dirac semimetal.

Although a Dirac semimetal can be achieved by carefully tuning material parameters to reach this critical point, it will be unstable. Any small deviation from the critical point will result in the opening of a gap and the material will become either a topological insulator or a trivial insulator. An alternative route to realizing a Dirac semimetal is to make use of crystal symmetries. In general, the conduction and valence bands will hybridize after inversion to open a gap. In the presence of additional crystal symmetries, however, this gap may be prevented from opening along high-symmetry points in the Brillouin zone. At these crossing points, the dispersion will once again be linear and the quasiparticle excitations about these Dirac cones will be massless Dirac fermions [23].

Figure 2.1 shows this schematically. As a function of a tuning parameter, typically the spin-orbit coupling strength, the gap in a conventional band insulator goes to zero and then becomes inverted. In the presence of sufficient crystal symmetries, however, crossing points between the valence and conduction bands will be protected, leading to a topological Dirac

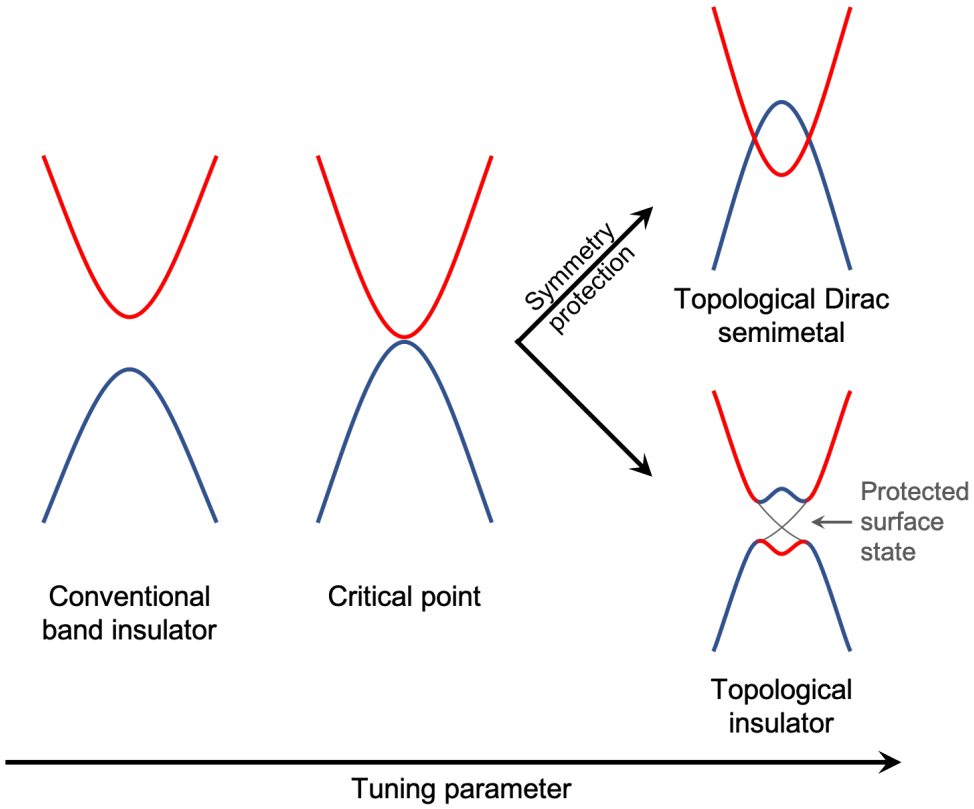

Figure 2.1: **The evolution of topological materials.** As the spin orbit coupling strength is tuned, in the presence of inversion and time reversal symmetries, the band gap in a conventional insulator can be inverted. In a high symmetry lattice, the valence and conduction band crossing points will be protected, forming a pair of Dirac nodes. Breaking inversion symmetry will split each Dirac node into a pair of Weyl nodes. If a crystal symmetry is not present to protect the Dirac nodes, they will hybridize to open a gap and form a topological insulator state.

semimetal. If those symmetries are broken, the bands will hybridize, opening a gap in the bulk. A protected surface state, however, will remain.

The Hamiltonian associated with these doubly degenerate Dirac cones is given by

$$H = \begin{bmatrix} \hbar v_F \vec{\sigma} \cdot \vec{k} & m \\ m & -\hbar v_F \vec{\sigma} \cdot \vec{k} \end{bmatrix} \tag{2.1}$$

where v_F is the Fermi velocity, $\vec{\sigma}$ are the Pauli matrices, $\vec{k}$ is the wavevector measured from the Dirac node, and m is a mass term corresponding to the opening of a gap. The energy of this system is given by $E = \pm\sqrt{(\hbar v_F k)^2 + m^2}$. In the limit of $m = 0$, this is a linear dispersion with a band crossing. This corresponds to the 3D Dirac semimetal state. If

$m > 0$, then a gap is opened and the dispersion is no longer linear. This corresponds to a topological insulator state.

Because the Dirac semimetal is a topological state, there will be protected surface states associated with it. These states are known as Fermi arc surface states and connect the projections of the Dirac nodes on the crystal surface. Since the Dirac nodes are doubly degenerate, each pair of nodes will be connected by two Fermi arcs. Note, in the case where crystal symmetries are relaxed and $m \neq 0$, the Fermi arcs will merge to form the topological insulator surface state [23]. In a Dirac semimetal, however, the bulk is not fully gapped and this allows mixing between surface and bulk states at the Dirac nodes, which can produce novel quantum oscillatory phenomena [24].

As mentioned, $m = 0$ at the critical point between a topological and trivial insulator. However, crystal symmetries may also require that $m = 0$ at specific points. From crystal symmetry arguments, both Na_3Bi and Cd_3As_2 were predicted to be Dirac semimetals protected by C_3 and C_4 crystalline rotation symmetries, respectively [25, 26]. Chapter 4 focuses on Cd_3As_2 and the observation of Fermi arc surface states using microstructured electronic devices.

2.3 Weyl semimetals

So far, time reversal and inversion symmetries have been assumed. Breaking either of these symmetries, however, lifts the degeneracy of the bands, and can lead to a topological phase known as a Weyl semimetal. Without degeneracy, the Hamiltonian in Eq. 2.1 is reduced to:

$$H = \pm \hbar v_F \vec{\sigma} \cdot \vec{k} \tag{2.2}$$

where $\vec{k}$ is again the wavevector measured from the position of the band crossing. There is no longer a mass term, and therefore the dispersion will remain gapless. Moreover, in three dimensions, all three Pauli matrices are incorporated into the Hamiltonian. Since any perturbation can be written in terms of the Pauli matrices and the identity, the only effect will be to shift the Weyl crossing points in k-space, not open a gap. As a result, Weyl nodes are extremely stable. In fact, they can only be annihilated by bringing two nodes of opposite sign together to form the doubly-degenerate Dirac Hamiltonian in Eq. 2.1.

The Weyl nodes described by Eq. 2.2 are topological objects. They act as sources or sinks of Berry curvature, a quantity akin to a magnetic field in momentum space. Integrating the Berry curvature over a surface containing a single Weyl node gives a value of $\pm 2\pi$ corresponding to a Chern number of ± 1. The sign of the Chern number is determined by the sign of the Hamiltonian in Eq. 2.2. As a result, each Weyl node has a chirality associated with it. Since the total chirality (or Chern number) of free space is zero, Weyl nodes must come in opposite-chirality pairs.

Because the Weyl nodes are topological objects, they too must have boundary states associated with them. Like the Dirac semimetal, these are Fermi arc states connecting the projections of opposite-chirality Weyl nodes on the crystal surface. Assuming the simplest

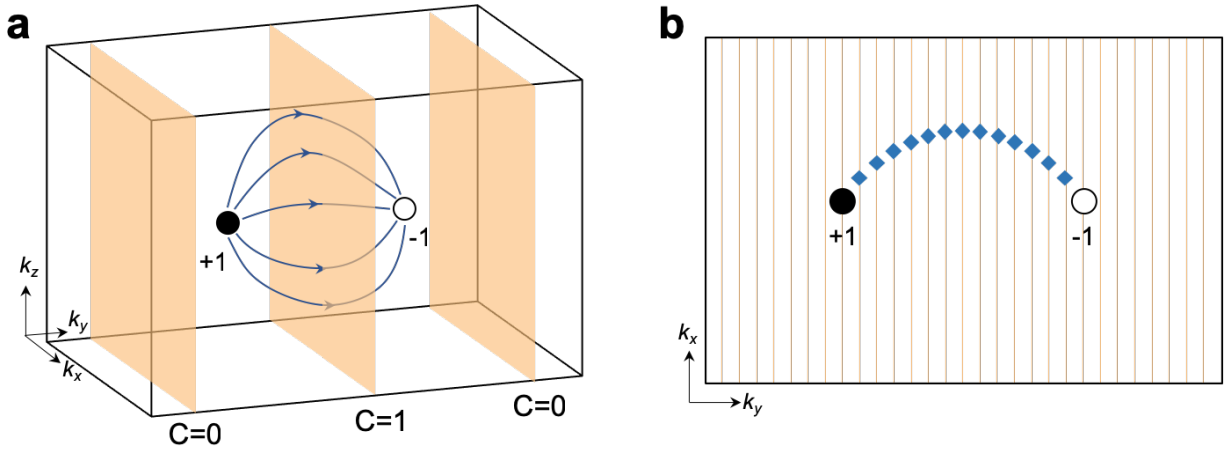

Figure 2.2: **Fermi arc surface states in Weyl semimetals.** (a) Two Weyl nodes of opposite chirality are separated in momentum space. A Berry flux flows from one to the other. A 2D slice of momentum space between the two nodes, therefore, has a net Berry flux flowing through it and an associated Chern number of 1. The same slices outside the two nodes have no Berry flux. (b) The 2D slices between the Weyl nodes are effectively quantum Hall insulator states, and therefore have an edge state associated with them. This edge state, in 3D, becomes a topologically protected Fermi arc which terminates at the projections of the Weyl nodes on the surface of the crystal.

case of two Weyl nodes of opposite chirality at $k_y = \pm k$, there is a Berry flux flowing from one node to the other. Although the bandstructure is not fully gaped, the region between the two Weyl nodes from $k_y = -k$ to $k_y = +k$ is. Thus each k_y slice of the Brillouin zone in this region is a two dimensional insulator with a 2π Berry flux flowing through it corresponding to a Chern number of 1. These slices are equivalent to quantum Hall insulator states and therefore have a single topologically protected edge state associated with them [27, 28]. Because the Berry curvature originates at one Weyl node and terminates at the other, the Chern number and associated edge state must do so as well. Putting all the slices together yields a topologically protected state that connects the projection of one Weyl to the other along the surface of the crystal in an arc. This is illustrated in Figure 2.2.

This explanation of Weyl nodes and Fermi arcs provides an elegant explanation of surface states in Dirac semimetals and topological insulators. A Dirac semimetal can be though of as two superimposed Weyl nodes of opposite chiralities. In general, these Weyl nodes would interact and open a gap, corresponding to a non-zero effective mass in Eq. 2.1. Crystal symmetries, however, can prevent the nodes from interacting, in which case the crossing becomes a doubly degenerate Dirac node. The Fermi arc surface states, associated with the Weyl nodes, however, remain. Therefore, there are two surface states associated with the Dirac node. In the case where crystal symmetries do not prevent the Weyl nodes

from interacting, a gap will be opened and the Fermi arcs will merge to form a topological insulator surface state [23]. The first Weyl semimetals to be discovered were the TaAs-class of transition metal monopnictides: TaAs [29, 30, 31], TaP [32], NbAs [33], NbP [34].

Chapter 3

Focused Ion Beam Fabrication

3.1 Motivation

Micro- and nanostructuring of solids has become an important tool to understand condensed matter phenomena that are only observable at small length scales. Microstructuring has been used to reveal effects such as ballistic electron transport in graphene [35, 36], hydrodynamic flow in $PrCoO_2$ [37], and magnetic focusing in GaAs [38], not to mention packing an ever increasing number of transistors into integrated circuits forming the basis for modern digital electronics [39]. Modern microstructuring techniques give the user precise control over device geometries and length scales. They can be a valuable tool to measure resistivity anisotropies in a crystal, or search for surface or interface phenomena. They also allow one to access regimes otherwise unattainable in the laboratory such as extremely high current densities by reducing a device's cross-sectional area, or tuning the surface-to-bulk ratio by thinning the device to enhance signatures of surface conductance.

There are many methods of device fabrication at the sub-micron level specific to different materials, chemistries, and applications. The focus of this chapter will be on focused ion beam (FIB) fabrication techniques. Although historically FIBs have been primarily used for preparing lamellas for transmission electron microscopy and conducting material analysis, they have become increasingly popular for fabricating devices for transport measurements [40]. Typically, FIBs are part of dual-beam systems incorporating a scanning electron microscope (SEM) such that both milling and non-destructive imaging can be performed. While not able to achieve the few-nanometer length scales of other fabrication techniques, such as electron beam lithography or extreme ultraviolet photolithography, FIB fabrication has several advantages that make it particularly useful for condensed matter applications.

First and foremost, FIB fabrication is extremely versatile. Because it is a ballistic milling technique, it is relatively insensitive to sample chemistry and the same basic recipe can be used to mill a large variety of disparate compounds with only minor modifications to the process. Second, the FIB does not require that samples be grown as thin films. Lamellas can be cut in order to produce devices from as-grown bulk single crystals, allowing it to be

used on compounds that are not easily exfoliated and do not have a well-established thin-film growth recipe. Since bulk crystal growth is often easier and faster than developing a thin-film recipe, FIB fabrication can be used to rapidly make devices and search for new physics in novel materials. Lastly, patterning, milling, and contact deposition can all be done in-situ, reducing the number of machines needed and therefore the fabrication time and equipment requirements. FIB fabrication can produce transport devices from bulk crystals of length scales below 100nm.

Although the FIB can be used to rapidly and efficiently mill devices, it has its limitations. The length scales accessible by the FIB are larger than the lengths achievable from competing techniques such as photo- or electron beam lithography. Moreover, because the FIB relies on ballistic milling, it typically produces a surface layer of damaged, amorphous material. This surface layer can conduct, or even superconduct, in certain instances [5, 41]. As a result, clean interfaces can be difficult to achieve. Nevertheless, the FIB has become an important fabrication tool, allowing devices to be produced quickly from a wide variety of quantum materials.

3.2 The instrument

The basic principal of operation of the FIB is that ions are focused by electric fields into a collimated beam, which is then directed onto a sample to mill patterns or perform imaging. Historically, gallium ions (Ga^{2+}) have been used in this process, although FIBs utilizing other elements such as helium and neon have become commercially available in recent years. The realization of the FIB was made possible by the development of the liquid metal ion source (LMIS), an ion source with sufficient flux to allow collimation into a beam and subsequent milling. The LMIS is produced by heating a metal into a liquid and applying a strong electric field. The electric field shapes the liquid metal into a Taylor cone. Local field enhancement at the sharp tip of the cone leads to ions being ejected from the source via field emission. Although LMIS can be produced from almost any metal and many alloys, gallium is used in the vast majority of sources due to its low melting point, low vapor pressure, and relatively high atomic weight. This allows the ions to be ejected with a small energy spread so they can be easily focused, while remaining heavy enough to mill at significant rates. Once ejected from the LMIS, the gallium ions are passed through a series of apertures and electrostatic lenses, which focus the beam and allow the user to direct it onto the sample for imaging or milling.

In addition to milling, the FIB can be used to deposit material via ion-assisted chemical vapor deposition [42]. A precursor gas of organic molecules containing the metal to be deposited is flowed over the sample. Some portion of the gas adsorbs onto the sample surface. Upon irradiation, the energetic ions of the FIB will break the chemical bonds in the gas molecules, depositing the metal onto the sample surface, while the more volatile organic components are pumped away. Because deposition is driven by the FIB, material can be selectively deposited. This technique can be used to deposit platinum for electrical contacts

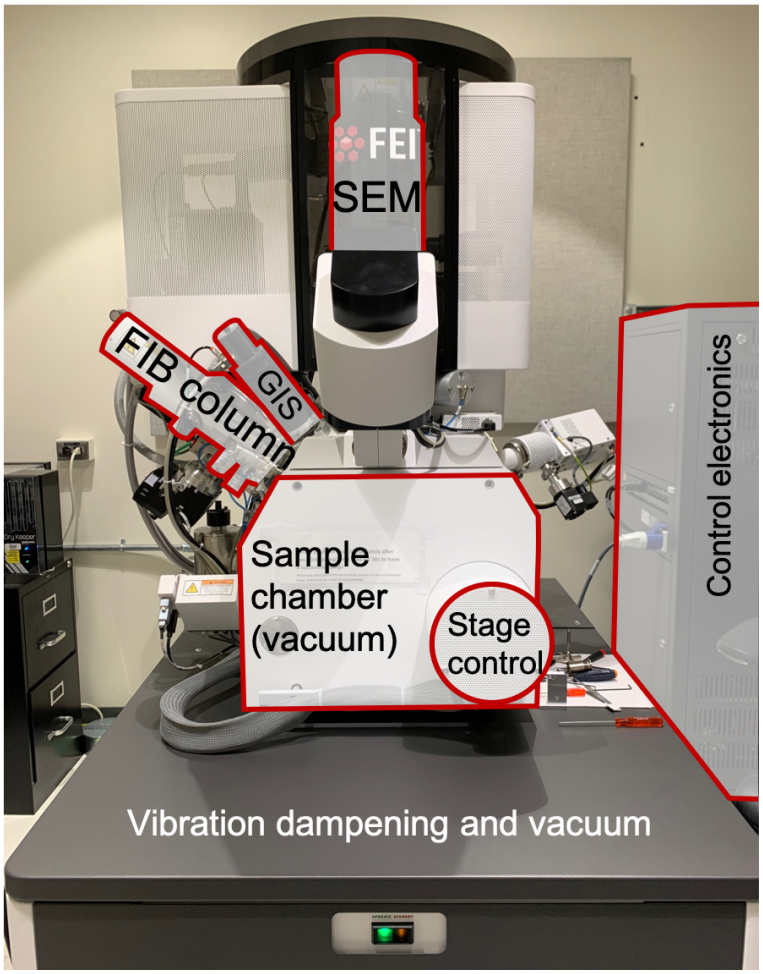

Figure 3.1: **The FIB instrument.** An image of an SEM/FIB dual-beam system manufactured by FEI and used to fabricate transport devices. Important components are labeled. The sample is loaded into the central vacuum chamber. An SEM (top, behind cover) can be used for non-destructive imaging of the sample and elemental analysis. The FIB column (leftmost) can be used to mill material to produce lamellas and define device patterns. The gas injection system (GIS, middle left) can be used in conjunction with the FIB to deposit platinum for contacts or contact repair. An x-ray detector (not shown, behind chamber) can be used in conjunction with the SEM to perform energy dispersive x-ray spectroscopy for elemental analysis. The entire system sits on a vibration dampening stage.

onto fabricated transport devices. Depositing contacts in this manner has the advantage that it can be done in-situ for samples that may be too sensitive for other deposition techniques. The downside, however, is that FIB-deposited metals often have a high organic impurity (carbon) content, resulting in higher resistivities than their elemental counterparts.

Although primarily used for milling and deposition, the FIB can also be used for imaging.

The high energy Ga^{2+} ions impacting the sample scatter electrons from the material. These secondary electrons can then be detected using an Everhart-Thornley detector to build an image as the FIB is raster-scanned over the sample. This is the same principle of operation as SEM imaging, although the FIB will be much more surface sensitive. While the FIB can generate images, it is not typically used for this purpose as the Ga^{2+} ions mill the sample as it is being imaged. Instead, most FIBs are coupled to an SEM which can be used to non-destructively image the sample while the FIB is used for patterning. The full apparatus, including FIB column, SEM column, gas injection system, vacuum chambers, and some control electronics is shown in Figure 3.1.

3.3 Device fabrication

There are two main methods of fabricating FIB transport devices from grown crystals, one being the abbreviated version of the other. For samples being fabricated from macroscopic crystals, a lamella is first cut from the bulk crystal, then mounted onto a substrate, after which the device is patterned using the FIB. For certain samples, the lamella cutting step may be skipped and the as-grown crystal can be directly mounted onto a substrate and patterned. Which method is more appropriate for a specific application depends on the thickness of the bulk crystal and its crystallographic orientation.

Preparing a lamella is the more versatile option and allows a device to be made from an arbitrarily-shaped crystal of almost any dimension. The basic technique is very similar to transmission electron microscopy lamella preparation, but done at a much larger scale. It is summarized in Figure 3.2. A rectangular cross-section (lamella) is cut from the crystal using the FIB. Typical dimensions are 20 µm × 10 µm × 3 µm, although these length scales can be varied to meet application-specific needs. Undercutting the rectangle allows it to be easily lifted out from the crystal. A small (<1 µm) bridge is left connecting the lamella to the bulk of the crystal. This holds the lamella in-place until ready for lift-out, during which it is easily broken. For electron microscopy lamellas, lift-out is typically done with a micro-manipulator in-situ. At the larger length scales used for transport devices, it can be done by hand using an optical microscope and great care.

Once removed from the bulk crystal, the lamella is mounted onto a substrate using non-conducive two-part epoxy. Typically glass (SiO_2) substrates are used. Fast-drying, low-outgassing epoxies are desired. The lamella "floats" on the epoxy, leaving one surface exposed, while the rest of it is embedded. Once fully cured, there are two options for creating electrical contacts. Most often, gold is deposited over the entire lamella/epoxy area. Because the top surface of the lamella is not covered by epoxy, the gold makes electrical contact to the sample and the negative space is cut out with the FIB to create contacts. An alternative is to use the aforementioned platinum deposition capabilities of the FIB to direct-write electrical contacts onto the sample. This is typically used for samples that are too surface sensitive for gold evaporation or to repair problems (such as cracks) in the gold deposition. FIB-deposited platinum typically has a much lower conductivity than deposited gold, so gold is preferred

where possible. If the bulk crystal is thin (under 10 µm) cutting a lamella is not necessary and the crystal can be directly mounted into the epoxy and deposited with gold.

The next step is to return the sample to the FIB and mill the desired device geometry. If a layer of gold has been deposited, the gold is first milled from the active area of the device to prevent it from short-circuiting contacts. If platinum contacts are being deposited, they should be deposited first so that the overspray can be milled away as part of the device patterning. At this point the device pattern can be milled. Several parameters need to be fine tuned in order to achieve the desired feature fidelity. The FIB beam current affects the sputter rate and the spot size. Increasing the current can speed up the patterning process, at the expense of feature resolution. Typically, different beam currents are used for coarse and fine features. The acceleration voltage affects the stopping range of the Ga^{2+} ions in the material, and therefore the surface damage induced by the beam. Finally, the milling rate and therefore the patterning time is highly material dependent. Once the device has been milled, the gold or platinum contacts are connected to wires using wire-bonding or silver epoxy and the device is ready to measure.

The primary consideration when fabricating devices using the FIB is the surface damage induced by the Ga^{2+} ions. At an acceleration voltage of 30kV (60keV kinetic energy), where most FIBs operate, Ga^2+ has a penetration depth of approximately 20nm, as shown in Figure 3.3. This indicates that FIB devices will be surrounded by an approximately 20nm thick layer of damaged material. This damage can take two different forms: amorphization due to implanted defects, and a change in the chemical composition due to differential sputtering yields. The first is a direct result of impacting a crystalline lattice with high energy ions. The Ga^{2+} will knock atoms out of position, creating dislocation defects and vacancies. In addition, some of the Ga^{2+} will become implanted in the crystal. This may dope the material or otherwise modify the surface potential. Moreover, different chemical elements in the crystal may be sputtered at different rates, causing the surface layer to have a different stoichiometry than the bulk. How this surface layer affects transport behavior is highly material dependent. In some cases, the damaged layer was found to have almost no effect, with bulk quantum oscillations and intrinsic surface states remaining directly observable [3]. In other cases, however, the damaged layer was found to superconduct at low temperature, short-circuiting the bulk crystal and dominating the transport behavior [5, 41]. This is further discussed in Section 5.3.

The damage produced by the FIB can be modeling using the "Stopping and Range of Ions in Matter (SRIM)" software package [43, 44]. Figure 3.3 shows the scattering cascade cause by 60keV Ga^{2+} ions impacting the surface of a TaAs crystal. As can be seen, each Ga^{2+} ion causes multiple scattering events. The depth of the damage layer is approximately 20nm and the As has been sputtered five times faster than the Ta due to its lower atomic weight and increased volatility. As mentioned, the exact sputtering yields will be highly material dependent and have to be compensated for with larger beam currents or longer milling times.

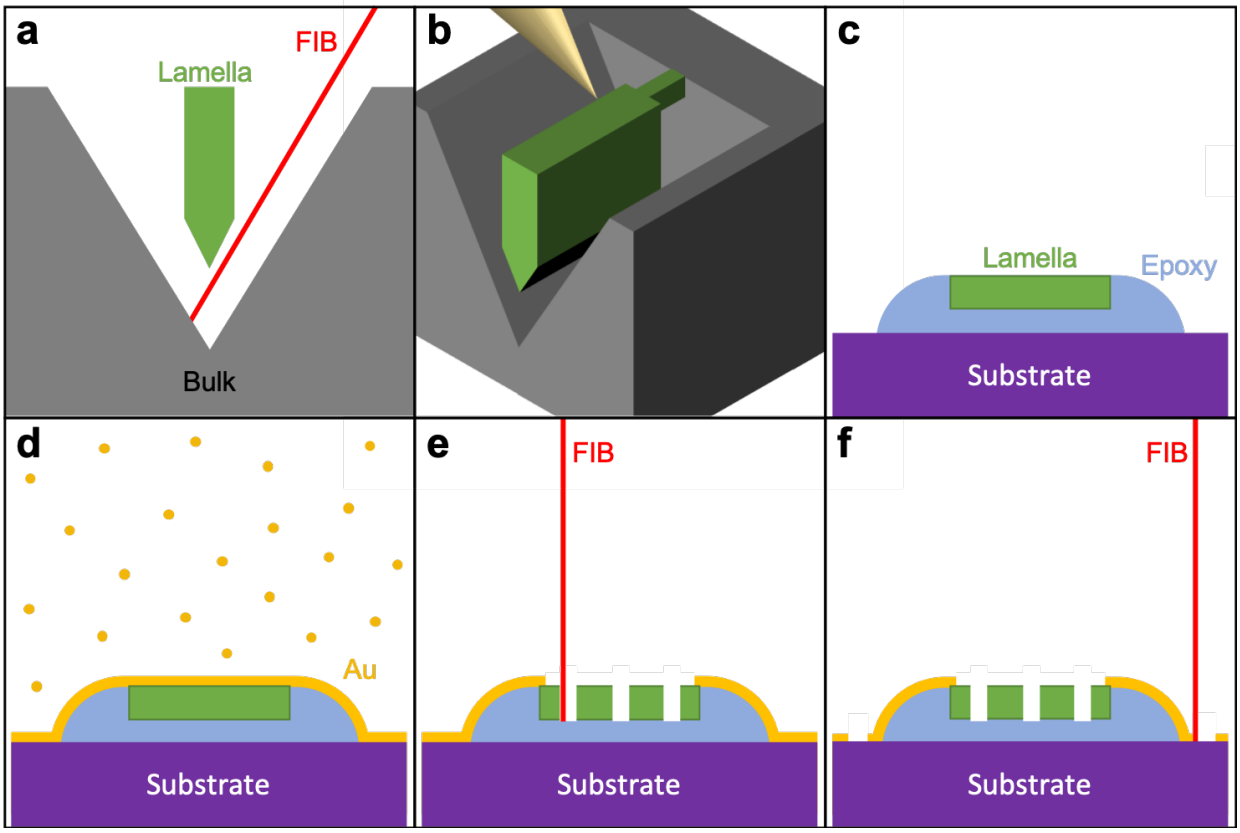

Figure 3.2: **FIB fabrication.** (a) The FIB is used to cut and undercut an approximately rectangular lamella (green) from a bulk crystal. (b) A micromanipulator or other probe (yellow) is used to remove the lamella from the crystal, breaking the connecting bridge in the process. (c) The lamella is then transferred to a drop of epoxy (blue) on a substrate (purple). The lamella is embedded in the epoxy such that the top surface remains exposed. (d) Gold (yellow) is deposited over the entire sample. This step is not necessary if in-situ platinum deposition is used to make electrical contacts instead. (e) The lamella is milled into the desired device geometry using the FIB. (f) The gold is milled into individually addressable pads that can be contacted using either silver epoxy or wire bonding. This step is not necessary if using platinum deposition. Note: For sufficiently thin crystals, milling of a lamella is not necessary and the crystal itself can be directly mounted as shown in step (c).

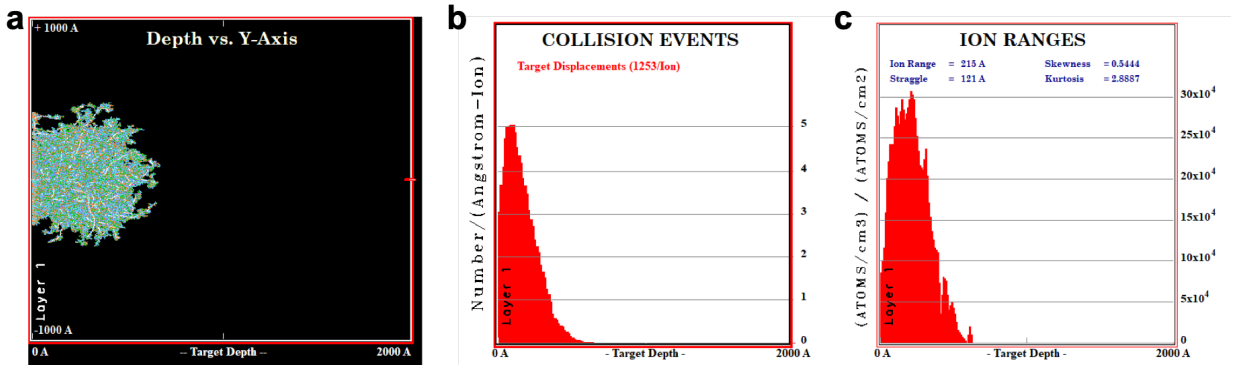

Figure 3.3: **Ion damage.** (a) The simulated damage cascades caused by 60keV Ga^{2+} ions impacting the surface of a TaAs crystal at normal incidence. (b) The displacement of atoms in the TaAs lattice due to collisions with the Ga^{2+} ions. (c) The final depth of the Ga^{2+} ions that remain embedded in the material. Both (b) and (c) peak at around 20nm, quantifying the depth of the surface damage layer. These calculations were performed for TaAs using the SRIM software package [43, 44].

Chapter 4

Fermi Arc States in Cadmium Arsenide

4.1 Motivation and previous results

Although topological semimetals have been extensively predicted, transport signatures of their topological properties have remained rare. Specifically, up until this work, Fermi arc surface states had only been observed by local probes such as scanning tunneling microscopy (STM) and angle resolved photoemission spectroscopy (ARPES). Direct transport observation and manipulation of Fermi arcs is necessary not just to understand the behavior of these unique states, but to use them in device applications. The most straightforward way to directly observe a Fermi arc is through a unique coherent cyclotron orbit known as a Weyl orbit. These orbits combine surface and bulk states to produce measurable signatures of charge carriers traversing the Fermi arcs. Because this orbit depends strongly on sample thickness, FIB fabrication is a natural solution to achieve the sub-micron device geometries required.

Cd_3As_2 has long been known to have high electron mobilities and long mean free paths, making it appealing even for non-topological device applications [45]. More recently, however, refinements to the crystal structure combined with ab initio calculations predicted it to be a Dirac semimetal [26, 46]. The ordering of cadmium vacancies in the low temperature phase of Cd_3As_2 leads to a large unit cell of 176 atoms in the tetragonal $I4_1/acd$ (No. 142) space group. Density function theory (DFT) calculations show two doubly degenerate Dirac nodes located symmetrically about the Γ-point at $(k_x, k_y, k_z) = (0, 0, \pm 0.032)\text{Å}^{-1}$ [26]. The band structure about these nodes is illustrated in Figure 4.1b. Close to the nodes the dispersion is linear and has been confirmed by ARPES and STM measurements [47, 48, 49, 50, 51]. As described in Section 2.2, the C_4 rotational symmetry of the crystal prevents the nodes from interacting and opening a gap [26].

The projections of the Dirac nodes onto the crystal surface will be connected by two Fermi arc surface states. Although surface states in general are quite difficult to detect, in

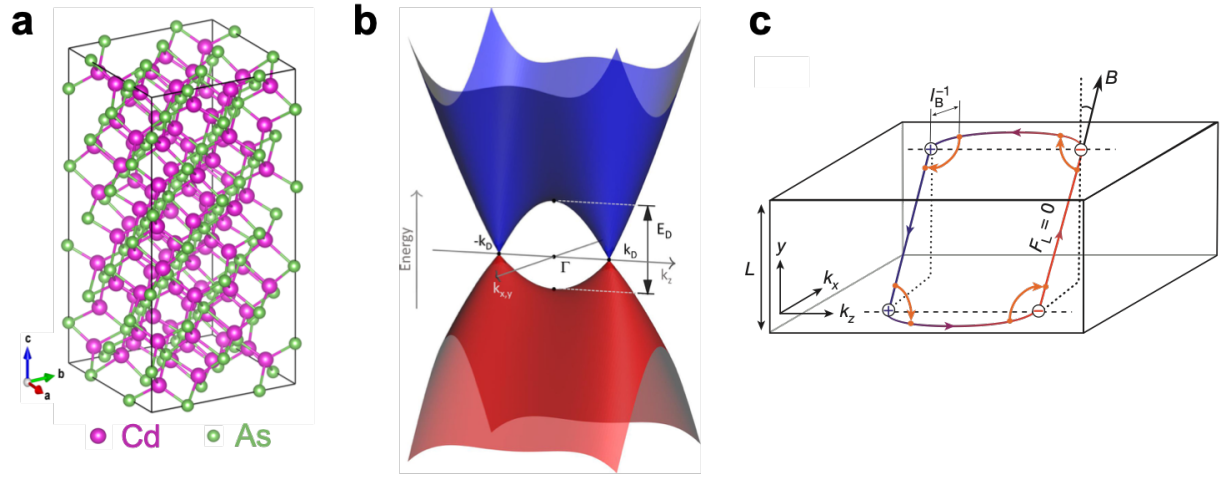

Figure 4.1: **Cd_3As_2 crystal and electronic structure.** (a) The crystal structure of Cd_3As_2 is tetragonal and centrosymmetric with the space group $I4_1/acd$ (No. 142). (b) A schematic highlighting the two Dirac crossings about the Γ point and the associated Dirac cones. Adapted from Ref. [52]. (c) The Weyl orbit connects Fermi arc states on opposite crystal surfaces through the bulk Dirac nodes, forming a coherent, closed quantum orbit. Adapted from Ref. [3].

sufficiently thin materials and strong magnetic fields it has been proposed that Fermi arcs can participate in a coherent cyclotron orbit giving rise to quantum oscillations [24]. The application of a magnetic field normal to the surface drives charges along the Fermi arc by the Lorentz force. When those charges reach the end of the Fermi arc, the only available states are the Landau levels from the bulk Dirac Fermi surface. In a large magnetic field, a significant fraction of charges will enter the zeroth Landau level. As a result of its chiral nature, charge carriers in this level have a constant band velocity parallel to the field and will move along it to the opposite surface. There, they enter the opposite Fermi arc and the process repeats. This process, summarized in Figure 4.1c, forms a closed, coherent orbit and therefore leads to quantum oscillations in high mobility samples. These oscillations are analogous to the oscillations described by the Lifshitz-Kosevich formula in Chapter 1 and will result in periodic SdH oscillations in the device resistance as a function of inverse magnetic field.

The oscillatory frequency corresponding to this Weyl orbit can be derived by considering the time that a particle spends in each leg of the orbit. The time spent in the Fermi arc is given by $\tau_{arc} = \hbar k_0/ev_F B$, where k_0 is the arc length of the arc and v_F is the Fermi velocity. The time spent traversing the bulk is $\tau_{bulk} = L/v_F$. Since both must be done twice to complete the orbit, the total time is given by

$$\tau = 2\frac{\hbar k_0 + eLB}{ev_F B} \tag{4.1}$$

The energy levels of the Weyl orbit can be related to the orbital time by the correspondence principle, stating that $\varepsilon_n \tau = 2\pi\hbar(n+\gamma)$. This gives energy levels of

$$\varepsilon_n = \frac{\pi v_F \hbar (n+\gamma)}{L + \hbar k_0 / eB} \tag{4.2}$$

These energy levels will cross the chemical potential, μ, at periodic intervals of the inverse magnetic field. Solving for the spacing between subsequent crossings of energy levels n and $n+1$ and inverting gives the expression for the frequency expected from these oscillations

$$F_S = \frac{k_0 \mu}{e \pi v_F} \tag{4.3}$$

where the chemical potential, μ, is measured from the Dirac point. A detailed derivation is available in Ref. [24].

Eq. 4.3 states that particles undergoing the Weyl orbit will exhibit quantum oscillations periodic in inverse magnetic field, similarly to conventional de Haas van Alphen or Shubnikov de Haas oscillations. There are several key properties that make these oscillations unique, however. First, charge carriers traversing the bulk will be in the chiral, zeroth Landau level with a band velocity that is parallel to the applied magnetic field. As a result, these charge carriers will undergo Lorentz force-free motion and therefore this leg of the orbit will not affect the oscillatory frequency. Instead, the width of the sample only manifests as an overall phase. Second, a non-adiabatic correction to the orbit will give deviations from perfect periodicity at large enough magnetic fields. These two properties provide concrete, testable predictions that differentiate Weyl orbit oscillations from conventional SdH oscillations.

4.2 Flux growth

Single crystals of Cd_3As_2 were grown using the flux growth technique. In this technique, precursors are dissolved in a liquid flux from which the target compound precipitates. First, the precursors and flux are heated to a temperature sufficient for the flux to melt and the precursors to dissolve, forming a homogeneous solution. As the temperature is lowered, the solubility of the reactants in the flux decreases and the solution becomes saturated. This leads to precipitation of crystals of the target compound out of solution. The ampule containing the reaction can be centrifuged at high temperature to separate the liquid flux from the precipitated crystals. Chemical etching can be used to remove any excess flux from the crystals.

The solubility of the precursors and the stoichiometry of the precipitant will depend strongly on the ratio of the flux to the precursors. Binary or ternary phase diagrams are typically consulted to ensure that only the target compound is produced without impurity phases.

In the case of Cd_3As_2, cadmium was used as the flux, making this a self-flux growth. A 5:1 ratio of Cd to Cd_3As_2 (4:1 Cd to As) was placed into an aluminum oxide crucible

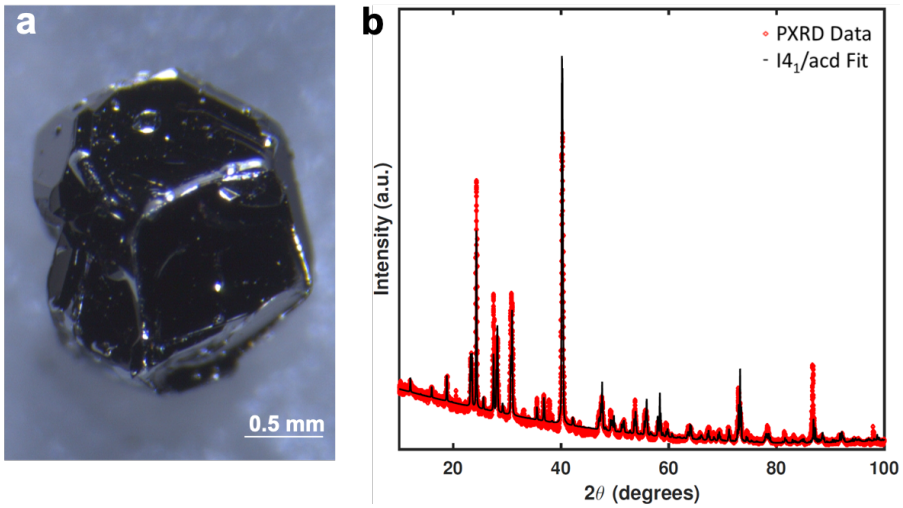

Figure 4.2: **Cd_3As_2 flux growth.** (a) An image of a crystal of Cd_3As_2 grown using the flux technique. A 1:5 melt of Cd_3As_2:Cd was heated to 825°C and slowly cooled to 425°C where it was centrifuged. Crystals in excess of 2mm were obtained. (b) Powder x-ray diffraction measurements on the resulting crystals show a good fit to the $I4_1/acd$ (No. 142) space group. Adapted from Ref. [3].

and sealed into an evacuated quartz ampule. The ampule was heated to 825°C and held for 48 hours to ensure a homogeneous solution. It was then cooled at 6°C/hour to 425°C, precipitating Cd_3As_2 crystals out of solution, while remaining above the melting point of Cd. The hot ampule was removed from the furnace and centrifuged to separate the crystals from the Cd flux. Crystals of varying sizes exceeding 2mm were obtained and confirmed to be in the $I4_1/acd$ (No. 142) space group by both powder and single crystal x-ray diffraction. Figure 4.2 shows a crystal grown using this method and the corresponding powder x-ray diffraction analysis.

4.3 Fermi arcs in microstructured devices

Microstructured devices to search for Fermi arc surface states were fabricated using the FIB fabrication method outlined in Chapter 3. Since the Dirac nodes in Cd_3As_2 are separated in the [001] direction, their projections will be non-degenerate on all surfaces except [001], with their separation maximized on the [100] and [010] surfaces. Therefore the ideal device geometry would be one with large, polished faces normal to the [100] or [010] directions and current flowing along the orthogonal axis. One such Hall bar device is shown in Figure 4.3. This device was fabricated by cutting a lamella from the [010] face of a bulk Cd_3As_2 crystal.

Applying a magnetic field perpendicular to the current direction and out of the device plane (crystallographic [100] direction, denoted 90°) shows a single set of Shubnikov de Haas

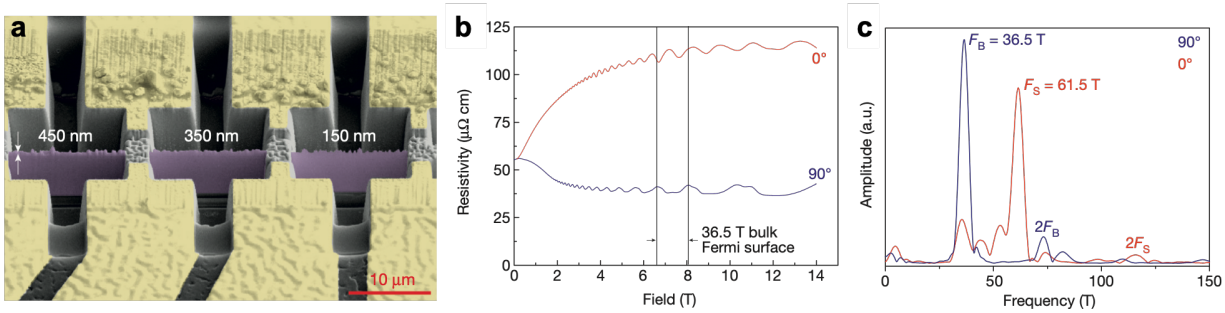

Figure 4.3: **Surface oscillations.** (a) An SEM image of FIB fabricated Hall bars of varying thicknesses. Contacts are colored gold and the active Cd_3As_2 crystal is purple. (b) SdH oscillations can be observed in the resistivity upon application of a magnetic field. (c) A Fourier transform reveals two oscillatory frequencies. A 36.5T frequency is observable at all field angles, while a 61.5T frequency is only apparent when the field is normal to the Cd_3As_2 surface. Adapted from Ref. [3].

(SdH) oscillations in the magnetoresistance. A Fourier transform shows a single oscillatory frequency in inverse magnetic field of 36.5T. These oscillations have been previously observed in Cd_3As_2 crystals and agree with those expected from the bulk Fermi surface [26, 53]. The oscillations onset around 1T at 2K, a result of the low charge carrier effective mass and long scattering times that this material is known for [45].

Tilting the field into the plane of the device, (parallel to the crystallographic [010] direction, denoted 0°), however, reveals a second set of oscillations. A Fourier transform in inverse field shows two frequencies. A new frequency at 61.5T, and the 36.5T bulk frequency previously observed. The presence of both frequencies indicates that one is not an evolution of the other, but comes from an independent orbit. Namely, the 61.5T frequency does not stem from an anisotropy of the bulk Fermi surface.

Fitting the Lifshitz-Kosevich thermal reduction factor to the temperature dependence yields an effective mass of $0.044m_e$ for the 36.5T oscillations. The 61.5T oscillation is found to have a mass $0.050m_e$. Both are shown in Figure 4.4a. Until this study an oscillation with this mass and frequency had not been previously observed in Cd_3As_2 [3].

An angle dependence provides additional evidence for the unique origin of the second frequency. As the magnetic field angle is tilted towards the [100] direction, the 36.5T frequency does not disperse significantly. This is consistent with the spherical nature of the bulk Fermi surfaces. The 61.5T frequency, on the other hand, increases rapidly and is not observable above approximately 50°. Its dispersion is well fit by a $1/\cos\theta$ dependence, the hallmark of a two-dimensional Fermi surface. A polar plot (Figure 4.4b) shows the surface nature of the 61.5T frequency. Although this dependence would be expected for the Weyl orbit, it would also be expected for trivial in-gap surface states. Additional measurements are required to show that they are an example of a Weyl orbit and stem from the topological nature of Cd_3As_2 and the Fermi arc states.

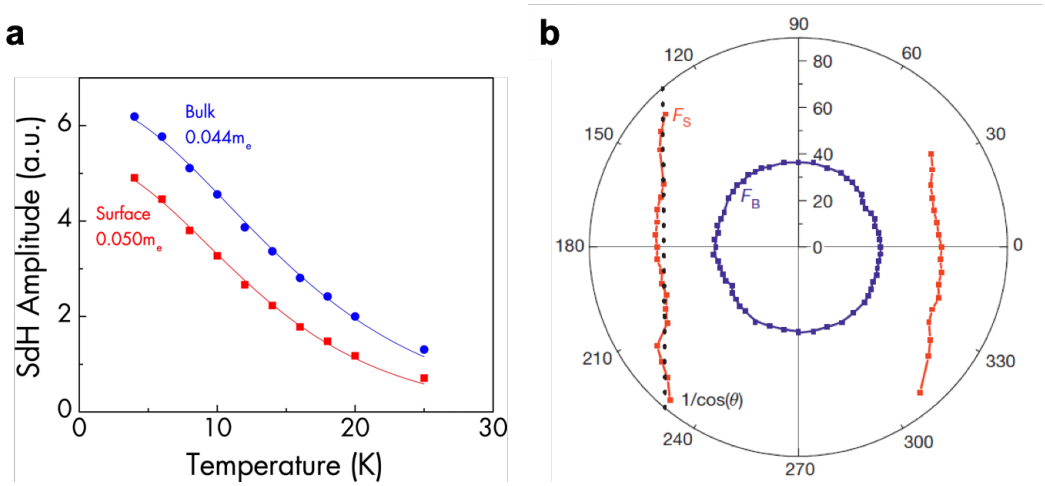

Figure 4.4: **Effective mass and angle dependence.** (a) The temperature dependence of the SdH oscillations at 0°, normal to the device surface. The two frequencies are fit to the Lifshitz-Kosevich thermal damping dependence to extract their effective masses (see Section 1.4). The 36.5T frequency, labelled "Bulk", has a mass of $0.044\mathrm{m}_e$, in close agreement with previously reported results. The 61.5T frequency, labelled "Surface" has a mass of $0.050\mathrm{m}_e$. (b) A polar plot shows the dispersion of the two SdH frequencies. The 36.5T frequency does not disperse strongly with angle and is well explained by the approximately spherical bulk Fermi surface of Cd_3As_2. The 61.5T frequency, however, disperses with the $1/\cos\theta$ dependence characteristic of a surface origin. Adapted from Ref. [3].

One such measurement is a thickness dependence. Because a Weyl orbit mixes surface and bulk trajectories, it can be disrupted by bulk scattering. In fact, if the bulk mean free path is smaller than the device thickness, one would expect scattering to lead to phase decoherence and oscillations would not be observed. Since the Weyl orbits traverse the bulk twice, this requirement is even more stringent and the device thickness must be less than half the bulk mean free path.

The thickness of the devices can be accurately measured via the Knudsen effect, a finite-size effect arising from ballistic transport in ultraclean materials. At low fields, a peak in the magnetoresistance is observed, the result of ballistic charge carriers scattering at the surfaces of the device. As the magnetic field is increased, however, the cyclotron orbit becomes smaller than the device thickness, reducing interactions between conduction electrons and the device surfaces. The total surface scattering is maximized when the diameter of the cyclotron orbit is on the order of the device thickness. This corresponds to a resistance maximum at a field of $B_{\max} = 2\frac{\hbar k_F}{eL}$, where L is the sample thickness [54, 55, 56]. The Knudsen effect is important for two reasons. First, it establishes that the device thicknesses are on the order of the bulk mean free path, a prerequisite for observing the Weyl orbit. Second, it can be used to confirm the measured device thickness.

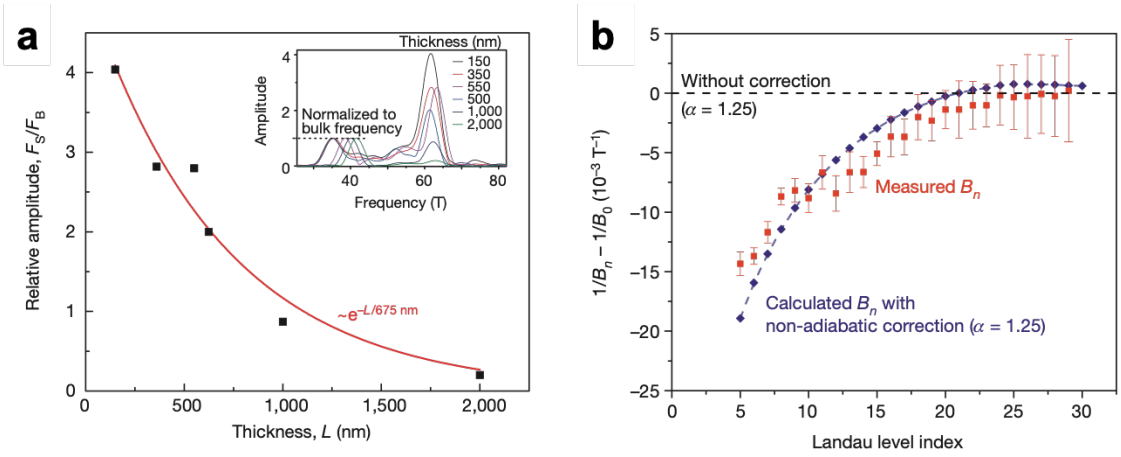

Figure 4.5: **Thickness dependence and non-adiabatic correction.** (a) The thickness dependence shows an exponential suppression of the surface oscillations with a characteristic sample width of 675nm, close to half the transport mean free path (500nm). Note, the surface amplitude has been normalized by the bulk amplitude to account for sample variation. (b) The position of the nth oscillation (red) deviates from perfect periodicity (black dashed). This deviation is well described by a non-adiabatic correction that would only be expected from a Weyl orbit (purple) [24]. Adapted from Ref. [3].

The thickness dependence of the surface oscillation amplitude is shown in Figure 4.5a. As expected, the oscillatory amplitude monotonically decreases with increasing device thickness up to 2µm, above which surface oscillations are no longer observable. Moreover, the amplitude can be well-fit by a decaying exponential with a characteristic length of 675nm. Note, the surface oscillation amplitude has been normalized by the amplitude of the bulk oscillations to account for variations in overall carrier mobility and impurity concentration between samples. This length scale is half the bulk scattering length associated with the surface oscillations (since the Weyl orbit traverses the bulk twice) and should be compared to the bulk mean free path of 1.0µm. This value has been estimated from transport measurements as $l = v_F\tau = v_F m^*/(ne^2\rho_0) = 1.0\mu m$, where $\rho_0 = 55\mu\Omega\,cm$ is the zero field resistivity at base temperature, $n = 2k_F^2/(3\pi^2) = 2.5 \times 10^{18} cm^{-3}$ is the carrier density for a spherical Fermi surface, τ is the scattering time, m^* is the carrier effective mass, and $k_F = m^* v_F/\hbar = 3.3 \times 10^8 m^-1$ is the Fermi wavenumber obtained from the bulk SdH oscillations. The agreement between the bulk mean free path (1.0µm) and the bulk scattering length derived from the thickness dependence of the surface oscillations (1.35µm) provides evidence that the carriers are indeed traversing the bulk, as would be expected from the Weyl orbit associated with topological Fermi arcs.

Typically quantum oscillations are associated with the quantum scattering length of the quasiparticles. Any scattering will lead to a loss of coherence and therefore a loss of quantum oscillations. This differs from the transport lifetime, which is associated with momentum

relaxation and large-angle scattering events. Interestingly, the Weyl orbit in Cd_3As_2 appears to be limited by the transport, not the quantum, lifetime. Although this is unusual for quantum oscillations, it may be understood as a consequence of the chiral zeroth Landau level. This state is expected to exhibit an additional resilience to small-angle scattering due to its chiral nature. The only available states for quasiparticles to scatter into are in the zeroth Landau level of the opposite-chirality node. As a result, all scattering should come from the same large-angle scattering that determines the transport lifetime. Since quasiparticles in the Weyl orbit use the zeroth Landau level to traverse the bulk, it would be expected that the decoherence length in this orbit would be the same as the transport mean free path.

A second confirmation that the orbit being observed is indeed the Weyl orbit expected from Fermi arcs comes from the phase of the oscillations at high fields. Specifically, the phase is found to have a field dependence, which would not be expected from conventional quantum oscillations. As shown in Figure 4.5b, the peak position B_n of the n^{th} oscillation deviates from perfect periodicity. The peaks move to higher fields, corresponding to a decrease in the effective frequency. This decrease can be explained by a non-adiabatic correction to the orbit caused by tunneling at the junctions between surface and bulk legs. In presence of a strong magnetic field, charge carriers can tunnel from one state to the other. This process, known as magnetic breakdown, has been observed extensively in bulk materials [13]. In the case of Cd_3As_2, it leads to quasiparticles skipping some of the Weyl orbit, reducing the effective length of the orbit. With this correction, the oscillatory frequency to first order is given by

$$F_S(B) = F_S(0)\left[1 - \frac{4\alpha}{k_0}\sqrt{\frac{eB}{\hbar}}\right] \tag{4.4}$$

where $F_S(0)$ is the frequency from the full Weyl orbit given in Eq. 4.3 and α is a material parameter associated with the tunneling barrier between the bulk and surface [24]. Figure 4.5b shows calculated peak positions for $\alpha = 1.25$, which appear to track the deviation of the measured peak positions from periodicity well. Although magnetic breakdown can be observed in bulk quantum oscillations, it typically occurs between two Fermi surfaces and manifests itself as an additional set of high frequency oscillations. Here, the same mechanism reduces the orbit length and gives a smooth evolution of a single oscillatory frequency.

Lastly, a third confirmation that the oscillations observed are a result of Fermi arcs is the geometry dependence. Specifically, the Weyl orbit is expected to have oscillations at inverse magnetic field values of

$$\frac{1}{B_n} = \frac{e}{k_0}\left(\frac{n\pi v_F}{E_F} - L\right) \tag{4.5}$$

where L is the sample thickness [24]. The sample thickness contributes an overall phase to the oscillations. For a sample with a constant thickness, such as for the rectangular cross-section devices discussed so far, the phase of the oscillations at every sample location is the same and they add constructively. For a non-uniform cross-section, however, one would expect the phase to vary spatially with the device thickness and the oscillations to interfere

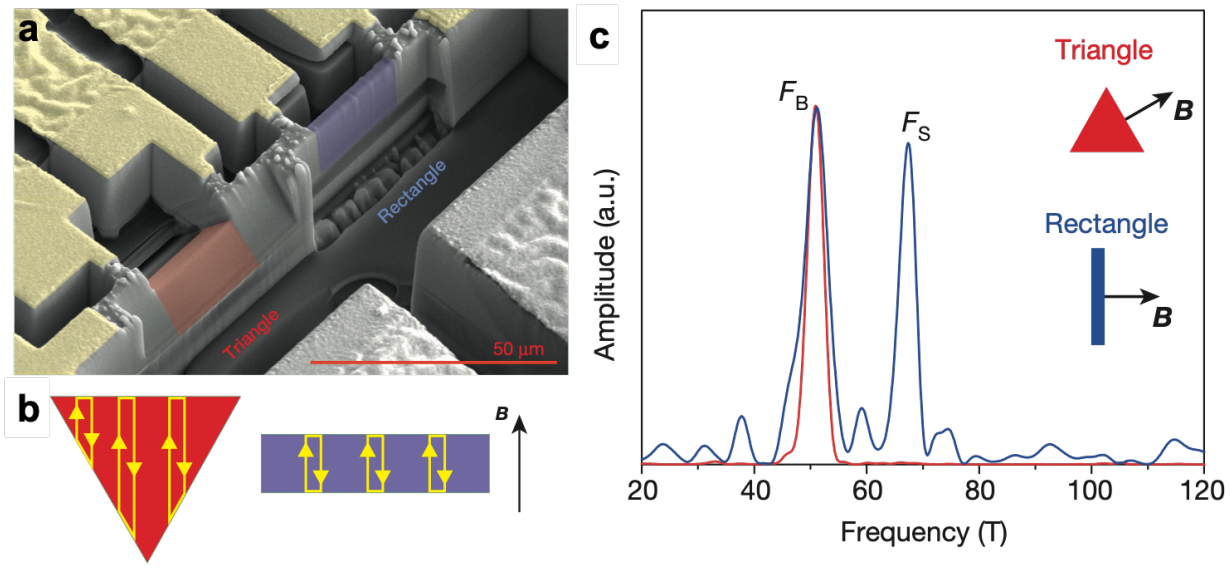

Figure 4.6: **Triangular device.** (a) An SEM image showing two Cd_3As_2 transport devices: a triangular device in red and a rectangular device in blue. (b) The cross-sections of the two devices. When a magnetic field is applied, Weyl orbits in the triangular device will have different lengths in the bulk whereas orbits in the rectangular device will all have the same length. (c) The varying device width of the triangular device (red) leads to destructive interference of the Weyl orbit oscillations. A Fourier transform shows only the bulk frequency. The rectangular device (blue), on the other hand, shows both surface and bulk frequencies. Adapted from Ref. [3].

destructively. As a result, the surface state oscillations would be expected to vanish, leaving only the bulk oscillations. In order to test this, a device with a triangular cross-section was fabricated. When magnetoresistance measurements were performed, the device showed only oscillations at the bulk frequency. The surface frequency was not present, although it was present in a rectangular control device fabricated in series from the same crystal (see Figure 4.6). Such a dependence of the oscillations on device geometry would not be expected for conventional quantum oscillations and is a confirmation that the source of the oscillations is indeed a Weyl orbit involving Fermi arc surface states.

4.4 Conclusion

The measurements outlined in this chapter represent the first transport signatures of Fermi arc surface states. Although they are a necessary consequence of the topological nature of Cd_3As_2, and indeed all topological semimetals, observing them has proven extraordinarily challenging. Topological states such as these have been proposed as a possible route to

scalable quantum computing. Realizing this, and other applications, however, first requires that these states are well characterized and their dynamics are understood. The observation of the Weyl orbit in Cd_3As_2 is the first step.

Chapter 5

Surface States in the TaAs-class of Weyl semimetals

5.1 Motivation and previous results

With the observation of Fermi arc surface states in Cd_3As_2 microstructures, a natural extension was to use the FIB to look for surface states in other classes of topological materials. The first and most well-known example of Weyl semimetals is the TaAs-class of transition metal monopnictides (TaAs, TaP, NbAs, NbP). Compared to Cd_3As_2, ab initio calculations show these compounds to possess a much more complicated band structure with 12 pairs of Weyl nodes in the bulk, in addition to non-topological bands [57]. The lack of inversion symmetry in the $I4_1md$ (No. 109) space group means that any band crossings must be Weyl and not Dirac. These Weyl nodes were shown to come in two symmetry distinct types: W1 with four Weyl pairs located towards the exterior of the Brillouin zone, and W2 with eight Weyl pairs located towards the interior of the Brillouin zone. Because of the larger number and more complex nature of the Weyl nodes in these compounds, Fermi arcs should be present on every crystal surface. However, because the crystal lacks inversion symmetry, the Fermi arc structure will depend heavily on the surface involved and was found to be very different for the cation-terminated (Ta,Nb) and anion-terminated (As,P) [001] surfaces [58]. In practice, the anion-terminated surface was found to be much more prevalent giving the Fermi arcs a spoon-and-bowtie geometry [29, 30, 31]. In addition to Fermi arcs, trivial surface states were also found to be present on the [001] surface, further complicating the band structure.

The bulk bandstructure of TaAs consists of 16 small, Weyl, electron-like W2 Fermi pockets, 8 larger, Weyl, electron-like W1 pockets, and 8 intermediate, non-topological, hole-like pockets. The [001] surface is found to have two Fermi arcs connecting each of the doubly-degenerate projections of the W2 nodes in a spoon-like shape, and a Fermi arc connecting each of the non-degenerate projects of the W1 nodes in a bowtie-like shape [58]. Trivial surface states are also present. All the bands are found to have large mobilities due to their

low effective masses. As a result, quantum oscillations from all can be observed in moderate magnetic fields. These pockets are highly anisotropic, resulting in oscillation frequencies that are strongly angle-dependent. The lowest frequencies are observed with the field along the crystallographic [001] direction.

Although TaAs was first theoretically predicted to be a Weyl semimetal, its topological nature has been verified by STM and ARPES [59]. ARPES measurements found evidence for linear dispersions at the W1 and W2 Weyl points as well as Fermi arcs connecting these points [29, 31, 33]. STM experiments found evidence for the Fermi arc surface states through quasiparticle interference measurements, which showed the dispersion of the surface states to be closely in line with those calculated by DFT [60]. Because of the large electron mobilities in the TaAs family of compounds, transport and magnetization measurements observe large dHvA and SdH oscillations, allowing the bulk Fermi surfaces to be mapped out. However, due to the multiband nature of the system, Landau level fan diagrams showing a non-trivial Berry's phase can not be reliably produced and direct transport signatures of Fermi arc surface states are lacking. As a result, direct transport measurements showing Fermi arcs, akin to those done in Cd_3As_2, are highly desirable.

5.2 Chemical vapor transport

Because of the high melting point of tantalum (and niobium), the flux growth method used in Section 4.2 would require temperatures beyond those ready achievable in the laboratory. Instead, the chemical vapor transport (CVT) method of crystal growth was used. In this method, a volatile transport agent, often a halogen, is used in tandem with a thermal gradient to mediate a reaction producing single crystals of a target compound. This process is illustrated in Figure 5.1 for the specific reaction of TaAs. A precursor power is made from powdered forms of the elements composing the target compound in a solid state reaction. This powder is added to the transport agent and placed into one end (the source) of an evacuated and sealed quartz ampule. The ampule is placed into a two-zone furnace that maintains a temperature gradient between the two ends of the tube. Both temperatures must be sufficiently high for the transport agent to evaporate and become gaseous. Moreover, when the transport agent reacts with the precursor powder, the products of that reaction must be gaseous as well.

The gaseous products of the vapor transport reaction will diffuse from the source end of the tube to the sink end through a temperature gradient. There, the change in temperature will favor the reverse CVT reaction. The products will disassociate into the transport agent and the target compound, which will be deposited into single crystals. The transport agent will then diffuse back to the source end of the ampule, starting the cycle over again. By holding the ampule in this temperature gradient for several days, single crystals can be formed of compounds whose melting points are too high for more direct growth techniques. A more detailed discussion can be found in Ref. [61].

The choice of transport agent and temperature gradient will depend sensitively on the

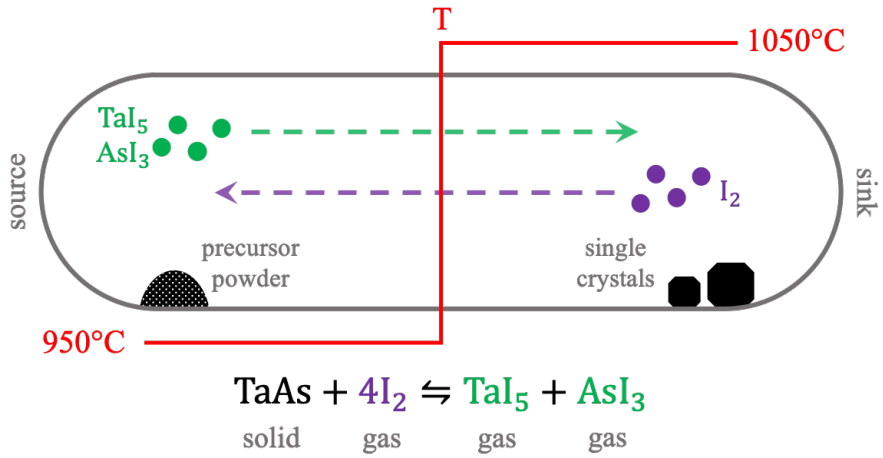

Figure 5.1: **The chemical vapor transport reaction.** The solid precursor powder (black) on the left (source) end of the quartz ampule reacts with iodine (purple), the transport agent to form TaI_5 and AsI_3, both gaseous species (green). The products diffuse to the right (sink) end of the tube where the reaction runs in reverse, depositing the TaAs into crystals (black). The iodine gas then diffuses back to the source to continue the reaction. The ampule was held in this temperature gradient for 14 days.

specifics of the reaction being run. The transport agent must be chosen such that both it and the reaction products will be gaseous at the furnace temperatures. Moreover, the CVT reaction must be reversible, proceeding preferentially in the forward direction on the source end of the tube and in the reverse direction on the sink end of the tube [62]. If the equilibrium is shifted too far to one side or the other, the temperature gradient will not be enough to reverse the reaction to any significant degree, and an unrealistic amount of time will be required to obtain sizable crystals. Typically, the reaction equilibrium constant, K_p, should be in the range $10^{-4} < K_p < 10^4$ at the midpoint of the tube [63]. K_p can be calculated from the Gibbs free energy by

$$\Delta G = -RT \ln K_p \tag{5.1}$$

where ΔG is the change in the Gibbs free energy from reactants to products, R is the universal gas constant, and T is the average temperature of the two-zone furnace. If the chemical reaction and enthalpies of formation are known, calculating the equilibrium constant can help determine the optimal transport agent and thermal gradient to use for a given target compound.

One consequence of Eq. 5.1 is that the direction of the thermal gradient will depend on whether the CVT reaction is endothermic or exothermic. In an endothermic reaction, an increase in temperature will shift the reaction equilibrium towards the reaction products. Therefore, the high temperature should be on the source end of the ampule, where the

products are desired, and the low temperature on the sink end, where the reactants are desired. In an exothermic reaction, the opposite is true: an increase in temperature will favor the reactants. Therefore, the source and sink should be held at low and high temperatures, respectively, and the gradient is reversed. The temperature gradient in Figure 5.1 is shown for an exothermic reaction.

In the specific case of TaAs, iodine was used as the transport agent. The precursor powder was grown by sealing a stoichiometric mixture of arsenic and tantalum powder in a quartz ampule under vacuum. The ampule was heated to 1100°C and held there for 4 days to allow the precursors to completely react. The resulting powder was confirmed to be TaAs in the $I4_1md$ (No. 109) space group by powder x-ray diffraction. The TaAs powder was then mixed with 2.5 mg/cm^3 of iodine in a sealed ampule and loaded into a two-zone furnace. The source end of the furnace was held at 950°C and the sink end at 1050°C for 14 days. The reaction driving the CVT process is [64]

$$\mathrm{TaAs(s)} + 4\mathrm{I_2(g)} \rightleftharpoons \mathrm{TaI_5(g)} + \mathrm{AsI_3(g)} \tag{5.2}$$

At the source end of the tube, the reaction equilibrium is shifted towards the right-hand side, driving the reaction in the forward direction. At the sink end of the tube, the change in temperature shifts the equilibrium to the left-hand side, driving the reverse reaction. In this manner, the TaAs powder is reacted on the source end, then diffuses to the sink end where it is deposited into single crystals. Well-faceted crystals up to 3mm per side were obtained and their structure was confirmed with x-ray diffraction. A typical crystal is shown in Figure 5.2a.

5.3 FIB microstructuring and superconductivity

The project goal was to microstructure transport devices of TaAs and directly observe the Fermi arc surface states in a similar manner to Cd_3As_2. Crystals were mounted and fabricated into transport devices using the FIB. A typical device is shown in Figure 5.2b. It is a multi-terminal resistivity bar produced from a lamella of TaAs. Similar devices were fabricated from the entire TaAs family of compounds (TaAs, NbAs, TaP, NbP). Figure 5.2c shows the measured resistivity as a function of temperature. At low temperature, all the samples became superconducting with transition temperatures ranging from 2-4K. Superconductivity has not been observed in bulk crystals, indicating that the FIB fabrication process has changed the material composition in some way.

In order to elucidate the origins of the superconducting state, a NbAs device was successively thinned down, with resistivity measurements performed at each thickness. The resistivity was found to be strongly thickness dependent. This would not be expected from a bulk conduction channel, where the total device resistance should scale geometrically with the thickness, and the resistivity should remain constant. Instead, a thickness-dependent resistivity would be expected for a surface conduction channel that would not scale with the device geometry. Evidence for the presence of such a channel comes from SRIM calculations,

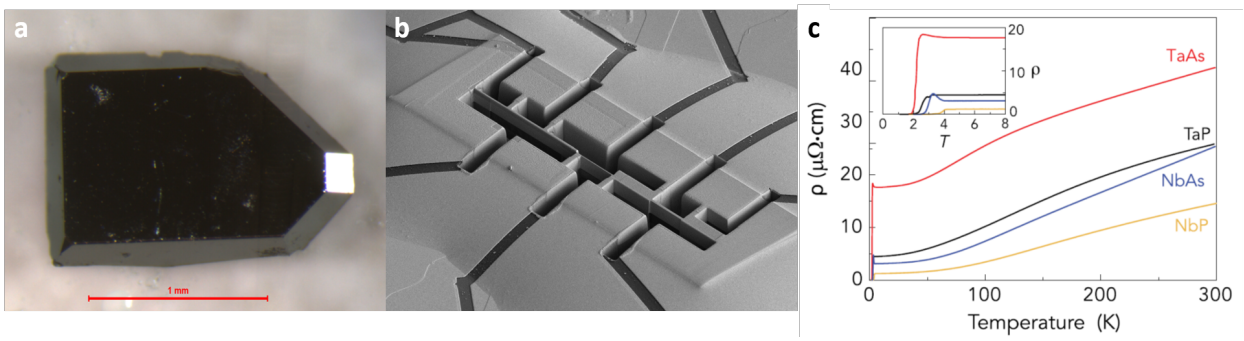

Figure 5.2: **TaAs bulk crystal, FIB device, and superconductivity.** (a) A typical TaAs crystal grown via the described chemical vapor transport method. (b) A FIB fabricated resistivity bar device. (c) Resistance as a function of temperature for FIB fabricated devices of TaAs and related compounds. All exhibit superconductivity at low temperature (inset), likely due to an excess of tantalum or niobium on the device surface. Adapted from Ref. [5].

	TaAs	**NbAs**	**TaP**	**NbP**
Ta/Nb	4.86	5.07	5.11	5.39
As/P	26.38	24.23	10.17	9.82

Table 5.1: **Sputtering yields per incident 60keV Ga^{2+} ion at grazing incidence.** For all compounds, the pnictide is preferentially sputtered leaving an excess of Ta/Nb on the device surface.

which show that the pnictide element (As, P) is preferentially sputtered compared to the transition metal (Ta, Nb), as might be expected from the large difference in sublimation temperatures. Table 5.1 shows the SRIM results. For 60keV Ga^{2+} ions at grazing incidence, 4.8 arsenic atoms are sputtered for every niobium atom. This leaves a large excess of niobium in the surface layer of the FIB devices. Although this layer is amorphous, superconductivity has been observed in amorphous sheets of niobium with a similar transition temperature to what was observed [65].

A confirmation of the surface conduction layer comes from the observed magnetoresistance. The magnetoresistance rolls over and appears to saturate at high fields, as shown in Figure 5.3. Bulk NbAs, like the rest of the TaAs family, exhibits a conventional quadratic magnetoresistance for fields applied along the a-axis, however. This behavior can be well explained using a parallel conduction model with contributions from both the bulk and the surface. The magnetoconductivity of bulk NbAs is given by the usual quadratic form $\sigma_{bulk} = 1/(aH^2 + c)$, where c is a constant. Because the surface layer is disordered, it can be modeled by a constant conductivity that is field-independent, σ_{surf}. As shown in Figure 5.3a, the combined conductivity, $\sigma = \sigma_{bulk} + \sigma_{surf}$, is an excellent fit to the data and yields a surface resistivity of 16.7 $\Omega/\square$. This value is in close agreement with what has been observed

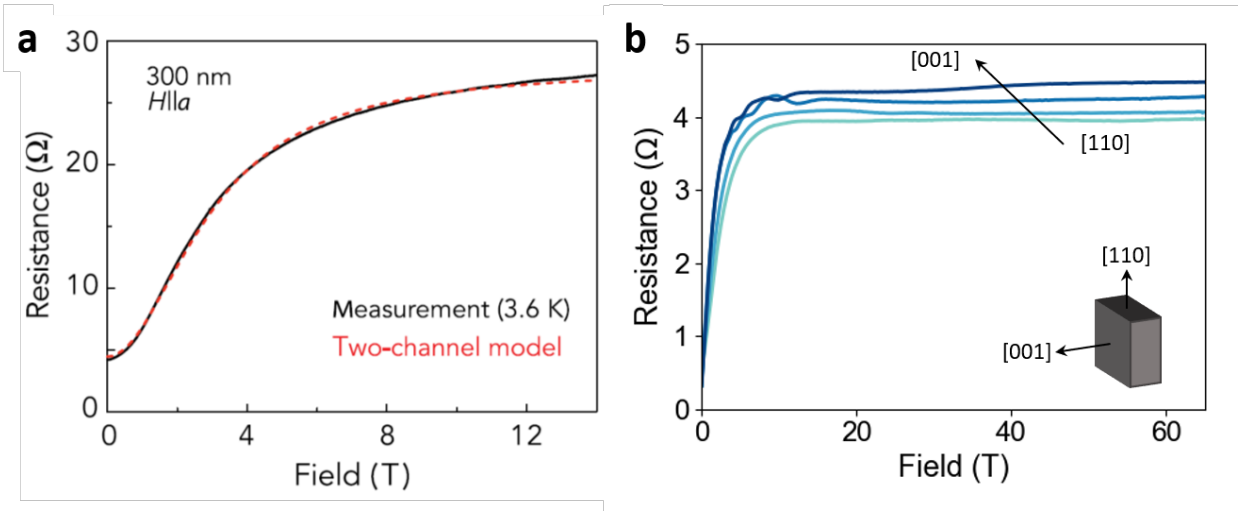

Figure 5.3: **Surface conduction and high field magnetoresistance.** (a) A 300nm NbAs FIB device shows a rollover in the magnetoresistance, a deviation from the quadratic behavior observed in bulk samples. The resistance can be well fit with a parallel conduction model assuming a field-independent surface conductance. Adapted from Ref. [5]. (b) High field measurements on a 270nm TaAs device show no indication of surface oscillations stemming from Fermi arcs at any angle. The oscillations observable at intermediate fields can be well explained by the bulk Fermi surface. At high fields, the bulk is nearly completely short circuited by the conducting surface and even the bulk quantum oscillations are suppressed.

in irradiated thin films of niobium [65].

Although conduction at high fields in these devices is dominated by the surface FIB-irradiated layer, signatures of the bulk Fermi surface remain. Specifically, quantum oscillations were observed in intermediate fields (7-14T) with a frequency of 85T. This frequency agrees with what is observed in bulk NbAs with field along the a-axis. Three conclusions can be drawn from the presence of these SdH oscillations. First, the crystallinity is preserved in the bulk of the material. Although the FIB causes significant damage and alterations to stoichiometry, the damage is confined to the surface layer, leaving the bulk intact. Second, the agreement between the SdH frequency observed in the FIB devices and previous measurements in bulk samples indicates that the bulk of the sample has not been doped by the FIB, further evidence that the FIB technique only affects the surface layer. Finally, although the surface layer of the device is highly conductive, it has not completely shorted the bulk. This raises the prospect that the original goal of these devices, namely the measurement of Fermi arc surface states, may still be possible.

SdH oscillations from the bulk of NbAs were observable at 14T and 2K, additional oscillations expected from Fermi arc surface states were not. This could be due to these states having a larger effective mass than the bulk, or the increased scattering expected at the surface. The former would require lower temperatures, and the latter higher magnetic fields.

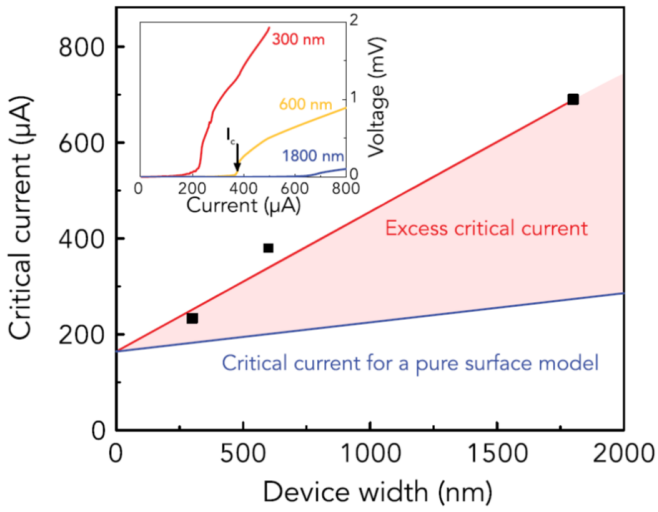

Figure 5.4: **Critical current scaling with device width.** The critical current does not directly scale with the surface area of the device, as would be expected for a supercurrent carried exclusively by the surface. Instead, there is an "excess" critical current which may indicate that some of the supercurrent is carried in the bulk. If so, this would be an example of proximity induced superconductivity in a Weyl semimetal and may provide a route to the realization of Majorana fermions. Adapted from Ref. [5].

In order to achieve both of these conditions, the FIB devices were taken to Los Alamos National Laboratory to perform pulsed field measurements up to 65T at 300mK. The measured resistivity in a TaAs device of 270nm width is shown in Figure 5.3b. Although pronounced SdH oscillations can be seen below 20T, they are in close agreement with what has been observed from the bulk Fermi surface. Additional oscillations, however, were not observed. Not only are additional oscillations from potential surface states not present, but the oscillations from the bulk appear to be suppressed at higher fields. This is the opposite of what would normally be expected. Moreover, the resistivity is almost flat from 20T onward. All three of these observations are consistent with the surface layer carrying almost all of the current as the resistivity of the bulk increases with field. Either the oscillations from the Fermi arc surface states are too small to measure in parallel with the highly conductive surface, or the Fermi arcs themselves have been damaged by the FIB milling process. In either case, the conclusion is that the FIB technique, although successful in Cd_3As_2, cannot be used to measure the surface states in the TaAs-family of Weyl semimetals.

Although FIB fabrication was not successful in measuring the topological surface states in TaAs, it may be useful in creating interfaces at which to study topological superconductivity. If topologically protected surface states can be made superconducting through the proximity effect, they may host Majorana modes [66]. These elusive states are their own antiparticles and are predicted to be one route to implementing quantum computation [67]. Although

evidence of Majorana edge modes is not present in these measurements, the dependence of critical current on device width, as shown in Figure 5.4, does not scale with the circumference of the device, as would be expected for a purely surface superconductivity. Instead, an excess critical current is observed, indicating that the bulk NbAs may be carrying some of the supercurrent. If so, then this might be an example of topological superconductivity and FIB fabrication may be an ideal technique for making such systems. Further measurement is required to elucidate the exact nature of the superconductivity in these devices.

5.4 Mechanical polishing and SdH oscillations

In order to avoid the surface damage caused by FIB fabrication, mechanical polishing were used instead. Crystals of TaAs were cut and polished into Hall bars ranging from 14 µm to 272 µm, with the main face normal to the [001] crystallographic axis. Figure 5.5 shows the magnetoresistance from one such device. At 2K, pronounced SdH oscillations can be observed on the non-saturating background typical of these materials. A Fourier analysis of this data yields oscillatory frequencies of 7.3T and 19.9T, in close agreement with frequencies previously reported for the W1 and H1 pockets in bulk TaAs [57]. Moreover, because of the change in fabrication methods, superconductivity was no longer present down to 1.8K. Subtraction of a high temperature (10K) background from the 2K magnetoresistance, however, reveals the presence of an additional, subtle SdH oscillation onsetting at approximately 8T. This oscillation has a frequency of 285T and has not been previously reported by any study of TaAs. Moreover, band structure calculations do not show any bulk Fermi surfaces large enough to produce such a frequency, hinting that it may instead come from a surface contribution.

The angle dependence of the 285T frequency is shown in Figure 5.6 and shows clear indications of being two-dimensional in origin. As the field is tilted away from the [001]-axis and into the plain of the Hall bar, the oscillatory frequency is observed to increase and the onset of the oscillations moves to higher field. Specifically, if the frequency is plotted as a function of field angle, it is found to be well-fit by a $1/\cos\theta$ dependence, consistent with what would be expected from a two-dimensional or cylindrical Fermi surface. The two-dimensional nature of this orbit has been confirmed in multiple devices along multiple rotation axes, as summarized in Figure 5.8. Moreover, the dispersion of the bulk oscillations is consistent with previous results, indicating that the additional frequency does not stem from a doping or crystal growth issue and is instead intrinsic to thin TaAs devices.

The temperature dependence of the 285T SdH oscillation is shown in Figure 5.7. As expected, the amplitude of the oscillation decays as a function of temperature and can be well-fit by the Lifshitz-Kosevich thermal damping factor. A fit of the 7.3T bulk frequency yields an effective mass of $0.066\mathrm{m}_e$, in close agreement with values previously observed and predicted by band structure calculation [57]. A fit to the 285T frequency, on the other hand, yields a much larger effective mass of $0.5\mathrm{m}_e$. As will be discussed, this large effective mass can be explained by a unique surface orbit involving multiple Fermi arcs.

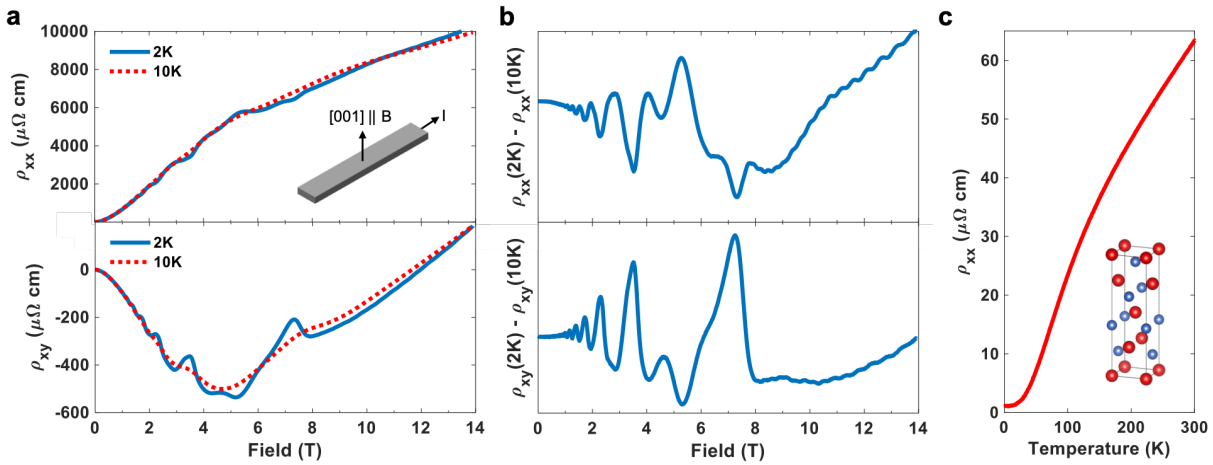

Figure 5.5: **A new oscillation in TaAs.** (a) The longitudinal (upper) and Hall (lower) resistivities of a polished 33 µm Hall bar device at 2K (blue) and 10K (red, dotted) with field applied along the [001] direction, normal to the plane of the device. (b) The 2K resistivities from panel (a) with the 10K curves subtracted. An additional oscillation can be observed, onsetting around 8T with a frequency of 285T. (c) The resistivity shows metallic behavior down to 1.8K with a residual resistivity ratio of 56. No superconductivity is observed. The crystal structure of TaAs is shown in the inset, with tantalum atoms in red and arsenic in blue. Adapted from Ref. [4].

Although the reproducibility of the 285T oscillation suggests an intrinsic origin, several likely impurity phases were considered and subsequently ruled out as possible origins. The most likely impurity phases in TaAs would be elemental tantalum, elemental arsenic, the binary compound $TaAs_2$, and a predicted hexagonal phase of TaAs. In all three cases, the known SdH frequencies are either far from 285T, the crystal symmetries are inconsistent with the observed angle dependence, and/or the effective masses do not agree with that measured. Elemental tantalum shows quantum oscillations at much higher frequencies than what was observed, with frequencies above 2700T for all field angles [68].

Elemental arsenic shows SdH frequencies in the same range as those observed [69]. The alpha and beta Fermi surfaces both show oscillations crossing 285T as a function of field angle. Elemental arsenic, however, can be eliminated as the cause of the observed 285T oscillation for three reasons. First, both the pockets that show a 285T oscillation only exhibit that frequency at a specific field angle and have global minima at lower frequencies, at 139T and 213T for the alpha and beta pockets, respectively. During extensive rotations in field, the TaAs devices never show high frequency oscillations below 285T. Second, arsenic has a six-fold rotational symmetry in the ab-plane. The observed 285T frequency, however, never show a six-fold symmetry in multiple devices rotated along multiple orthogonal directions. Finally, the effective masses of the alpha and beta pockets in arsenic are $0.098m_e$ and $0.13m_e$,

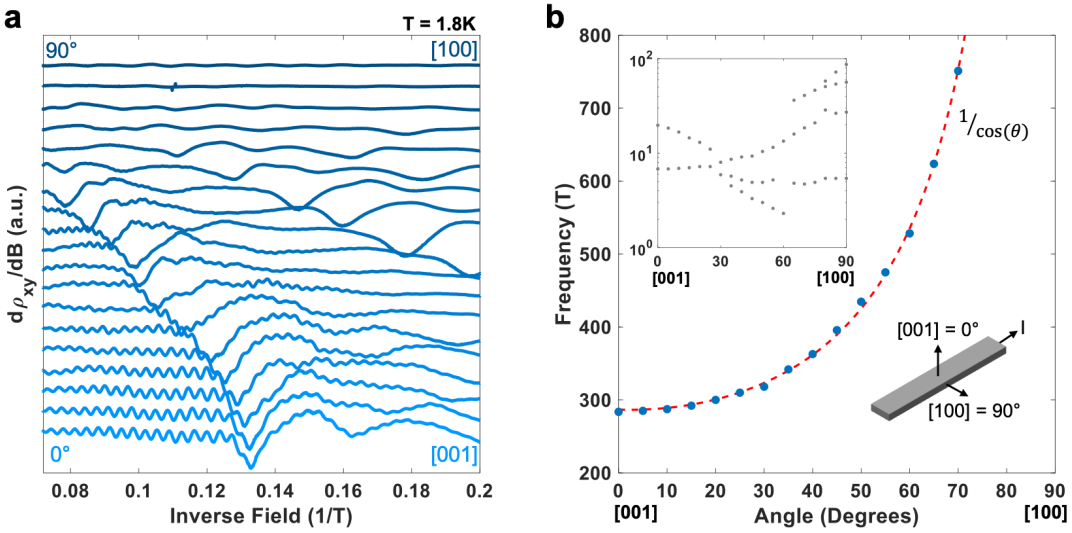

Figure 5.6: **Angle dependence.** (a) The derivative of the Hall resistivity is plotted against inverse magnetic field at various angles. As the field is rotated into the plane of the device, the oscillations increase in frequency and move to higher field. (b) The angle dependence of the oscillatory frequency shows the characteristic $1/\cos(\theta)$ dependence associated with a two-dimensional cyclotron orbit. Inset: The angle dependence of the low frequency SdH oscillations is in good agreement with what has been measured in bulk samples of TaAs [57]. Adapted from Ref. [4].

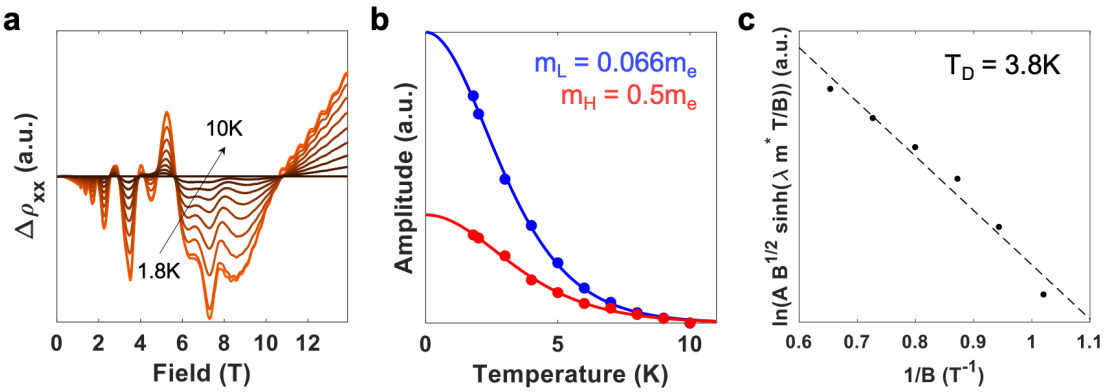

Figure 5.7: **Temperature dependence and effective mass.** (a) The temperature dependence of the SdH oscillations with field along the [001] axis and a 10K background subtraction. (b) The oscillatory amplitude can be well-fit by the standard Lifshitz-Kosevich thermal reduction factor and yields an effective mass of $0.066m_e$ for the low-frequency bulk oscillations and $0.5m_e$ for the high-frequency surface oscillations. (c) A Dingle analysis of the bulk SdH oscillations gives a Dingle temperature of 3.8K corresponding to a quantum lifetime of 0.32ps. Adapted from Ref. [4].

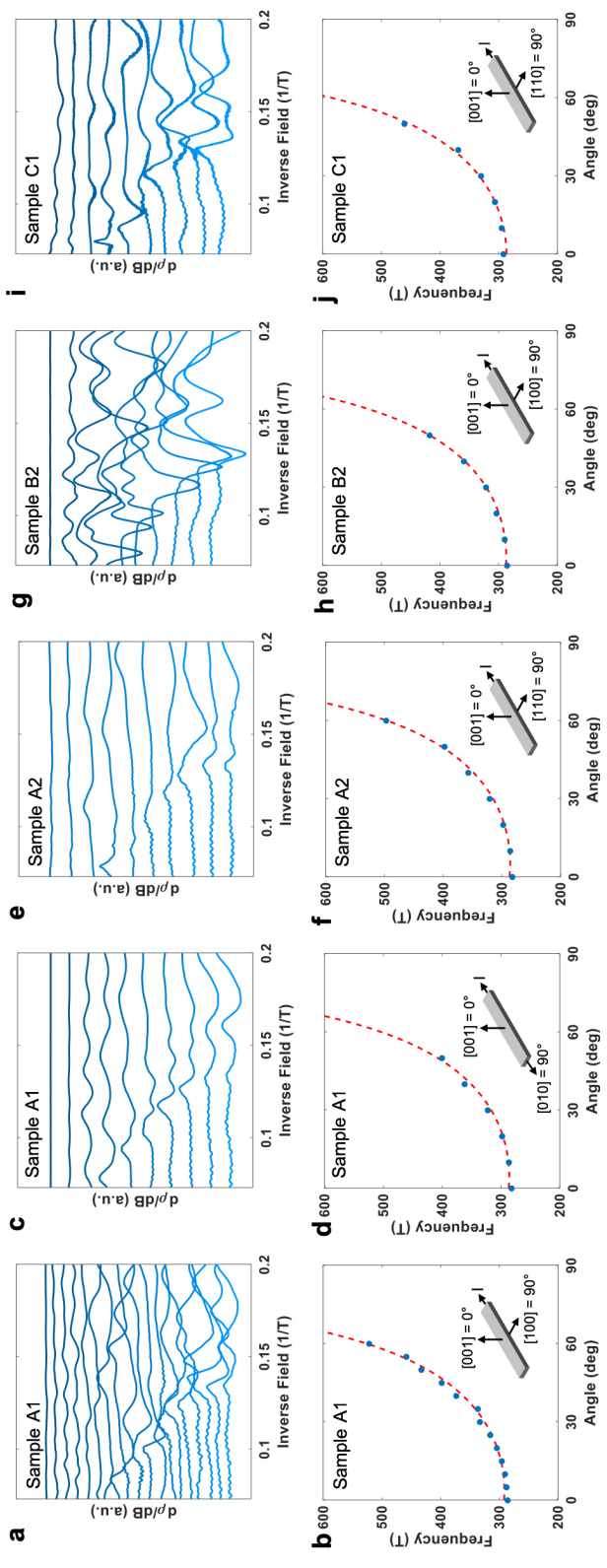

Figure 5.8: **Additional samples and rotation axes.** Additional Hall bar devices fabricated from different TaAs samples. The 285T frequency oscillation is consistently observed with field along the [001] axis and disperses as $1/\cos(\theta)$ along all field rotation directions. Adapted from Ref. [4].

significantly lower than the measured mass $0.5m_e$ for the 285T oscillation in TaAs.

Similarly to arsenic, $TaAs_2$ shows quantum oscillations from two principal Fermi pockets [70]. The frequencies of these pockets, however, are significantly lower than the 285T oscillation observed in TaAs. The alpha and beta pockets have frequencies of 104T and 130T with field along the c-axis, decreasing to 100T and 50T when rotated into the ab-plane. Additionally, the effective masses in $TaAs_2$ are $0.083m_e$ and $0.078m_e$, much lower than what was measured in TaAs.

Although it has not been experimentally confirmed, a hexagonal phase of TaAs is predicted to be stable under pressure [71]. The presented samples are not under pressure, but it may be possible that small impurity domains of this hexagonal phase have been stabilized and may be contributing to the SdH spectrum. However, the 285T frequency is not observed to be six-fold symmetric along any rotation axis, a requirement for a hexagonal lattice. Moreover, DFT calculations predict an SdH frequency of approximately 100T for the hexagonal phase, much lower than the 285T observed.

Finally, it has been reported that planar defects, primarily in the form of stacking faults, can occur in crystals of TaAs [72]. Band structure calculations show these defects to primarily change the location of the Fermi energy, appearing as an effective doping. The measured bulk quantum oscillation spectrum in the FIB devices, however, agrees with what has been observed in the literature implying that the Fermi energy is not significantly different than those measured previously. Moreover, one would expect defects, such as stacking faults, to be evenly distributed throughout the crystal. This would not result in a systematic thickness dependence to the magnetotransport, as observed in the Hall bar devices (see Figure 5.10).

Finally, extensive powder and single crystal diffraction studies were performed, including using micro-Laue to scan with micron resolution across the active area of several devices. Laue diffraction patterns were obtained using broadband x-rays focused to a 1µm spot. The spot was scanned across the sample to obtain spatially-resolved diffraction patterns. The observed peaks could be well-indexed by TaAs and no patterns corresponding to impurity phases were observed. Figure 5.9 shows the summed diffraction image obtained from a 100µm × 100µm scan with a 2µm step size of the active area of one of the transport devices exhibiting the 285T oscillations. The image was generated by averaging 2500 individual Laue images. The peaks can all be indexed by TaAs and the lack of stray peaks indicates that no impurity phase is present over this 10,000μm^2 area. Similarly, powder diffraction did not reveal any peaks that could not be indexed by TaAs, confirming the single-phase nature of the samples.

5.5 Signatures of Fermi arcs

With impurity phases ruled out, one possible origin of the 285T frequency is the surface of TaAs. High-mobility, two-dimensional surface states would be a natural explanation of the $1/\cos(\theta)$ dispersion observed in the angle dependence. In order to evaluate whether the surface is playing a role in the transport, a thickness dependence was performed. A TaAs Hall

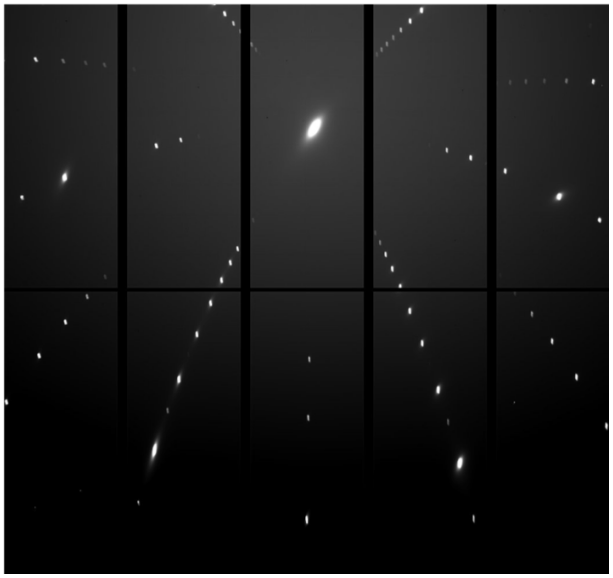

Figure 5.9: **Integrated Laue diffraction pattern.** A Laue diffraction pattern taken by scanning a 1 µm x-ray spot across a device and summing the 2500 resulting individual patterns. All peaks can be fit by TaAs with no impurity phases observed.

bar was polished to 272 µm, 130 µm, 43 µm, and 14 µm with magnetoresistance measurements performed at each successive thickness. As shown in Figure 5.10, both the longitudinal and Hall resistivities show a strong thickness dependence, immediately suggesting a surface contribution.

Although complicated, the thickness dependence can be effectively modeled using a parallel channel conductance model incorporating both bulk and surface contributions to the resistivity. Specifically, four contributions to the conductivity were assumed: bulk electrons, bulk holes, surface electrons, and surface holes. Although the true band structure is significantly more complicated, involving multiple pockets of each carrier type, this minimal model captures some of the essential features of the thickness dependence. The conductivity tensor of each carrier type is assumed to take the semiclassical form

$$\sigma = \frac{n|e|\mu}{1+(\mu B)^2}\begin{bmatrix} 1 & \pm\mu B \\ \mp\mu B & 1 \end{bmatrix} \tag{5.3}$$

where n is the carrier density, e is the electron charge, μ is the carrier mobility, B is the applied magnetic field, and $\pm$ denotes holes or electrons, respectively. The fitting parameters used are shown in Table 5.2. The bulk is partially compensated, consistent with what has been observed in other measurements [57, 73]. The surface is also close to compensation, with much lower mobilities than the bulk. This would be expected from polishing-induced damage that might cause additional scattering on the surface. SdH oscillations were incorporated by adding a Lifshitz-Kosevich oscillatory term to the diagonal elements of the conductivity tensor to simulate the 7.3T oscillations of the bulk W1 Fermi pocket.

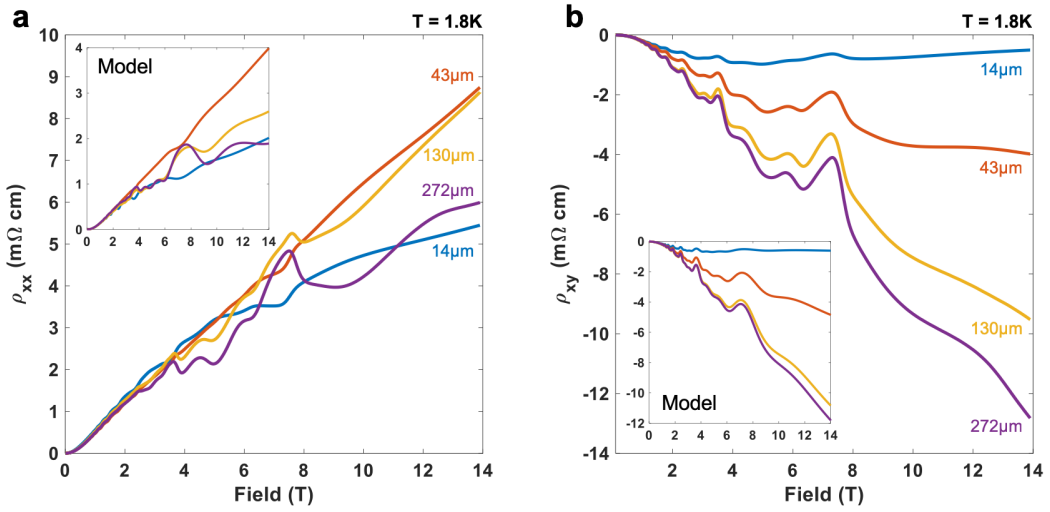

Figure 5.10: **Thickness dependence.** Longitudinal (a) and Hall (b) resistivities show a non-trivial thickness dependence. Resistivities were calculated using bulk geometrical factors. For a purely bulk conductivity, this would cause the curves to collapse. In addition, the SdH oscillations in the transverse magnetoresistivity appear to show a phase inversion between the 14 µm/43 µm devices and the 130 µm/272 µm devices. Insets: The thickness dependence can be well-modeled with a parallel channel conductance model incorporating both surface and bulk contributions to device resistance. This model captures the overall shape and ordering of the resistivity curves and the phase inversion of the SdH oscillations. Adapted from Ref. [4].

The model captures the thickness dependence shown in Figure 5.10 through a geometry-driven difference in scaling between the surface and the bulk. As the sample is thinned, the surface plays a proportionally larger role, leading to a systematic change in the net carrier concentration and a decrease in the Hall resistivity. This, in turn, changes the proportion of the current carried by the surface, leading to the complicated thickness dependence observed in the longitudinal resistivity. Although this is a very simple minimal model, the calculated resistivities closely reproduce the features of the measured data with the parameters summarized in Table 5.2.

One specific feature that is captured is the phase inversion of the bulk oscillations between the 43 µm and 130 µm devices in the longitudinal, but not Hall channel. The oscillation at 7T, for example, appears as a peak in the longitudinal resistivities of the 272um and 130um devices, but a trough in the 43um and 14 um devices. In the Hall resistivities, on the other hand, the same oscillation appears as a peak for all thicknesses. This thickness-dependent phase inversion is well captured by the model. Similar phase inversions have

	Electron Density	Hole Density	Electron Mobility	Hole Mobility
Bulk	$6.9 \times 10^{18}\text{cm}^{-3}$	$6.2 \times 10^{18}\text{cm}^{-3}$	$100,000\text{cm}^2/\text{Vs}$	$30,000\text{cm}^2/\text{Vs}$
Surface	$5.6 \times 10^{15}\text{cm}^{-2}$	$6.1 \times 10^{15}\text{cm}^{-2}$	$570\text{cm}^2/\text{Vs}$	$600\text{cm}^2/\text{Vs}$

Table 5.2: **Modeling parameters.** The carrier densities and mobilities used to model the surface contribution to the transport.

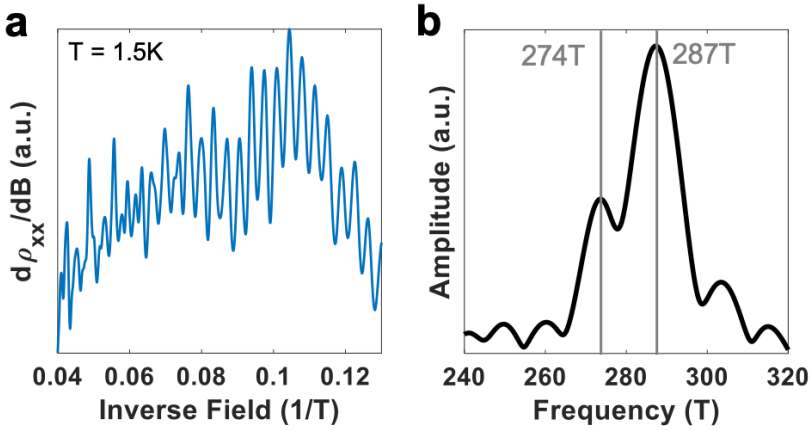

Figure 5.11: **High field transport.** (a) Above approximately 14T additional structure can be observed in the high frequency SdH oscillations. (b) A Fourier transform shows two frequencies, 274T and 287T, emerging at high field. Adapted from Ref. [4].

been observed in samples of elemental bismuth and antimony [74, 75]. They are understood as a competition between diagonal and off-diagonal terms of the conductivity tensor. As the devices are thinned, the larger influence of the surface changes the strength of the Hall conductance relative to the longitudinal conductance, leading to the change of phase in the SdH oscillations. The fact that this phase change is also captured by the model is strong evidence of the influence of surface conduction on the overall conductivity.

In order to observe the evolution of the 285T oscillation, the samples were measured in pulsed fields up to 60T. Below 14T, the oscillations appear fully periodic in inverse field with a frequency of approximately 285T, as previously noted. Above 14T, however, additional peaks emerge and the oscillation begins to show a beating pattern (Figure 5.11). A Fourier transform shows that two distinct frequencies at 274T and 287T can be resolved. These two frequencies can be traced to a unique Fermi arc interference orbit that may be present in this system.

ARPES experiments and DFT calculations can help elucidate the origin of the surface oscillations. Figure 5.12 shows a schematic of the electronic surface structure of the [001]

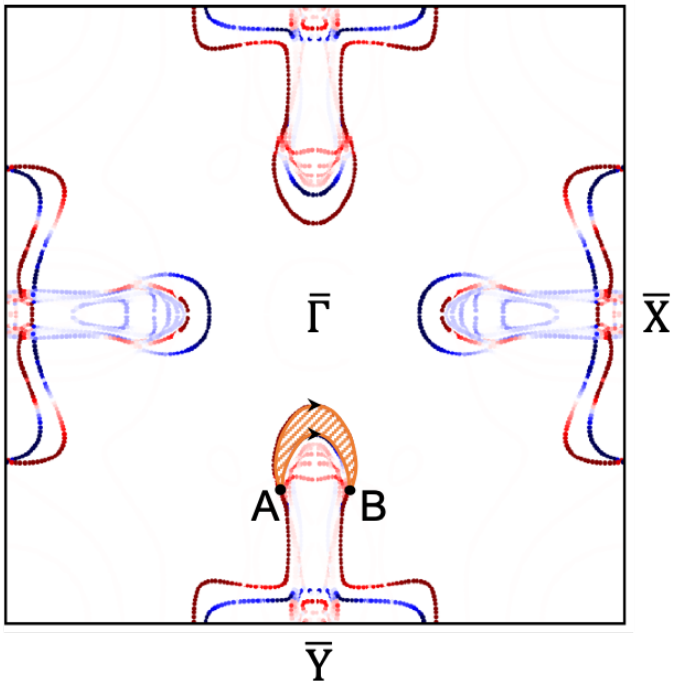

Figure 5.12: **Theoretical expectations from quantum interference orbits involving Fermi arcs.** A DFT band structure calculation showing trivial and Fermi arc surface states on the [001] surface of TaAs. The interference orbit between two adjacent Fermi arcs is highlighted in orange. The area enclosed agrees closely with the SdH oscillation frequency observed in transport. The orbit near $\overline{X}$ is 7% larger than the equivalent orbit near $\overline{Y}$, in remarkable agreement with the frequency splitting observed at high fields (Figure 5.11). Adapted from Ref. [4].

As-terminated surface of TaAs. Although Weyl orbits involving individual Fermi arcs and traversing the bulk, as observed in Cd_3As_2 in Chapter 4, would be a natural explanation of the oscillations in TaAs, the expected frequencies would be much higher than observed. Moreover, coherent orbits from Fermi arcs on opposite surfaces require the traversal of the bulk and since these samples are not FIB fabricated and therefore significantly thicker than the quantum mean free path ($\lambda \sim 0.1\mu$m) it seems highly unlikely that coherent orbits of this sort can form [24].

However, one orbit that matches the observations corresponds to the cyclotron path connecting two different Fermi arcs on a single surface, as illustrated in Figure 5.12. Such an orbit involves an interband transition from one arc to another, a process known as magnetic breakdown that is observed in materials with nearly degenerate bands near the Fermi energy [76, 13, 77]. What is especially unusual about this orbit is that it is semiclassically forbidden; it involves electrons traveling opposite to the Lorentz force along one of the arcs. Such orbits are known to appear by Stark interference, the interference of two coherent cyclotron

trajectories, and have been observed in magnesium and certain organic superconductors [78, 79, 80]. In essence, the quantum mechanical phase of the particles interferes as they are transmitted and reflected at the junctions where the arcs terminate.

To see that interference orbits can lead to quantum oscillations, consider a particle at position A in Figure 5.12, at the left junction of the two arcs. If the particle travels to position B along the top or bottom arc, it will pick up an Aharonov-Bohm phase from the field enclosed by the associated real-space trajectory, $\phi = \frac{e}{\hbar}\int \vec{A}\cdot d\vec{l}$, where $\vec{A}$ is the vector potential. The phase difference between the two paths leads to interference of the wavefunction where the paths rejoin at point B. As a result, the total probability amplitude will be of the form $T \sim \cos(\phi_{top} - \phi_{bottom}) = \cos(\frac{e}{\hbar}\oint \vec{A}\cdot d\vec{l})$, where the integral is over the real-space path enclosed by the two Fermi arcs. By Stokes theorem, this path integral can be converted to a surface integral over the area enclosed, and the real space area, A_r, can be converted into a k-space area, A_k, by $A_k = (\frac{eB}{\hbar})^2 A_r$. Therefore, as a result of the quantum interference of the paths, the probability amplitude becomes $T \sim \cos(\frac{\hbar A_k}{eB})$. This is of the exact same form as SdH oscillations with a frequency $F = \frac{\hbar A_k}{2\pi e}$, where A_k is now the area enclosed between the two Fermi arcs. A more detailed derivation is available in Ref. [81].

A_k estimated from ARPES measurements ($A_k \sim 0.026\text{Å}^{-2}$) is consistent with DFT calculations, and corresponds to a frequency of 277T, in close agreement with the observed 285T [30]. This is also consistent with previous DFT calculations of the Fermi surface reported in Refs. [82, 60]. Additionally, from different energy cuts, the cyclotron effective mass can be estimated by $m^* = \frac{\hbar^2}{2\pi}\frac{\partial A_k}{\partial \epsilon}$, and is found to be approximately 0.4m_e, in reasonable agreement to the observed effective mass of 0.5m_e. Given that no other surface or bulk states of TaAs, let alone known impurity phases, have masses close to this value, this agreement is a strong indication that the observed frequency arises from the quantum interference of the Fermi arcs.

The observation of two distinct frequencies at high field is also consistent with the Fermi arc interference orbit. The [001] surface of TaAs breaks the four-fold rotational symmetry of the crystal. As a result, the surface band structure does not have to be the same in the $\overline{\text{X}}$ and $\overline{\text{Y}}$ directions. In fact, the Fermi arcs connecting the W2 Weyl nodes are found to differ slightly in both DFT calculations and ARPES measurements [30]. This difference leads to an approximately 7% change in the area enclosed by the two quantum interference orbits, very close to the 5% splitting of the observed SdH frequencies.

5.6 Conclusion

Surface signatures of the Fermi arcs in Weyl and Dirac semimetals have proven extraordinarily difficult to detect, let alone evidence of coherent orbits among them. The only system in which such orbits have been observed is Cd_3As_2, where the samples lend themselves to microfabrication techniques, allowing device thicknesses to approach the bulk mean free path. In TaAs, observation of these arcs is much more complicated; not only are there many more arcs that intersect in complex ways, but trivial surface states are also present

and the material chemistry prevents the same microfabrication techniques from being used without significantly altering the sample [5]. In this work, mechanically polished samples reveal a new SdH oscillation that sustains electron coherence along a cyclotron orbit. This orbit cannot be explained by any bulk Fermi surface or likely impurity phase. DFT calculations instead show that this orbit quantitatively agrees with a cyclotron path involving the quantum interference of two Fermi arcs on the same surface, distinguishing it from the oscillatory phenomena observed in Cd_3As_2. These observations demonstrate that there are exciting possibilities not only to reveal the transport behavior of the Fermi arcs in high magnetic fields, but to utilize field-driven interferometry as a means to study and employ their topological properties.

Chapter 6

Dirac Electrons in $ZrTe_5$

6.1 Motivation and previous results

Although many materials have been identified as topological and non-topological in recent studies, very few materials appear to exist at the boundary of these two phases. $ZrTe_5$ is one such material that is believed to reside close to such a phase boundary. Because of this proximity, however, its exact topological nature has been hotly debated, having been predicted and verified as a Dirac semimetal [83, 84, 85, 86, 87], a topological insulator [88, 89, 90, 91, 92] and a trivial semiconductor [93] by different studies. The putative topological phase transition (TPT) is thought to be manifested as an unusual peak in the temperature dependence of the resistivity, whose position is strongly sample dependent and ranges between $\sim$ 10K to 150K. Density functional theory calculations suggest this sample dependence arises directly from a (structural) proximity to a TPT [94], and evidence for this has been bolstered by recent angle-resolved photoemission and pressure-dependent transport measurements [95, 96, 97]. Nevertheless, the topological nature of $ZrTe_5$ above and below the resistivity anomaly has remained controversial, highlighting the need for better experimental signatures of topological character.

Previous studies on the Weyl semimetal NbAs found that its topological character could be probed by measuring the sample's magnetization at large magnetic fields [98]. Specifically, topological Weyl and Dirac Fermi pockets will exhibit paramagnetism as they approach the quantum limit, the field at which all electrons are in the zeroth Landau level. This orbital paramagnetism is diminished above the quantum limit and gives way to a background diamagnetism that is usually also present. This cross-over from paramagnetism to diamagnetism at the quantum limit is a signature of topological carriers. Although this phenomenon was first confirmed in NbAs, a previously known Weyl semimetal, it can be used to search for other materials whose topological character is less clear.

In the most general case, all materials show some small degree of orbital diamagnetism arising from the local orbital moment of the ions. Trivial metals show an additional Landau diamagnetism arising from the orbital motion of their itinerant electrons. In topological

materials, however, a paramagnetic response can be observed due to the presence of a chiral Landau level at zero energy. For a massless Dirac fermion in a magnetic field B along z, this is given by

$$\varepsilon_n = v_F\sqrt{2\hbar eB(n+\gamma)+\hbar^2k_z^2}, \tag{6.1}$$

where n is the Landau index and v_F the Fermi velocity. γ is a quantum correction associated with Berry's curvature of the band structure. In trivial systems, it takes the value $1/2$. In Dirac systems, on the other hand, $\gamma = 0$. This Berry's phase is often used as evidence for the existence of a topological bandstructure, which can in principle be extracted from a plot of the Landau level indices versus inverse magnetic field [99]. However, the influence of Zeeman splitting, the complicating effects of conductivity contributions from other bands and the presence of a Dirac mass can make this extraction unreliable, particularly in three dimensions [100, 101].

Instead, a robust consequence of Eq. 6.1 is a sign-change of the magnetization beyond the quantum limit. In the absence of any other magnetic transitions, this serves as a characteristic signature of the presence of an electron-like Weyl or Dirac Fermi surface. A consequence of $\gamma = 0$ in Eq. 6.1, is that the $n = 0$ Landau level is pinned at zero energy. As the magnetic field is increased, the growing degeneracy of this Landau level pulls down the total energy of the system, leading to an overall paramagnetic response given by $M = -dE/dB$. When the quantum limit is exceeded, the chemical potential asymptotically approaches the zeroth Landau level and the paramagnetic response diminishes, crossing over to the diamagnetic response expected from fully occupied bands [98]. In a single-band system, this crossover from paramagnetic to diamagnetic at the quantum limit leads to a kink and evidences the topological nature of charge carriers in a system.

Moreover, the crossover and associated kink should be a band-specific probe of topology. Since each Fermi surface crosses the quantum limit at a different field determined by its quantum oscillation frequency, the field at which the magnetization kink occurs can isolate which Fermi pocket contains the topological charge carriers. In a multiband system such as $ZrTe_5$, this may be a more sensitive probe than fitting Landau level intercept plots from SdH or dHvA oscillations.

6.2 Magnetic torque

Note, in many cases measuring the magnetization of a sample directly is not feasible. This is true when the magnetization of the sample is very weak, either intrinsically or due to sample size. It is true at high magnetic fields, especially pulsed fields, where the field is noisy and rapidly changing over time. It is also true if continuous rotations of a sample in the magnetic field are required. In these cases measuring a closely related parameter, the magnetic torque, is often an easier route to probe the same physics.

The magnetic torque is proportional not to the magnetization of the sample, but to its magnetic anisotropy. In general, the magnetization, M_i, of a sample is related to the applied magnetic field, H_j, by $M_i = \chi_{ij}H_j$, where χ_{ij} is the magnetic susceptibility, a 3×3

second rank tensor. In an orthorhombic system such as $ZrTe_5$, the off-diagonal elements are constrained to be zero by symmetry and the expression for the magnetization simplifies to $\vec{M} = \chi_a H_a \hat{a} + \chi_b H_b \hat{b} + \chi_c H_c \hat{c}$, where $\hat{a}, \hat{b}, \hat{c}$ are the crystallographic principal axes [102]. As a result, the magnetization will not point in the same direction as the applied magnetic field, unless the field is applied along one of the principal axes or additional crystal symmetries further reduce the susceptibility tensor. This will lead to a torque on the crystal given by $\vec{\tau} = \vec{M} \times \vec{H} = (M_b H_c - M_c H_b)\, \hat{a}$. Simplifying using the susceptibility tensor gives:

$$\tau = \frac{1}{2} \left(\chi_b - \chi_c\right) H^2 \sin(2\theta) \tag{6.2}$$

where θ is the angle of the applied magnetic field measured from the c-axis.

The magnetic torque is proportional to the susceptibility anisotropy and will be large in highly anisotropic systems. Any effects from Landau level quantization that manifest themselves in the magnetic susceptibility, such as dHvA oscillations, will also be apparent in the magnetic torque. Magnetic torque, however, has the advantage that it can be extracted from the straightforward resistance measurement of a microfabricated piezoresistive cantilever.

An example of the cantilever used is shown in Figure 6.1. This is a commercially available piezoresistive AFM tip onto which a sample is attached with vacuum grease. When placed into a magnetic field, the magnetic torque acting on the sample flexes the cantilever causing a change in resistance. A dummy cantilever is also present and can be wired into a Wheatstone bridge circuit to offset any non-torque magnetoresistance of the sample cantilever. In this manner, high precision measurements of a sample's magnetic torque, and therefore its susceptibility anisotropy, can be made in a variety of different environments, including pulsed magnetic fields and rotating sample stages.

6.3 Magnetization measurements

$ZrTe_5$ single crystals were grown by the vapor transport technique as outlined in Section 5.2 using iodine as the transport agent. A precursor powder was prepared by sealing a stoichiometric mixture of zirconium and tellurium in a quartz ampule under vacuum which was heated to 500°C and held for 7 days. The resulting powder was mixed with $5mg/cm^3$ of iodine and sealed in a quartz ampule under vacuum before being loaded into a two-zone furnace. The source and sink ends of the ampule were held at 520°C and 480°C, respectively for 21 days. Needle-like crystals up to 7mm long in the space group $Cmcm$ (No. 63) were obtained from the cold end of the ampule. Crystal structure and orientation was confirmed with x-ray diffraction.

Figure 6.2 illustrates the results of $ZrTe_5$ magnetization, magnetic torque, and transport measurements. The magnetization has a paramagnetic response at low field crossing over to diamagnetism at high field. The magnetic torque, related to the magnetization by Eq. 6.2, shows a very similar cross-over behavior. Both exhibit two kinks: a dominant kink at $\sim$ 1.5T and a smaller, more subtle kink at $\sim$ 2.5T, after which the sign change occurs.

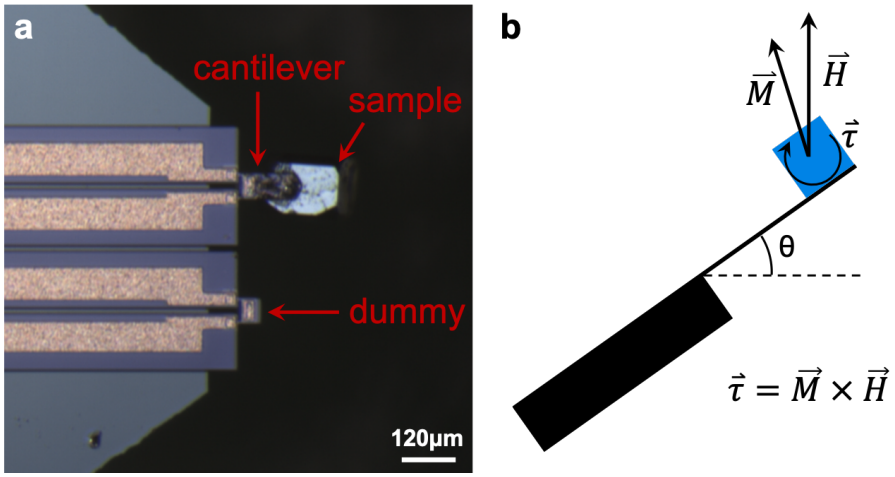

Figure 6.1: **Magnetic torque.** (a) A microscope image of a piezoresistive cantilever with sample and dummy cantilevers. (b) The sample (blue) generates a torque when the magnetization is not aligned with the applied magnetic field. This flexes the cantilever (black) and leads to a measurable change in its resistance.

Finally, the magnetoresistance of $ZrTe_5$ shows pronounced SdH oscillations with field along the crystallographic b-axis. Note that the oscillations are spin-split, so the Landau level position should be identified as the trough between spin-split SdH peaks. From this one can identify that the $n = 1$ Landau level crosses the Fermi energy at 2.6T, in agreement with the frequency extracted from the low-field SdH oscillations and very close to the smaller kink at ~ 2.5T.

From the arguments presented in Section 6.1, this crossover should be associated with a topological Fermi surface entering the quantum limit. Specifically, the kink observed ~ 2.5T matches well with the quantum oscillations which show a Fermi pocket entering its quantum limit at 2.6T. Since $ZrTe_5$ is inversion-symmetric, this pocket would have to be doubly degenerate and therefore Dirac-like in nature. Although both a cross-over from paramagnetism to diamagnetism and a kink can be observed in the magnetization and magnetic torque, the shape of these curves is not as clear-cut as similar measurements in NbAs [98]. Specifically, the dominant change in curvature occurs not at the quantum limit, but at ~ 1.5T. As will be discussed, this may actually be explained by the presence of additional bands that contribute to the magnetization.

In order to distinguish the low-field behavior from other sources of paramagnetism an angle dependence can be used to confirm that the sign change in the magnetization tracks with the quantum limit of the Fermi surface (Figure 6.3). As the angle of the field with respect to the principal axes of the crystal is changed, the cross-sectional area tracked by the frequency of the SdH oscillations shifts accordingly, pushing the quantum limit out to higher field. Figure 6.3b shows SdH oscillations in the magnetoresistance of $ZrTe_5$ at different

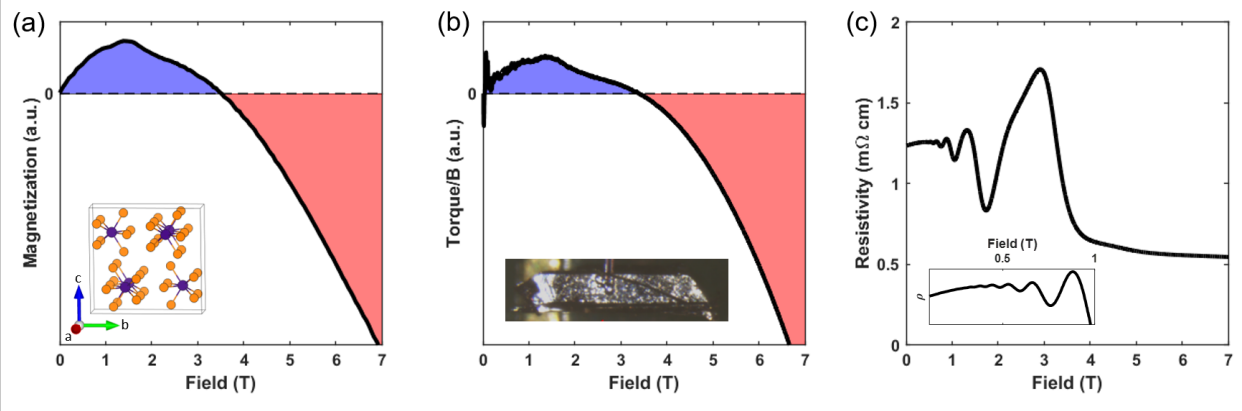

Figure 6.2: **Magnetization, torque, and resistivity.** (a) The magnetization of $ZrTe_5$ with field applied along the crystallographic b-axis shows a clear paramagnetic response at low field and a transition to a diamagnetic response at high field. Inset: The crystal structure of $ZrTe_5$ with Zr atoms in purple and Te atoms in orange. (b) The magnetic torque measured on the same sample as (a) is in close agreement with the magnetization and exhibits the same transition from para- to dia-magnetism. Inset: An image of the $ZrTe_5$ sample mounted on a torque cantilever with the long direction along the a-axis. (c) The magnetoresistance of $ZrTe_5$ shows pronounced SdH oscillations and the onset of the quantum limit in the vicinity of the sign change observed in (a) and (b). Inset: The low-field oscillations show no evidence of beating, implying that only one spin-split frequency is being observed. All measurements were performed at 1.8K. Adapted from Ref. [6].

angles. The frequency and the expected position of the $n = 1$ Landau level can be extracted from the oscillation and is plotted as black dots in Figure 6.3c. The anomaly observed in the torque, plotted as empty red circles, tracks well with the expected position of the $n = 1$ Landau level up until angles where the kink is so broad that it can no longer be well determined. However, one can track the $n = 2$ feature (filled circles in Figure 6.3a) in the torque to much higher fields, and it can be seen to follow the angle dependence of the SdH very closely up to high angles. The correlation between the kink in magnetic torque and loss of paramagnetism with the quantum limit provides strong evidence for the presence of an electron-like Dirac Fermi surface which is responsible for the observed SdH oscillations.

6.4 Evidence for Dirac electrons

There is one peculiar feature of the data which requires additional explanation. Although the $n = 1$ kink observed in the magnetic torque tracks well with the quantum limit, the dominant change in curvature of the torque signal appears at fields lower than the quantum limit (see the filled circles in Figure 6.3a). This would, in general, not be expected from a single Dirac band. Figure 6.4a shows a simulation of the magnetization from a single Dirac

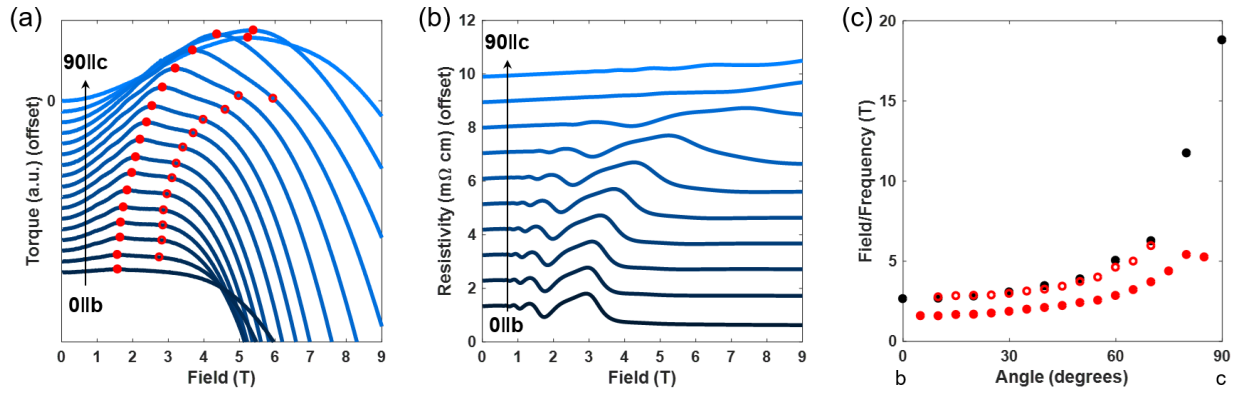

Figure 6.3: **Angle dependence.** (a) Torque measured at different magnetic field orientations in the b-c plane. The paramagnetic response and cross-over field grows with field angle. Two kinks can be extracted from the data. The more prominent low-field kink (filled circles) can be tracked for all angles. The less prominent high-field kink (empty circles) is only observable for intermediate angles. (b) The magnetoresistance measured at different field orientations in the b-c plane shows that the quantum limit grows monotonically with increasing field angle. (c) The kinks in the magnetic torque from (a) (red circles) compared to the SdH oscillation frequency extracted from the magnetoresistance data in (b) (black circles). The quantum limit, which occurs at the SdH frequency, tracks well with the high-field kink over the observable range. All measurements were performed at 1.8K. Adapted from Ref. [6].

conduction band with a linear diamagnetic background. While this broadly reproduces the oscillatory part of the data, it does not capture the overall curvature of the magnetization and the position of the dominant kink. In particular, to reduce the magnitude of the feature arising from the $n = 1$ Landau Level below that of the $n = 2$ with linear diamagnetism only, one has to suppress the weak field paramagnetism entirely. This implies that a non-linear diamagnetic background must be present.

Most conventional sources of magnetism in semiconductors will lead to a linear background in the magnetization, and non-linear contributions from correlated spins seem unlikely in a system with filled shells like $ZrTe_5$. A more natural possibility is the presence of a second Dirac pocket. This pocket – which may be itself slightly gapped – would enter its quantum limit at weak fields and enhance the low field paramagnetic signal. As shown in Figure 6.4b, a simulation of this system better captures the key features of the data. Note that if another Dirac pocket exists, no direct signature in the quantum oscillatory signal is observed. This may be because it enters the quantum limit at very low fields and therefore oscillations are not resolved. Nevertheless, the existence of such a pocket is consistent with DFT calculations of the band structure, and may have already been observed by ARPES experiments [93, 103].

The magnetization calculations shown in Figure 6.4 were performed by considering the effective Hamiltonian $H_0 = \hbar\left(v_x k_x \tau_x \sigma_z + v_y k_y \tau_y + v_z k_z \tau_x \sigma_x\right) + m\tau_z$, where m is a possible Dirac mass and σ and τ denote Pauli matrices for spin and Chern number, as given in [83, 104]. A magnetic field applied along the z direction (crystallographic b-axis) leads to a Zeeman term of the form $H_z = -\mu_B g \sigma_z B/2$. The band velocities, to first order, can be approximated as isotropic with $\hbar v_{x,y,z} = \hbar v = 3.0$ eVÅ, an averaged value of those reported in Ref. [103]. The carrier density and g-factor, $g = 15$, are fixed so the simulation matches the position of the spin-split $n = 1$ peak in Figure 6.2c. Solving for the energy eigenvalues of this Hamiltonian gives $\epsilon_{n,k_z,s} = \pm[v^2\hbar^2 k_z^2 + \left(\sqrt{2v^2 e\hbar B n + m^2} + s\mu_B B g/2\right)^2]^{1/2}$, where n is the Landau level index, $s = \pm 1$ labels the Zeeman split bands and the overall $\pm$ sign denotes the conductance and valance bands.

Assuming the Fermi energy to be in the conduction band, as is expected for the n-type carriers observed in $ZrTe_5$ the ground state energy of the system is given by $E(B) = (eB/2\pi\hbar)\Sigma_{n,k_z,s}\epsilon_{n,k_z,s} n_F(\epsilon_{n,k_z,s} - \mu)$, where n_F is the Fermi distribution restricting the sum to occupied states, and $eB/2\pi\hbar$ is the Landau level degeneracy. The chemical potential μ is calculated by fixing the carrier density $\rho = (eB/2\pi\hbar)\Sigma_{n,k} n_F(\epsilon_{n,k} - \mu)$ to the experimentally determined value. The magnetization is then given by $M(B) = -dE/dB$. The effects of the valence band can be included by subtracting a contribution linear in B [98]. For the parameters considered, the presence of a small zero-field mass does not noticeably alter the simulation and m is set to 0. A Gaussian convolution is applied to the magnetization to account for disorder and thermal broadening of the Landau levels.

The basic result of this calculation is shown in Figure 6.4a. As can be seen, the dominant kink occurs at the quantum limit, in contrast to what is observed in the magnetization and magnetic torque measurements. In Figure 6.4b, an additional Dirac band with $g' = 15$ and $\hbar v'_{x,y,z} = 5.0$ eVÅ is added, which reaches its quantum limit at $\sim$ 1T. The resulting calculated magnetization much more closely resembles the measured data. The low-field paramagnetism is enhanced, resulting in the dominant change in curvature occurring at a lower field value than the quantum limit. There is quite a range of parameters for this second Dirac band that can reproduce the observed low field paramagnetic boost, evidencing the generality of the model.

DFT calculations find several features close to the Fermi level that are consistent with the assumptions made when calculating the magnetization. As shown in Figure 6.5, without including spin-orbit coupling there are two Dirac crossings close to the Γ and S points. With the inclusion of spin-orbit interaction, the Dirac crossings become gapped and a new feature with a Dirac-like dispersion appears at Γ, in addition to several other bands close to the Fermi level in the Z to T direction. Hall effect data shows electron-like carriers at low temperature, implying some of these additional bands must be populated and Dirac-like or massive Dirac-like features should be present [95]. Note that these features are extremely sensitive to cell volume and strain, which may explain the conflicting experimental reports on the electronic properties and topological signatures in $ZrTe_5$ [94, 83, 64, 85, 86, 87, 88, 89, 90, 91, 92, 93].

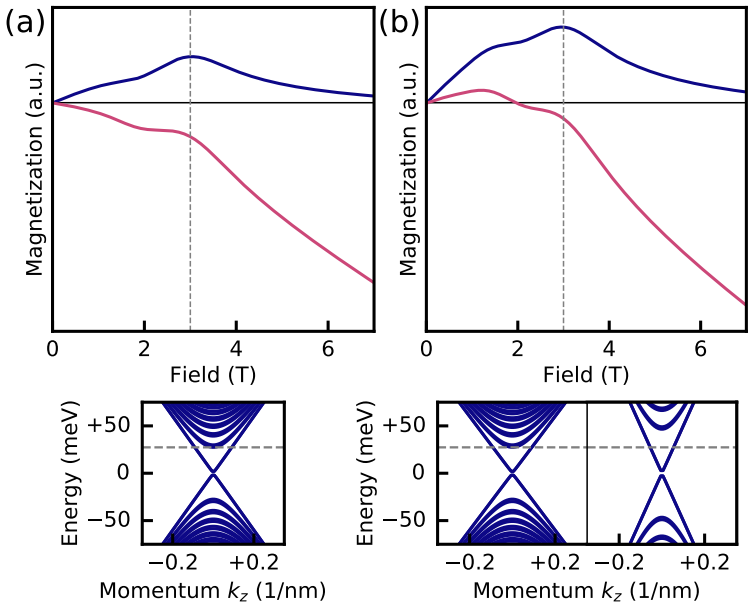

Figure 6.4: **Bandstructure calculations.** (a) Upper: Simulated magnetization of a single Dirac band at constant density, with (red) and without (blue) a linear diamagnetic background. The vertical dashed line at 3T indicates where the Dirac band enters its quantum limit. Lower: Dirac band-structure at magnetic field 3T with chemical potential μ indicated by the grey dashed line. (b) Simulated magnetization for two Dirac bands with (red) and without (blue) a linear diamagnetic background. The response from the high velocity Dirac pocket enhances the paramagnetic response at low field; with background diamagnetism, the $n = 2$ peak may become dominant. Adapted from Ref. [6].

The temperature dependence of the magnetic signal is shown in Figure 6.6. Strikingly, the low-field paramagnetic response is rapidly suppressed by increasing temperature and completely disappears by 5K. This suppression strongly suggests that the balance of Dirac and non-Dirac contributions to the total magnetization is highly dependent on thermal processes. By 10K the magnetization is dominated by the diamagnetic response, but its non-linearity suggests there is still a competing contribution from the Dirac pocket. At temperatures above 30K, which coincides with the peak observed in transport, the magnetization approaches the temperature-independent diamagnetic response typical of ordinary metals. In general, such a sign reversal would not be expected in a thermodynamic quantity over such a short temperature range without a phase transition. This surprising result indicates that the Dirac-like signatures of $ZrTe_5$ are very sensitive, indicating a proximity to a possible topological phase transition (TPT), in which the topological nature of the charge carriers changes.

The disappearance of the paramagnetic response coincides with a peak in the resistivity occurring at 35K (see Figure 6.6b). This peak, which has been observed to range from 10K

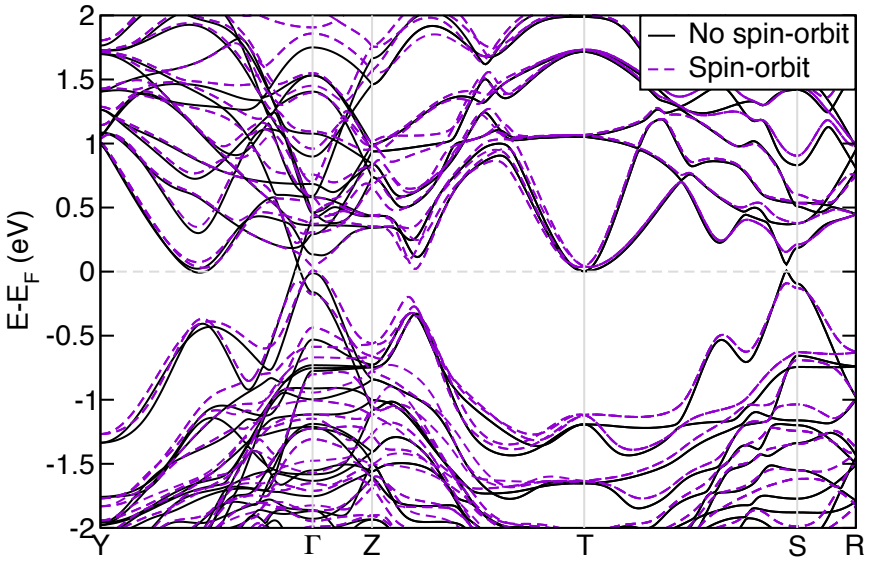

Figure 6.5: **DFT calculations.** Calculated electronic band structure for $ZrTe_5$ with (dashed line) and without (solid line) spin-orbit coupling. Lattice parameters were fixed to experimental values. The Fermi level is set to 0 eV and marked by the dashed line. Adapted from Ref. [6].

to 150K in other samples, has been attributed to a Lifshitz transition [95]. However, the fact that the peaks/troughs of the quantum oscillations in Figure 6.6a do not appear to shift as a function of temperature implies that the chemical potential is not varying with temperature or is varying slowly. Therefore, while a Lifshitz transition cannot be ruled out, the behavior of the magnetization and the resistivity hump is more consistent with a TPT associated with the opening of a gap in a Dirac cone [94]. Figure 6.6c shows the temperature dependence of the zero-crossing of the magnetization, which can be used to parameterize the critical response of the system as it crosses the TPT.

Two key features provide a clue as to the mechanism: the frequency of the quantum oscillations remain constant across the TPT, and the high field diamagnetism is similar above and below the TPT. This suggests that the dominant source of the diamagnetism is the same (namely trivial bands) and that only the Dirac band is changing. In the scenario where there are two Dirac bands, it is possible that the smaller of the two undergoes the TPT. This may explain its dominant paramagnetic signal at low temperatures (since $M \sim v_F$), as well as the preservation of the Fermi surface size of the large Dirac band, since a TPT of the smaller pocket would only weakly affect the filling of the large Dirac band. Another scenario is that one or both bands become massive above the TPT, which would strongly suppress the paramagnetic signal but without necessarily affecting the SdH frequency.

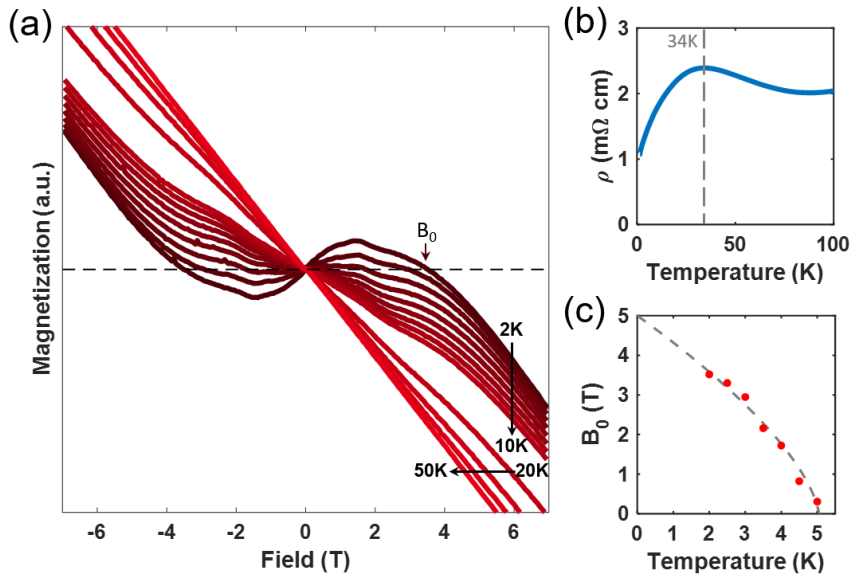

Figure 6.6: **Temperature dependence.** (a) Temperature dependence of the magnetization with magnetic field oriented along the crystallographic b-axis. The low-field paramagnetic response is rapidly suppressed with increasing temperature, becoming completely diamagnetic by 5K. Above 30K, the magnetization approaches the constant, temperature-independent diamagnetic response typically found in ordinary metals. (b) The resistivity shows a peak around 30K, which has been attributed to a Lifshitz transition in $ZrTe_5$ and matches the temperature scale at which the paramagnetism disappears. (c) The field, B_0, at which the magnetization changes sign evolves in a manner suggestive of an order parameter. The dashed line is a guide with functional form $B_0 \propto (1 - T/T_c)^{2/3}$. Adapted from Ref. [6].

6.5 Conclusion

Although the band structure of $ZrTe_5$ is complex and unanswered questions remain, the measurements presented show a clear thermodynamic signature of Dirac electrons. By combining magnetic torque, magnetization and magneto-transport data the disappearance of this signature can be correlated with a possible TPT coincident with a transport anomaly occurring at low temperatures. This is broadly consistent with photoemission and pressure-dependent transport studies of these compounds [95, 96, 97]. Magnetization measurements provide an indirect measure of the topological nature of $ZrTe_5$, exhibiting a bulk, magnetic signature of the transition. $ZrTe_5$ thus provides a rare experimental platform in which the fundamental statistical mechanics of topological systems and their transitions can be studied directly. Understanding topological phase transitions may allow for topological invariants to be used as a robust platform for information storage and computation.

Chapter 7

Antiferromagnetic Memory in Intercalated Transition Metal Dichalcogenides

7.1 Motivation and previous results

Although the FIB has proven to be an extremely useful tool in the exploration of topological semimetals, it can also be used to make devices from other quantum materials that are not readily exfoliated. In this chapter, FIB fabrication techniques are used to show electronically accessible magnetic memory storage in antiferromagnetic (AFM) intercalated transition metal dichalcogenides (TMDs). AFM memory storage has long been sought-after due to the improvements it promises over widely-used ferromagnetic (FM) memory heterostructures. Like FMs, AFMs are a non-volatile method of memory storage. Unlike FMs, AFMs produce no external fields, making memory stored in this manner invisible to external probes and reducing crosstalk between individual devices. AFMs possess ultrafast spin dynamics. They have been demonstrated to switch at speeds up to several THz, compared to the GHz limit of FM memory devices [105, 106]. Moreover, AFMs couple weakly to magnetic fields, making them robust against magnetic perturbations. This insensitivity to field, however, makes manipulating and detecting AFMs difficult, limiting their use primarily to passive layers in FM heterostructure devices [107, 108]. As a result, electronically accessible AFM memory remains a challenge.

One option for manipulating AFM systems for memory storage would be through the use of a spin transfer torque. The spin transfer torque describes the torque applied on localized moments by the spins of the conduction electrons and, in its most general form, is given by

$$\tau = \underbrace{\vec{M}^{A/B} \times \vec{p}}_{field-like} + \underbrace{\vec{M}^{A/B} \times (\vec{M}^{A/B} \times \vec{p})}_{antidamping-like} \tag{7.1}$$

where $\vec{M}^{A/B}$ is the local magnetic moment on the A/B^{th} sublattice and $\vec{p}$ is the net spin

polarization of the injected charge current [107, 109, 110]. The first term in the spin transfer torque is referred to as "field-like" and the second as "antidamping-like". Generally, the field-like term will lead the local moment to precess around the direction of spin polarization, in much the same way that a moment would precess around an applied magnetic field. The antidamping term, however, will point in the direction of the spin polarization, $\vec{p}$, and will tend to align the two. As a result, the direction of the antidamping torque will depend on the spin polarization of the conduction electrons and can be used to change the magnetization of the sample. Note, a Gilbert damping term will also be present. Overcoming the Gilbert damping leads to a minimum current threshold required to reorient magnetic order.

In FM systems, the effect of the antidamping torque is straightforward. Given a large enough current, it will align the local magnetic moments with the spin polarization of the applied current. This is the basic principle of operation behind the magnetic tunnel junction. A fixed FM layer acts as a spin valve, which polarizes the conduction electrons. These polarized electrons then flow to a second, free FM layer, whose magnetization will realign due to the antidamping torque. Since the direction of the electron polarization depends on the direction of current flow, this creates a reversible magnetic switch. Combined with the giant magnetoresistance effect, this forms the basis of commercial magnetoresistive random access memory (MRAM) storage technologies [111, 112, 113].

In AFMs, the situation is a little more complicated. Because of the large exchange coupling energy between neighboring spins, they cannot be treated individually and the system must be treated as a whole. The antidamping torque will act in the same direction on the moments in both sublattices. Since the sublattices are aligned antiparallel, this would, in general cause those moments to rotate in opposite directions. The AFM exchange energy, however, enforces that these moments remain largely antiparallel, up to a small canting. This results in a new equilibrium where the sublattice moments are antiparallel and orthogonal to the direction of the conduction spin polarization. In this configuration, the Néel vector is orthogonal to the conduction spin polarization with a small parallel FM component associated with the canting of the moments. Once the current is no longer present, this FM moment will relax. This mechanism is conceptually similar to a spin-flop transition in an AFM due to an applied magnetic field and is discussed in detail in [114].

Figure 7.1 compares the effect of a spin transfer torque in a FM and an AFM. In a FM, the antidamping torque causes a reorientation of the local magnetic moments to lie parallel to the conduction spin polarization. Typically, this leads to a 180° reversal of the moment, due to the fixed nature of the spin valves [115]. In AFMs, however, the same spin polarization will lead to a 90° rotation of the moments and the associated Néel vector [114].

The magnitudes and directions of the spin transfer torque terms is determined by the spin polarization of the injected charge current, $\vec{p}$. In a conventional heterostructure device, a nonzero $\vec{p}$ is achieved by injecting charge carriers through a fixed FM spin polarizing layer, as is the case in magnetic tunnel junctions [114]. In the absence of such a layer, the value of $\vec{p}$ is determined instead by the symmetries of the crystal lattice. In an inversion symmetric lattice, the net spin polarization over the entire Brillouin zone must be zero, although it may be locally non-zero [116]. In the absence of inversion symmetry, however, the spin

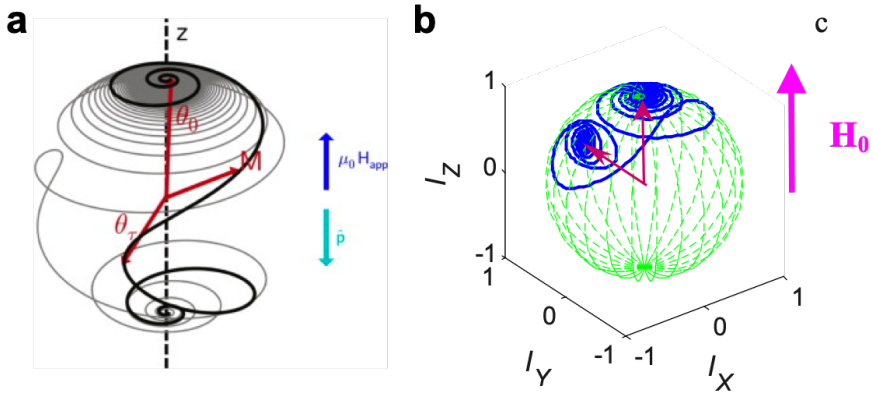

Figure 7.1: **Spin transfer torque switching in FMs and AFMs.** (a) The antidamping torque in a FM rotates the local moments by 180° resulting in a reversal of the magnetization. Adapted from Ref. [115]. (b) In AFMs, the antidamping term results in a 90° rotation of the moments and associated Néel vector. Adapted from Ref. [114].

polarization may be globally non-zero as a result of the inverse spin galvanic effect (ISGE) or Edelstein effect. This is a result of Rashba spin-orbit coupling, which couples a charge carrier's spin to its crystal momentum. An applied electric field will cause the Fermi surface to gain a net momentum, and the Rashba spin-orbit coupling causes a corresponding gain in net spin polarization. In a multiband system, asymmetric interband scattering can enhance this effect [117, 118, 119]. (Note, in an inversion symmetric system the Fermi surface is doubly degenerate and therefore any change in spin population of one subband is offset by an opposite population shift on the other subband.) The ISGE-induced spin polarization is given by $\vec{p} = \hat{z} \times \vec{J}$, where $\hat{z}$ is the unit vector along the direction of the relevant broken mirror symmetry and $\vec{J}$ is the injected charge current [116].

Two AFM compounds, CuMnAs and Mn_2Au, were recently predicted and subsequently measured to possess electronically accessible switching dynamics in single crystal form [116, 120, 121]. A third AFM compound, NiO, was found to be switchable when coupled to spin-polarizing platinum contacts in a heterostructure [122, 123]. It both cases, it was shown that DC electric current pulses could be used to rotate the direction of the AFM order and this rotation could be detected as a change in the device resistance. In this manner, fabricated devices could be used as memory bits with electronic write-in and read-out. Because both CuMnAs and Mn_2Au are inversion-symmetric, their switching behavior has been attributed to the field-like term of the spin transfer torque, which differs from the antidamping-driven switching mechanism described above. Although the charge carrier polarization, $\vec{p}$, must be globally zero, it may be locally non-zero and was predicted to be non-zero with opposite polarity on the two magnetic sublattice sites [116]. As a result, the effective field associated with the field-like term of the spin transfer torque, $\vec{B}_{eff}^{FL} \sim \vec{p}$, will be staggered with the AFM sublattice periodicity. From a symmetry standpoint, it has the same symmetry as the AFM

order, and therefore the two would be expected to couple strongly, allowing a relatively weak electric field to rotate the AFM order. The corresponding field associated with the antidamping term, on the other hand, will have the same value over both sublattice sites, and therefore would not be expected to couple to the AFM order any more strongly than a constant external magnetic field. Although both materials were shown to operate at room temperature, the current densities required for their switching was in excess of $10^7 \mathrm{A/cm}^2$. Combined with the fact that tens of pulses are required for the resistance to saturate to the "low" or "high" value, these compounds are far from ideal for device applications.

The NiO/Pt heterostructure devices, on the other hand, use a different physical mechanism to switch the AFM order [122, 123]. In that case, a strong spin Hall effect in the platinum layer gives a nonzero spin polarization, $\vec{p}$, at the NiO interface. The resulting spin transfer torque rotates the AFM moments in the NiO, and the result can be measured as an anisotropic magnetoresistance-driven change in the device resistance. Because the induced spin polarization is constant across the Brillouin zone, the switching is attributed to the antidamping-like term of Eq. 7.1. Switching in these heterostructures, however, still requires current densities in excess of $10^7 \mathrm{A/cm}^2$, making it difficult to implement in commercial applications. Similarly to CuMnAs and Mn_2Au, multiple current pulses are required to approach saturation. Although switching in these heterostructures has been attributed to the antidamping-like term of the spin transfer torque, it should be noted that switching in a single crystal material driven by the same term has not been observed.

The inadequacy of existing AFM materials for device applications points to a need for new candidates. The existing materials all required high current densities to switch and multiple pulses to approach saturation. Intercalated TMDs have a rich landscape of magnetic orders and may provide a platform for electronically addressable AFM memory devices.

7.2 Growth and magnetic properties of $Fe_{1/3}NbS_2$

This chapter focuses on the inversion symmetry-breaking compound $Fe_{1/3}NbS_2$. $Fe_{1/3}NbS_2$ consists of iron atoms intercalated in a periodic lattice between layers of the 2H phase of the TMD NbS_2. The unit cell is in the hexagonal space group $P6_322$ (No. 182), which breaks inversion symmetry due to the stacking of the iron atoms. The iron atoms are octahedrally coordinated by sulfur and take a 2+ oxidation state with 6 electrons on the d-shell. Because the crystal field splitting is weak compared to the exchange interaction, the d-electrons take the high spin state. The crystal field splitting, however, is larger than the spin-orbit interaction and quenches the majority of the orbital angular momentum [124]. As a result, the iron atoms are observed to have an effective moment of $\mu \sim 5\mu_B$/Fe (corresponding to $J_{eff} \sim 2$) [125]. The electronic structure is metallic with hole-like carriers from the partially-filled niobium d-band.

Crystals were grown using the vapor transport method described in Section 5.2 with iodine as the transport agent. A polycrystalline precursor powder was prepared from stoichiometric amounts of iron, niobium, and sulfur sealed in a quartz ampule. The ampule was

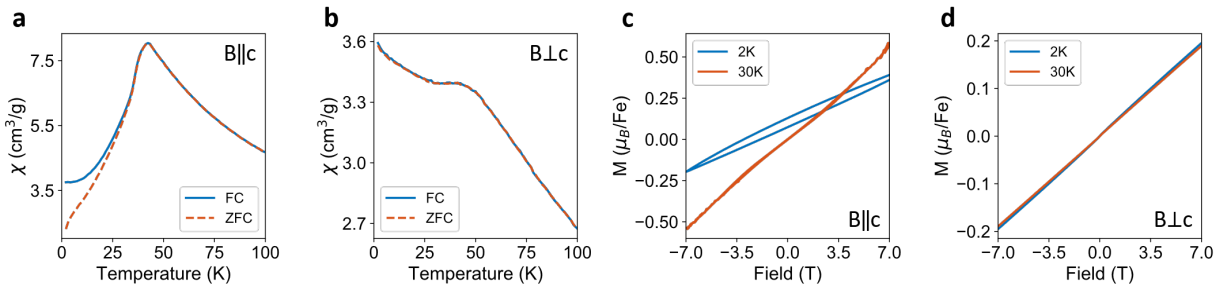

Figure 7.2: **Magnetization measurements.** (a,b) C-axis and in-plane magnetization measurements show a peak at the AFM transition temperature of 42K in both 0.1T field cooled (FC) and zero field cooled (ZFC) measurements. The FC and ZFC curves deviate below approximately 25K. (c,d) C-axis and in-plane magnetization measurements at 2K and 30K. Hysteresis is present with an out-of-plane field at 2K. This hysteresis vanishes by 30K and is not present for an in-plane field at any temperature. Adapted from Ref. [7].

heated to 400°C for 12 hours followed by 900°C for 48 hours. The resulting powder was then mixed with 2.2 mg/cm^3 of iodine and loaded into a horizontal two-zone furnace. The vapor transport reaction is

$$6Fe_{1/3}NbS_2(s) + 14I_2(g) \rightleftharpoons Fe_2I_4(g) + 6NbI_4(g) + 6S_2(g) \tag{7.2}$$

The source end was held at 950°C and the sink end at 800°C for a period of 7 days. On the source end of the tube, the reaction equilibrium is shifted towards the products, which diffuse to the sink end. The lower temperature at the sink shifts the equilibrium back towards the reactants, causing $Fe_{1/3}NbS_2$ to be deposited in single crystal form. Note, that although Eq. 7.2 represents the dominant reaction taking place, minority species of FeI_2 and FeI_3 will be present on the right hand side, complicating the reaction and associated calculations [61]. High quality crystals in excess of 5mm were obtained. These crystals were fabricated into devices using the FIB fabrication techniques outlined in Chapter 3. Because of their platelet morphology, lamella cutting was not required. Instead, thin (<10 μm) crystals could be directly mounted into epoxy for device fabrication.

The iron atoms in $Fe_{1/3}NbS_2$ are arranged in a triangular lattice, leading to geometric frustration. Nevertheless, it exhibits AFM ordering at low temperature with a transition from a paramagnetic state at 42K [126, 127, 128, 129, 124]. Most likely, this is a coupled with a structural relaxation to relieve the geometric frustration, consistent with heat capacity and magnetization measurements [125]. Recent single-crystal neutron diffraction measurements have shown an AFM stripe ordering of the iron moments, which are mostly colinear with the c-axis, but have a 10° - 15° canting into the ab-plane [130]. This AFM order is thought to be primarily driven by an RKKY interaction mediated by the conduction electrons associated with the niobium d-band [124]. A superexchange interaction mediated by the calcogen atoms may play a smaller, secondary role [128].

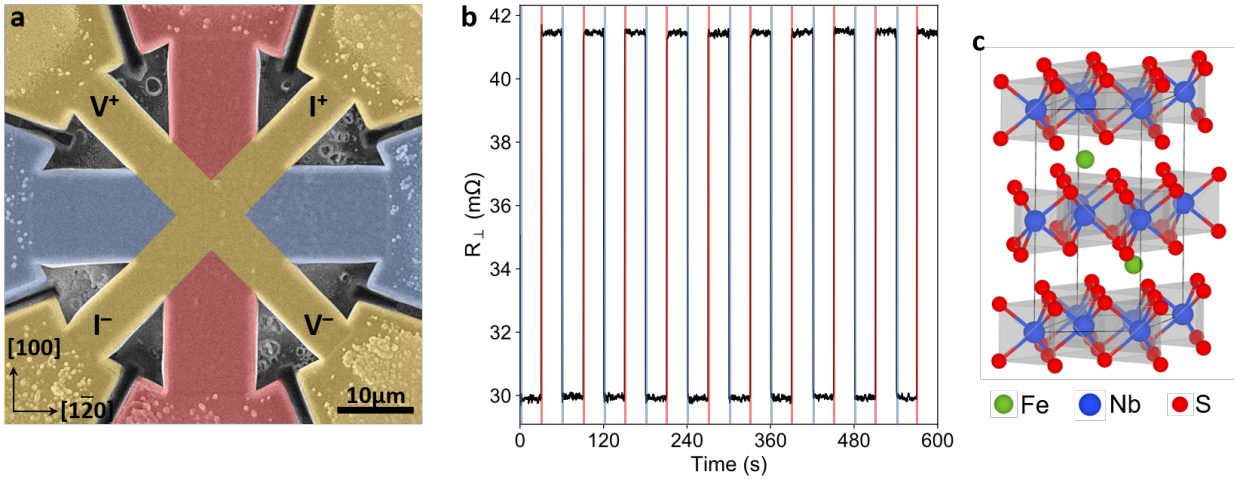

Figure 7.3: **Basic switching results.** (a) A false-color SEM image of a $Fe_{1/3}NbS_2$ switching device. The transverse resistivity ($R_\perp$) is measured using the yellow contacts. A 100 μA (5.4×10^2 A/cm^2) AC probe current is applied along one yellow bar, while the voltage drop is measured along the orthogonal bar using standard lock-in techniques. Simultaneously, DC current pulses can be applied along the red and blue contacts in the [100] and [1$\bar{2}$0] directions. (b) When orthogonal current pulses are applied, the transverse resistivity switches between two states. Applying 5.4×10^4 A/cm^2 for 10ms along the blue contacts switches the device into a low transverse resistivity state. Applying the same pulse along the red contacts switches the device into a high state. The time between pulses is 30 seconds and the switching has been repeated 10 times to show the robustness of this behavior. The measurement was performed at 2K. (c) The crystal structure of $Fe_{1/3}NbS_2$ is that of 2H-NbS_2 with iron atoms intercalated between layers. At this stoichiometry, the iron intercalants form an ordered lattice with space group $P6_322$ (no. 182). Adapted from Ref. [7].

Magnetization measurements show a peak at 42K, with field cooled (FC) and zero field cooled (ZFC) curves overlapping, a strong indication of AFM order. As shown in Figure 7.2, however, there is a slight residual moment between the FC and ZFC curves below approximately 25K. This residual moment has been attributed to a spin glass phase stemming from iron impurities due to deviations from perfect stoichiometry. Thermodynamic measurements show hysteresis in the magnetization, a giant exchange bias, a broadened transition in heat capacity, memory effects, and time relaxation, all pointing to the presence of a spin glass phase. Nuclear magnetic resonance measurements, however, show clear indications of a co-existing AFM order, manifested as two distinct resonance peaks as a function of magnetic field [125].

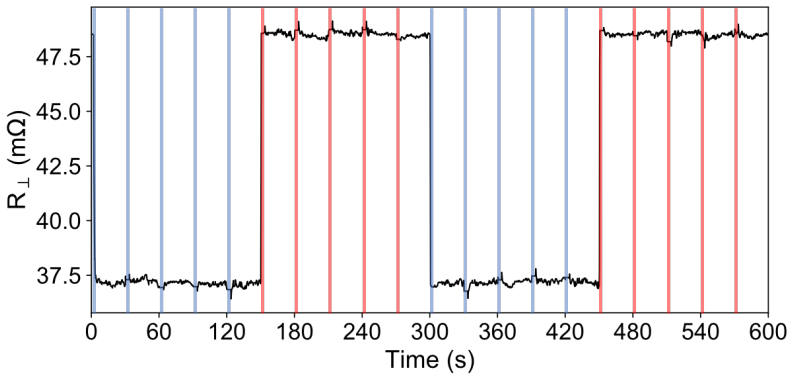

Figure 7.4: **Multiple pulses.** The switching response of the device with the same contact geometry shown in Figure 7.3a. Five pulses are applied in each orthogonal direction (blue and red). After the first pulse switches the resistance state, the four subsequent pulses have no effect, indicating that the response has saturated after the application of the first pulse. Adapted from Ref. [7].

7.3 Electrical switching in microstructured $Fe_{1/3}NbS_2$ devices

Figure 7.3 shows the basic results of this project. When fabricated into an eight-contact device using standard FIB techniques, the AFM order in $Fe_{1/3}NbS_2$ can be switched using electrical current pulses and measured as a change in device resistance. The transverse resistance of the device is measured by driving a 100 µA (5.4×10^2 A/cm^2) alternating current (AC) across one leg of the device and measuring the resulting voltage drop across the orthogonal leg (yellow contacts in Figure 7.3a) using standard low-frequency lock-in measurement techniques. In tandem, direct current (DC) pulses can be applied along two orthogonal directions (red and blue contacts).

The application of a DC pulse along the thick bars switches the sample between two different magnetic states, reflected in the transverse resistivity. A 5.4×10^4 A/cm^2 current density applied for 10ms along the blue bar (A direction) switches the device into a low transverse resistance state. The same pulse applied along the red bar (B direction) switches the device into a high resistance state. This switching is repeatable, reversible, and stable. The device can be switched from one resistance state into the other with subsequent application of pulses along the two orthogonal directions. This process can be run in either direction. Moreover, once in the high or low resistance state the device is stable and the measured transverse resistance does not decay over the 30-second intervals shown in Figure 7.3b.

Applying multiple current pulses in the same direction does not change the resistance value of the high/low state, implying that a single pulse saturates the response, as shown in

Figure 7.4. This is in sharp contrast to the previously discovered switching AFM systems, all of which required tens of pulses to approach their saturation values [120, 121, 122, 123]. Reversing the polarity of the current pulses also does not change the switching behavior. The device switches to the low resistance state for both positive and negative current pulses along the blue bar and to the high resistance state for both negative and positive current pulses along the red bar. This is a direct result of the anisotropic magnetoresistance (AMR) read-out mechanism as will be discussed in further detail.

Figure 7.5 shows the temperature and magnetic field dependence of the switching amplitude. The switching amplitude was extracted by fitting a square wave to the measured device response when applying 10 alternating A/B current pulses. It is suppressed by both temperature and out-of-plane (c-axis) magnetic field. By 40K and 14T, switching is no longer observable. These values are closely related to the suppression of the AFM order. A phase transition to a paramagnetic state is observed at 42K, and a spin-flip transition at 16T. The coincidence of the suppression temperature and field with the magnetic transitions imply that the switching must be driven by the AFM state. The robustness of the effect to large out-of-plane fields is remarkable and a direct consequence of the AFM origin of the switching. Interestingly, in-plane magnetic fields do not appear to have any effect on the switching amplitude.

One interesting aspect of the field dependence is shown in Figure 7.6. Although the ability to switch the AFM order is suppressed by an out-of-plane magnetic field, memory of the ordered state appears to be preserved. Specifically, sweeping the magnetic field after switching the device preserves the change in resistance between the high and low states, although the absolute resistance values change due to hysteresis caused by the spin glass. An A (B) pulse is applied to the device, switching it into the low (high) transverse resistance state after which the magnetic field is swept from 0T to 14T to -14T and back to 0T. The difference between the two resistance curves remains essentially unchanged, implying that although the field changes the magnetization state of the spin glass, it does not change the magnetization state of the AFM, which is determined by the initial A or B current pulse. The magnetic field does not erase the information stored in the AFM state, but instead "freezes" it, preventing it from being altered by subsequent current pulses. As will be discussed, this is strong evidence that the AFM, not the spin glass, is in fact driving the switching behavior.

Rotating the device geometry, as shown in Figure 7.7a, can help elucidate the mechanism of the switching behavior. The AC excitation current and the associated four-point resistance measurements ($R_{\parallel}$ and $R_{\perp}$) were rotated between contacts while keeping the direction of the DC current pulses fixed. 45° (column 1) denotes the configuration shown in Figure 7.3. At this angle, all the switching is observed in the transverse channel ($R_{\perp}$) while almost no signal is observed in the longitudinal resistance ($R_{\parallel}$). Rotating the contacts to 90° (column 2) reverses this. The switching appears parallel to the current while the signal in the transverse channel is suppressed. Rotating the contacts further, to 135° and 180° moves the switching signal back into the perpendicular and longitudinal channels, respectively, however the sign is now reversed. Namely, application of the same pulse sequence results in a reversed ordering of high and low resistance states. Figure 7.7a shows angles 45° to 180°. Angles 225° to 360°

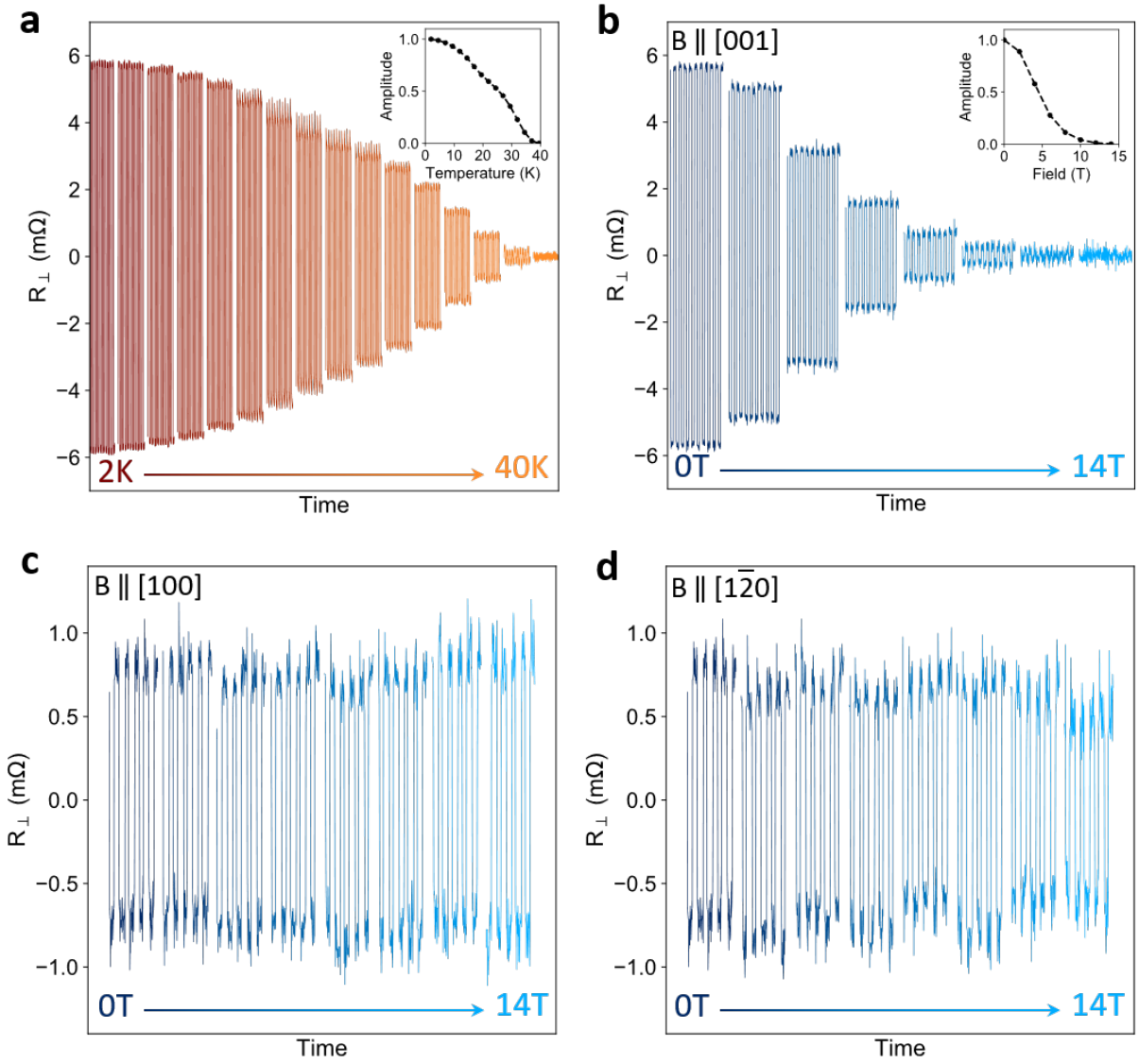

Figure 7.5: **Temperature and field dependence.** (a) The switching behavior is suppressed by temperature. By 40K, the switching amplitude is completely suppressed, as shown in the inset. The temperature-dependent background of $R_\perp$ has been subtracted from all curves to highlight only the switching component. (b) The switching behavior at 2K is suppressed by an out-of-plane magnetic field, although it shows surprising robustness and can be observed at fields as high at 12T. The field-dependent background of $R_\perp$ has been subtracted to highlight only the switching component. The extracted switching amplitude is shown in the inset. (c,d) Application of an in-plane field has little effect on the switching behavior, which can still be observed as high as 14T. Measurements were performed at 2K and for two orthogonal field directions: [100] (c) and [1$\bar{2}$0] (d). Note, these measurements were performed on a different device from the previous two panels. Adapted from Ref. [7].

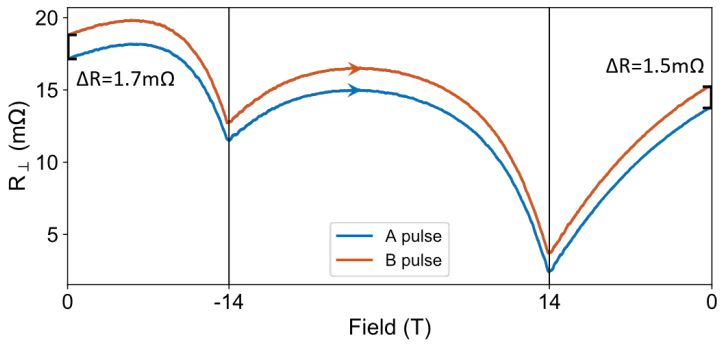

Figure 7.6: **Memory persistence.** Field sweeps performed after applying DC current pulses to a FIB device show the robustness of the switching memory. Applying a DC current pulse along the A (B) bar of the device at 0T switches the device into a low (high) transverse resistance state. A magnetic field along the c-axis is then swept from 0T to +14T to -14T and back to 0T. Although the sample returns to a different absolute resistance value, due to the hysteretic spin glass background, the difference in resistance between the A and B pulses remains unchanged, indicating that the AFM phase remembers which state it was initially switched to and the magnetic field does not erase this information. This measurement was performed at 2K. Adapted from Ref. [7].

(not shown) repeat the behavior, giving an overall 2-fold periodicity to the switching.

The angle dependence of the switching is intimately connected to the anisotropic magnetoresistance (AMR). The AMR was measured by field cooling a bulk crystal in a 9T in-plane field from above the AFM transition to 2K. The magnetic field was then turned off, and $R_{\parallel}$ and $R_{\perp}$ were measured. This process was repeated at several angles, as shown in Figure 7.7b. After background subtraction, $R_{\parallel}$ and $R_{\perp}$ show the characteristic sinusoidal AMR behavior offset by 45° [131]. The amplitude of the AMR signal is completely suppressed by 40K (Figure 7.7b, inset), the same temperature at which the switching behavior disappears and close to the AFM transition.

There are two important things to note in the AMR data. First, the AMR presented in Figure 7.7 is the zero field AMR. This differs from a conventional AMR measurement in which $R_{\parallel}$ and $R_{\perp}$ are measured in the presence of a finite magnetic field. The fact that this quantity is non-zero means that the in-plane field influences the direction of the AFM order, which remains frozen-in even after the field has been removed. As a result, the magnetic field can be used to write information into $Fe_{1/3}NbS_2$, which can then be read out via the AMR after cooling, in a similar manner to the current pulses. Similar field-induced memory effects stemming from a zero field AMR have been observed in the AFM systems FeRh and MnTe [132, 133].

Note, the field dependence of the zero field AMR is evidence for the presence of domains in this system. Figure 7.8 shows the non-saturating behavior of the zero field AMR at 2K with increasing field. This is likely due to the formation of AFM domains whose local Néel order is oriented along the principal axes of the lattice, as required by symmetry. The aggregate Néel vector, however, may point in an arbitrary direction since it averages the contributions from each individual domain. As such, it can point along the applied magnetic field (or current pulse) direction. This pseudo-continuous rotation of the aggregate Néel vector from additional of local, discretely rotatable domains is described in detail in Refs. [133, 134]. As the magnetic field is increased, the domains become increasingly polarized, leading to the increasing AMR response. The quadratic increase at low fields should eventually lead to saturation, however this field threshold appears to be larger than 14T. Saturation appears to be easily reached when applying current pulses, however.

Second, the zero field AMR also has the same angle dependence as the switching amplitude. The AMR is independent of the sign of the magnetic field, as is the switching amplitude to the sign of the current pulse. Where $R_{\parallel}$ or $R_{\perp}$ in the AMR is maximized, the switching amplitude is maximized in the same channel. Where $R_{\parallel}$ or $R_{\perp}$ go through zero, the switching behavior is suppressed. Where $R_{\parallel}$ or $R_{\perp}$ become negative, the switching order inverts. This implies that the application of a current pulse to the device is similar to an in-plane magnetic field: they both write a preferred orientation into the AFM state, which can then be electronically read out via the AMR. In other words, both a current pulse and an applied magnetic field in the same direction act to rotate the principal axes of the resistivity tensor in the same way. In this manner, the device can be used to store information with electrical write-in and read-out.

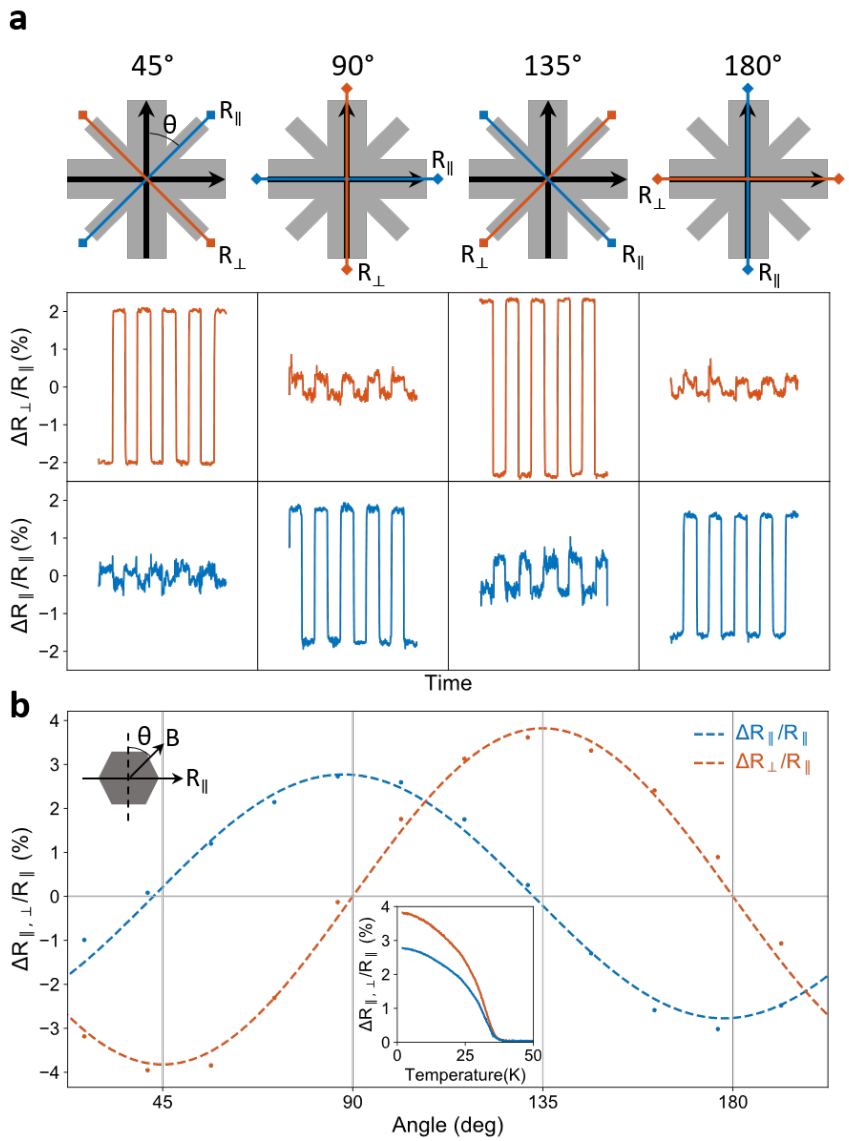

Figure 7.7: **Geometry dependence and AMR.** (a) The switching behavior is dependent on device geometry. As the angle between the AC probe current and the DC write pulses is rotated (top row), the switching signal moves between the transverse (red, middle row) and longitudinal (blue, bottom row) resistance channels, picking up a sign change between 90° and 135°. Black arrows denote the fixed directions of the DC pulses, with the horizontal bar pulsed first followed by the vertical bar, repeated five times. Red denotes the transverse resistivity. Blue denotes the longitudinal resistivity and the direction of the AC probe current. The measurement configuration at 45° is equivalent to that in Figure 7.3. (b) The zero field AMR shows a very similar angle dependence. Every 45° rotation shifts the signal from one resistance channel to the other. Moreover, the sign of the AMR switches in the same angular range as the sign change in the switching. As shown in the inset, the AMR vanishes at approximately 40K, the same temperature at which the switching behavior disappears. A constant offset has been subtracted from both curves. Adapted from Ref. [7].

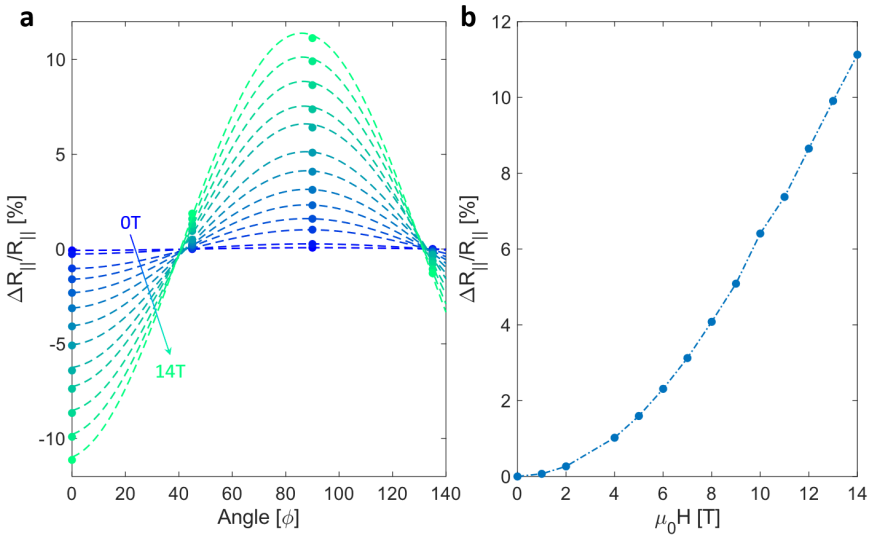

Figure 7.8: **Field dependence of the AMR.** (a) The field dependence of the zero field AMR measured on a bulk crystal and fit to the characteristic sinusoidal dependence. (b) The zero field AMR amplitude grows with field without saturating up to 14T. This may indicate that magnetic domains are present and are being successively polarized with increasing magnetic field. This is in contrast to the electrical current dependence, where saturation appears to be reached after a single pulse. Adapted from Ref. [7].

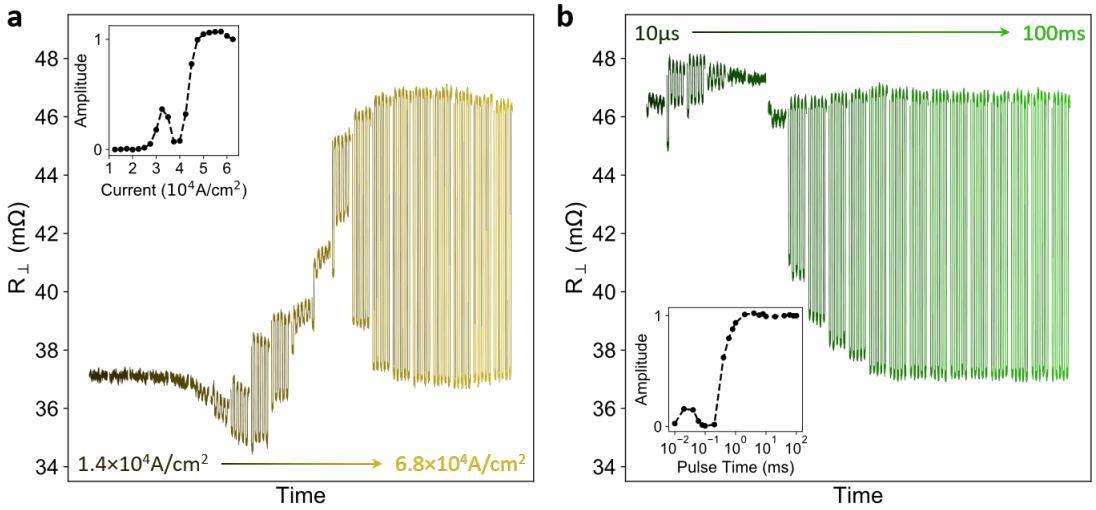

Figure 7.9: **Pulse current density and duration dependence.** (a) The switching amplitude saturates at large current densities but shows non-monotonicity and a local maximum at small currents. Switching can be observed at current densities as low as 2.7×10^4 A/cm^2. The extracted switching amplitude is plotted in the inset. Measurements were performed at 2K in the absence of an external field with a 20ms pulse duration. (b) The pulse duration shows a very similar behavior to the current dependence, with a local maximum followed by saturation of the switching amplitude. Switching is observed as low as 10 µs, the limit of the experimental apparatus. Measurements were performed at 2K in the absence of an external field with a 5.4×10^4 A/cm^2 current density. Adapted from Ref. [7].

Figure 7.9 shows the dependence of the switching behavior on the current density and pulse duration of the DC pulses. At large current densities and durations the switching amplitude saturates, indicating that an in-plane magnetic component has been fully polarized by the DC pulse. At low densities/durations, however, the switching amplitude is non-monotonic, exhibiting a local maximum. Moreover, although the device appears to exhibit switching in this region, the amplitude is smaller than in the saturated region and the high and low resistance states are not perfectly repeatable; the resistance values appear to change between pulse sets. This may be due to domains of an in-plane AFM order that cannot be fully polarized below a critical threshold. Although not fully saturated, switching can be observed at current densities as low as 2.7×10^4 A/cm^2 and pulse durations as short as 10 µs (the limit of the experimental apparatus), both orders of magnitude lower that what has been previously reported for DC pulses in CuMnAs, Mn_2Au, and NiO/Pt heterostructures [120, 121, 122].

Although the data presented thus far has come from a single FIB device, the behavior described has been observed in multiple devices. The switching characteristics of an additional device are summarized in Figure 7.10. The device was fabricated using the same FIB techniques. The current dependence shows a similar non-monotonic behavior, with saturation of the switching response starting around 5.6×10^4 A/cm^2, in close agreement to the value of 5.4×10^4 A/cm^2 observed in the first device. The temperature and out-of-plane field dependencies are also very similar; the switching behavior is suppressed by both, disappearing by 35K and 12T, respectively.

7.4 Spin transfer torques and magnetic order

The switching behavior points to a magnetic order that is significantly more complicated than previously suggested. Previous studies found the moments to be AFM ordered and parallel to the c-axis in a Wurtzite-type geometry [126, 127]. An applied in-plane magnetic field would be expected to couple isotropically to such an order in the absence of any additional symmetry breaking. In contrast, AMR and magnetization measurements indicate that some component of the AFM order lies in the ab-plane. This could be due to canting of the spins or the coexistence of a more complicated magnetic order, like the helical textures, observed in other intercalated TMDs such as $Cr_{1/3}NbS_2$ and predicted by theory for these frustrated system [135, 136]. Recent neutron diffraction measurements indeed suggest that the magnetic moments are canted into the ab-plane by 10° to 15° while remaining antiparallel to each other. This in-plane AFM component is likely the origin of both the zero field AMR and the switching behavior.

In addition to a canting of the AFM order, a coexisting low-temperature spin glass state has been observed. This spin glass likely stems from iron vacancies and is responsible for the residual moment between the field cooled and zero field cooled curves and the magnetization hysteresis in Figure 7.2. In addition, $Fe_{1/3}NbS_2$ shows a giant exchange bias, a broadened transition in heat capacity, memory effects, and time relaxation effects, all supporting the

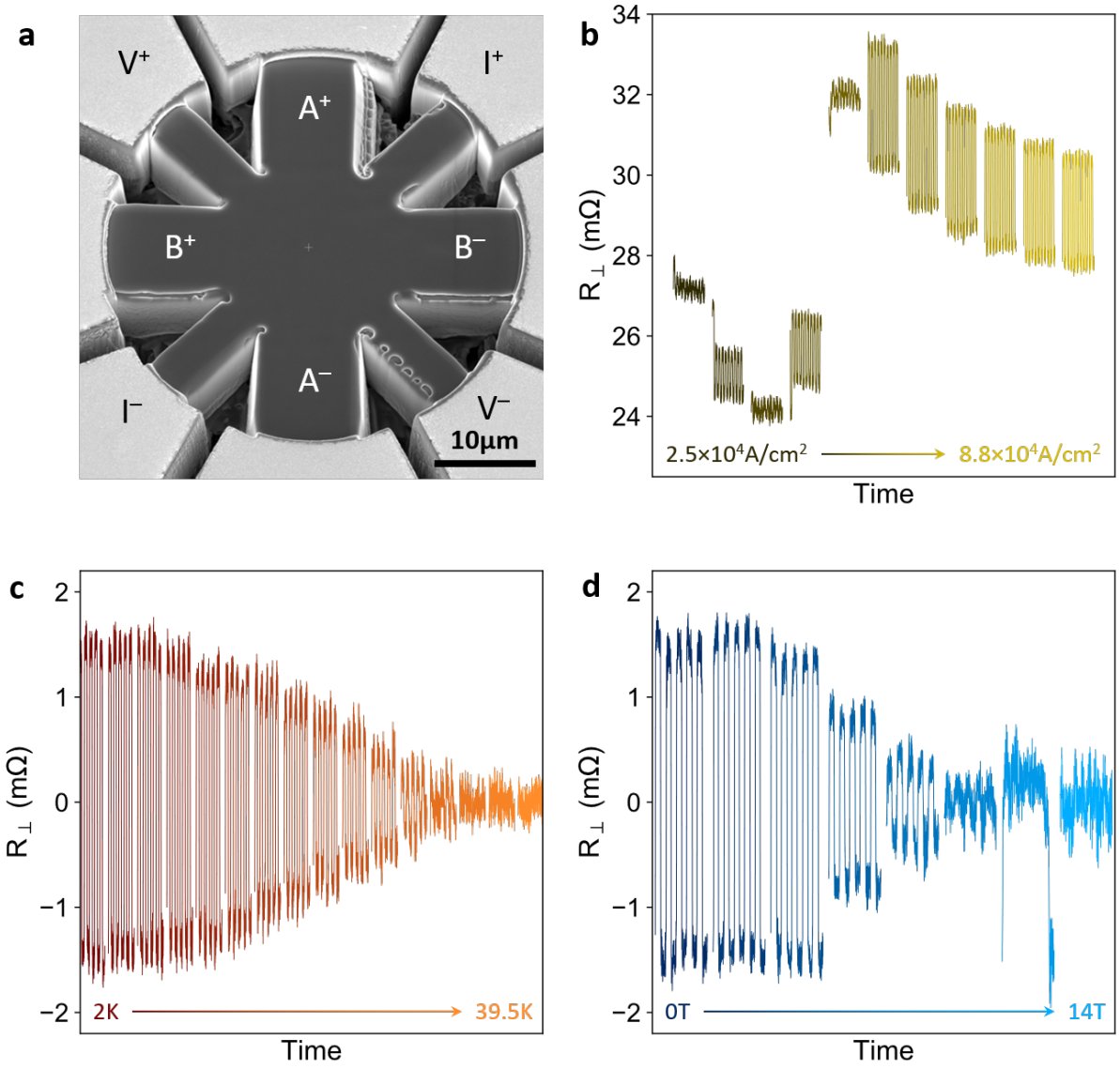

Figure 7.10: **Second switching device.** (a) An SEM image of an additional switching device. The narrow bars are used for resistivity measurements and the wide bars for current pulses. The A bar is pulsed first followed by the B bar. (b) The current dependence at 2K shows the non-monotonic behavior observed in first device. The switching response saturates around 5.6×10^4 A/cm^2. (c) The switching response is suppressed by temperature, disappearing by 35K. (d) The switching is also suppressed by magnetic field, disappearing around 12T. Measurements were performed at 2K. Temperature and field-dependent backgrounds have been subtracted from (c) and (d). Adapted from Ref. [7].

conclusion of a coexisting spin glass phase [125]. Although the interplay between the spin glass state and the AFM order is quite complicated, the spin glass state itself is not believed to be responsible for the switching behavior for several reasons. First, although the magnetization curves in Figure 7.2 show hysteresis at 2K, the hysteresis is suppressed by 30K. The switching behavior, however, persists up to at least 40K, close to the AFM transition temperature of 42K. Moreover, the in-plane magnetization curves do not show hysteresis at any temperature. This implies that the spin glass moments do not cant significantly into the plane, as would be required to produce the previously discussed AMR.

Second, switching the magnetic field after switching the device appears to preserve the change in the resistance between the high and low states, as shown in Figure 7.6. Although the absolute value of the transverse resistance shows hysteretic behavior and does not return to the same resistance value, as would be expected with a spin glass contribution, the difference between the two curves remains essentially unchanged. Although the field changes the magnetization state of the spin glass, it does not change the magnetization state of the AFM order initially established through application of the A or B current pulse.

Finally, the strength of the spin glass phase can be tuned by varying the iron stoichiometry. At certain stoichiometries, all trace of the spin glass phase vanishes but switching can still be observed. See Section 7.5 for a more detailed discussion of the spin glass.

In order to better understand the switching behavior, it is useful to treat it as two separate processes: "write-in" in which information is encoded into the AFM state via the current pulses, and "read-out" in which the AFM state is probed by the resistivity measurement. The read-out process is equivalent to the aforementioned AMR measurements. The anisotropic scattering of conduction electrons from the localized iron moments changes the measured resistance depending on the relative orientation of the AFM order and the AC probe current. This effect typically stems from scattering of conduction electrons into the localized iron d-orbitals and is discussed in more detail in Refs. [131, 137, 138]. In this manner, the resistivity tensor is sensitive to the direction of the in-plane Néel vector. When the in-plane moments are rotated 90° by a current pulse, the measured resistance switches from a maximum to a minimum (or vice versa), reading-out the information encoded into the magnetic state.

In the write-in process, the current pulses reorient the Néel order and hence rotate the principal axes of the AMR-derived resistivity tensor. This is accomplished by the spin transfer torque discussed in Section 7.1. The lack of inversion symmetry in $Fe_{1/3}NbS_2$ generates a net spin polarization in the conduction electrons when a current pulse is applied according to the inverse spin galvanic effect (ISGE). This polarization is given by $\vec{p} = \hat{z} \times \vec{J}$ [117, 118, 119]. In $Fe_{1/3}NbS_2$, this leads the conduction electrons to be spin polarized in the ab-plane, orthogonal to the current pulse. Since AFM moments will be rotated perpendicular to the spin polarization by the spin transfer torque, this causes the preferred orientation of the in-plane component of the Néel vector to be parallel to the current pulse. This agrees with the AMR measurements, showing that current and magnetic field should transform in the same way. Because of Gilbert damping, a minimum current threshold is required to achieve this rotation.

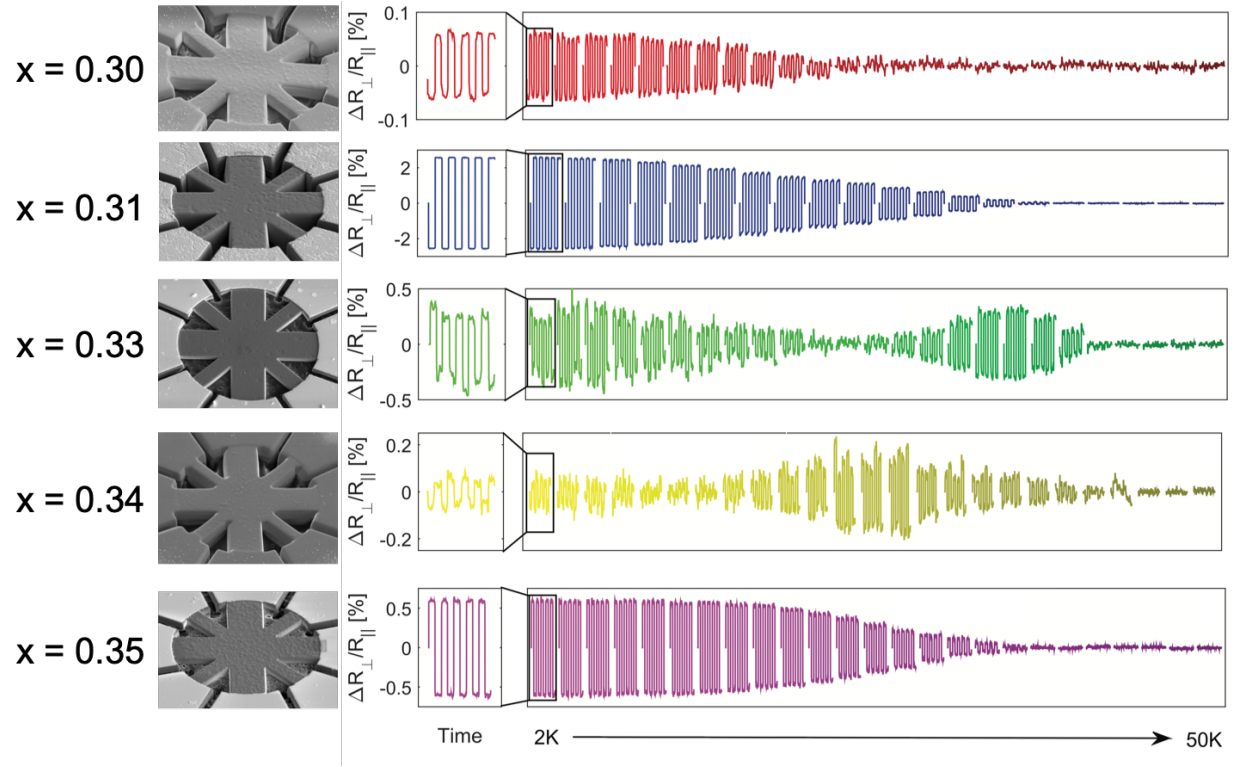

Figure 7.11: **Iron concentration: switching.** Devices of Fe_xNbS_2 were fabricated and measured for five different iron stoichiometries, x. The normalized traverse resistivity is shown at various temperatures. Applying the same A/B pulse sequence to each device results in changes to the high/low switching order depending on iron concentration. Moreover, at intermediate concentrations the switching amplitude is non-monotonic as a function of temperature and shows a sign reversal.

7.5 Iron stoichiometry

Up to this point only a single iron intercalation has been discussed. When measured using energy dispersive x-ray spectroscopy, this iron stoichiometry was found to be 0.31, slightly below the nominal value of 1/3 due to iron vacancies. These iron vacancies are likely responsible for the aforementioned spin glass phase. Varying the iron concentration, therefore, should change the strength of the spin glass phase and, it turns out, dramatically influences the switching behavior.

Crystals of Fe_xNbS_2 were grown by the same vapor transport method described in Section 7.2, where x, the iron concentration, was confirmed using energy dispersive x-ray spectroscopy. Eight-contact devices were then produced using FIB fabrication. The switching behavior as a function of temperature for $x = 0.30, 0.31, 0.33, 0.34, 0.35$ is shown in Figure 7.11.

There are several important features to note in the data. First, the switching behavior at low temperature depends strongly on the iron concentration. Applying an A pulse followed by a B pulse to the $x = 0.31$ device, switches it between a low and high transverse resistance state, as has been discussed for most of this chapter. This is also true of the $x = 0.30$ and $x = 0.34$ intercalations. Applying the same pulse sequence to the $x = 0.33$ and $x = 0.35$ devices, however, results in a reversed ordering of the resistance states. Namely, the A (B) pulse produces a high (low) transverse resistance state.

The second major result of varying the iron concentration is that it changes the temperature dependence. Whereas the $x = 0.31$ device shows a monotonic temperature dependence in which the switching amplitude is suppressed by increasing temperature, the $x = 0.33$ and $x = 0.34$ both show a much more complicated behavior. In these devices the switching amplitude actually changes sign as a function of temperature, reversing the order of the high and low resistance states.

Changing the iron concentration also affects the evolution of the zero field AMR, as shown in Figure 7.12. The zero field AMR measured on bulk crystals shows a sign change as a function of temperature in the intermediate intercalations, $x = 0.33$ and $x = 0.34$. There the low-temperature AMR is opposite to the rest of the series. In contrast to the switching behavior, where the intercalant end-points showed opposite responses, the AMR shows the same response at both end points.

There are two aspects of this behavior that must be explained: the sign change of the switching, and the sign change of the correlation between the switching and the AMR. These two effects cannot be fully explained with the straightforward model presented of a spin transfer torque acting exclusively on an AFM state, even if that AFM state changes with iron intercalation. Instead, the solution likely requires that the spin glass phase play a role in mediating the spin transfer torque interaction in addition to an AFM state that is intercalation-dependent due to the inherent frustration of the system.

Small variations in iron concentration can lead to large changes in spin glass dynamics. Specifically, above and below the $x = 0.33$ iron stoichiometry, the spin glass will switch from being generated by iron vacancies to being generated by excess iron moments. Since spin glasses can be driven by ferromagnetic or antiferromagnetic correlations, it is possible that the spin glass phases on opposite ends of the concentration series have opposite spin-spin correlations. As per Section 7.1, this will lead to a qualitative change in the response of the spin glasses to the spin transfer torque.

At the same time, moving through the $x = 0.33$ fully packed iron stoichiometry causes a change in the AFM phase. Frustrated magnetic systems such as $Fe_{1/3}NbS_2$ lie on the cusp of multiple magnetic ground states. Which one is spontaneously selected is determined by small variations in lattice parameters, intercalations, disorder, etc. Changing the intercalant concentration, therefore, may lead to the selection of a new AFM ground state with similar interaction strengths to the first, but with a different microscopic spin texture. This may result in a similar low-temperature AMR behavior in the presence of an external magnetic field, but a different interaction with the spin glass state, and therefore a change in the response to a current pulse.

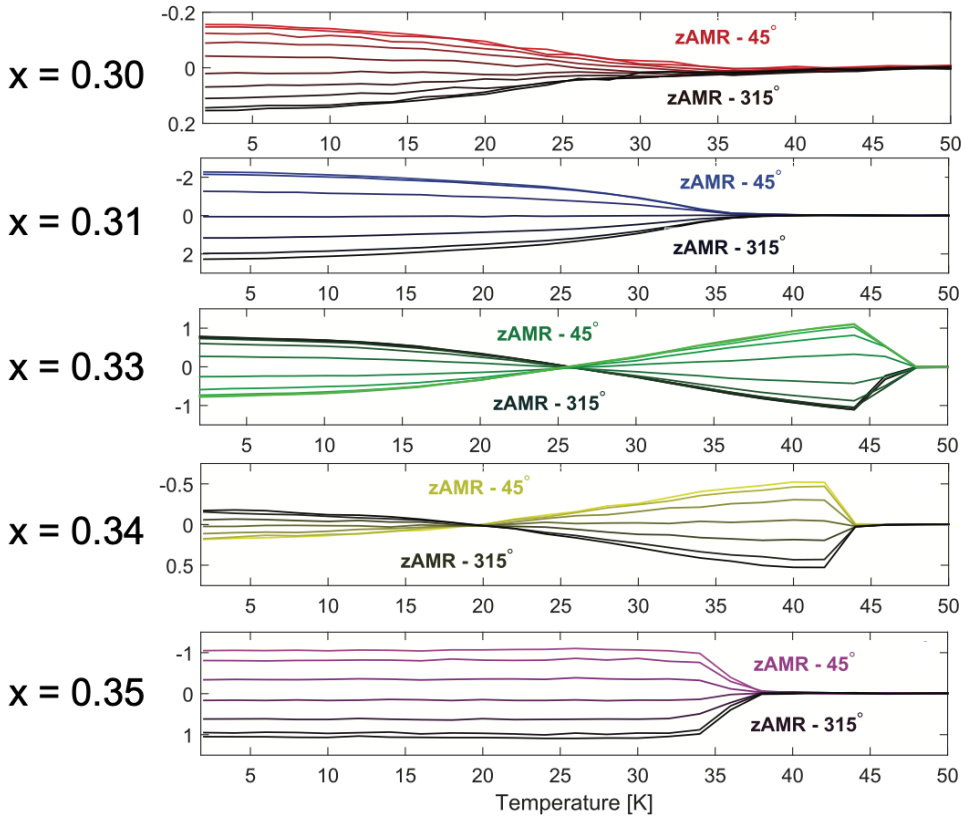

Figure 7.12: **Iron concentration: AMR.** The zero field AMR measured on crystals of various iron stoichiometries, x. The AMR shows a sign change as a function of temperature at low temperatures for the intermediate intercalants ($x = 0.33$ and $x = 0.34$). Interestingly, the AMR shows the same sign at opposite ends of the intercalation spectrum, in contrast to the switching, which shows opposite sign.

The role of the spin glass in mediating spin transfer torque interactions and the nature of the AFM phases in this system is not fully understood and is the subject of ongoing research [139]. Nevertheless, the intercalation dependence of switching in $Fe_{1/3}NbS_2$ provides a platform where one can precisely tune the material response for both exploring fundamental spin torque interactions and developing applied devices.

7.6 Conclusion and future prospects

Electronically accessible magnetic memory promises to dramatically improve device density, power dissipation, and read/write times in addition to being non-volatile. This has lead to a tremendous research effort and the production of the first commercial magnetoresistive random access memory (MRAM) chips. MRAM represents a significant step forward in

memory storage with the potential to be a "universal memory", providing the scalability and cost-effectiveness required for long-term data storage, as well as the write and read speeds required for on-chip caching.

MRAM, however, is built on the magnetic tunnel junction and the reorientation of ferromagnetic moments. The next leap forward in memory technology may come from encoding information into antiferromagnets instead, allowing for memory to become even faster, denser, and more robust. $Fe_{1/3}NbS_2$ would be a good candidate material for this application due to the low currents required for switching, and the single-pulse saturation of the response. There are, however, a few key challenges that would need to be overcome.

First, the device only operates below its AFM transition temperature of 42K. In order to be useful as a commercial technology, it will need to operate at room temperature. This will require a significant increase in the transition temperature. This may be achievable through carrier doping given that the AFM exchange energy is controlled by an RKKY interaction. In bulk crystals the carrier concentration may be tuned by chemical doping. In thin films, it may be done through electric field gating or by modifying lattice parameters through careful substrate selections. All of these methods have been used to tune the RKKY interaction strength in other compounds [140, 141].

Second, the $Fe_{1/3}NbS_2$ device presented here has a very low switching amplitude. There is only a few percent change in the resistance between the high and low states. In general, higher switching ratios make detection easier allowing for faster and lower-power readout operations. In the magnetic tunnel junction, high switching ratios are achieved through the incorporation of a tunneling barrier. A similar approach has been proposed for AFM memory devices [142, 143, 144]. In this case, the density of states will depend on the orientation of the AFM state, and therefore the tunneling probability will as well. As a result, small changes in the density of states from the reorientation of the AFM order can lead to large changes in the device resistance. Implementing $Fe_{1/3}NbS_2$ into similar tunneling heterostructures may similarly enhance the measured switching ratios.

If the room temperature operation and switching ratio shortcomings can be solved, then $Fe_{1/3}NbS_2$ is well-positioned to play an important role in future AFM spintronic devices. Even if these issues cannot be solved, however, $Fe_{1/3}NbS_2$ is just one compound in a much larger family of intercalated transition metal dichalcogenides. Many magnetic elements can be intercalated into these layered materials producing exotic magnetic phases that are just beginning to be explored. It is likely that some of these compounds may possess similar switching behaviors to $Fe_{1/3}NbS_2$ but may do so at higher temperatures, lower currents, or with larger switching ratios. This makes $Fe_{1/3}NbS_2$ a promising platform for realizing antiferromagnetic spintronics.

Chapter 8

Conclusion and Outlook

The results presented in this dissertation are an exploration of some of the emergent phenomena in the ever expanding field of quantum materials. These materials require a departure from the paradigm of single particle bandstructures and phase transitions defined only by symmetry. They have provided the research community with a new set of fundamental physical concepts to explore. Moreover, the new behaviors associated with these materials represent a new set of building blocks from which to build novel electronic devices.

Chapter 4 presented the first transport measurements of Fermi arc surface states using microstructured devices of Cd_3As_2. Since then, additional measurements of these states have been performed. Studies on nanoplate crystals grown through chemical vapor deposition explored the dependence of this orbit on carrier doping and found non-local behavior in the surface transport [145, 146]. In sufficiently thin samples, the Weyl orbit was found to undergo quantized transport in a version of the quantum Hall effect driven by Fermi arcs [147]. Fermi arcs have also been observed in other compounds such as TaAs, as discussed in Chapter 5. The observation of surface transport associated with the Fermi arcs is important for understanding the sometimes conflicting experimental reports on this compound. Moreover, inducing superconductivity in the presence of these Fermi arcs using the focused ion beam may be a promising route to realizing Majorana fermions in these materials. Majorana fermions are quasiparticle excitations which are their own antiparticles and are governed by non-abelian statistics, making them very useful for quantum computing applications.

Chapter 7 presented measurements on the antiferromagnet $Fe_{1/3}NbS_2$, which was found to be electronically switchable at surprisingly low current densities, forming a magnetic memory bit. The rotation of the Néel order via electrical currents writes information into the device, and the change in the anisotropic magnetoresistance reads it back out again. Combined with the ultrafast dynamics intrinsic to antiferromagnetic interactions, this makes $Fe_{1/3}NbS_2$ a promising platform for high speed, non-volatile memory storage applications. Since the initial discovery, the switching behavior in this compound has been explored as a function of iron concentration and an interesting interplay between the spin glass dynamics and the antiferromagnetic order has been observed [139]. This may lead to the discovery of new switching mechanisms in magnetic systems. Finally, $Fe_{1/3}NbS_2$ is part of a large

family of magnetically intercalated transition metal dichalcogenides that is only beginning to be explored. Some may show magnetic switching at even lower current densities or higher temperatures, or show new, unanticipated emergent behaviors.

Bibliography

[1] P. W. Anderson. "More Is Different". In: *Science* 177.4047 (1972), pp. 393–396. DOI: 10.1126/science.177.4047.393.

[2] Richard P. Feynman. "There's plenty of room at the bottom". In: *Engineering and Science* 23.5 (1960), pp. 22–36.

[3] Philip J. W. Moll et al. "Transport evidence for Fermi-arc-mediated chirality transfer in the Dirac semimetal Cd3As2". In: *Nature* 535.7611 (July 2016), pp. 266–270. DOI: 10.1038/nature18276.

[4] Nityan L. Nair et al. "Transport signatures of surface states in a Weyl semimetal". In: (Oct. 2018). arXiv: 1810.08600.

[5] Maja D Bachmann et al. "Inducing superconductivity in Weyl semimetal microstructures by selective ion sputtering". In: *Science Advances* 3.5 (May 2017), e1602983. DOI: 10.1126/sciadv.1602983.

[6] Nityan L. Nair et al. "Thermodynamic signature of Dirac electrons across a possible topological transition in ZrTe5". In: *Physical Review B* 97.4 (Jan. 2018), p. 041111. DOI: 10.1103/PhysRevB.97.041111.

[7] Nityan L. Nair et al. "Electrical switching in a magnetically intercalated transition metal dichalcogenide". In: *Nature Materials* (Nov. 2019). DOI: 10.1038/s41563-019-0518-x. eprint: 1907.11698.

[8] Charles Kittel. *Quantum Theory of Solids*. Second Rev. John Wiley & Sons, Inc., 1987. ISBN: 978-0-471-62412-7.

[9] A. A. Abrikosov. *Fundamentals of the theory of metals*. North Holland, 1988, p. 630. ISBN: 0486819019.

[10] Neil W. Ashcroft and N. David. Mermin. "Solid state physics". In: (1976), p. 826.

[11] K. V. Klitzing, G. Dorda, and M. Pepper. "New Method for High-Accuracy Determination of the Fine-Structure Constant Based on Quantized Hall Resistance". In: *Physical Review Letters* 45.6 (Aug. 1980), pp. 494–497. DOI: 10.1103/PhysRevLett.45.494.

[12] A. M. Kosevich I. M. Lifshitz. "On the theory of the de Haas-van Alphen effect for particles with an arbitrary dispersion law". In: *Dokl. Akad. Nauk SSSR* 96 (1954), p. 963.

[13] D. Shoenberg. *Magnetic oscillations in metals*. Cambridge: Cambridge University Press, 1984. ISBN: 9780511897870. DOI: 10.1017/CBO9780511897870.

[14] W. J. de Haas and P. M. van Alphen. "The dependence of the susceptibility of diamagnetic metals upon the field". In: *Proceedings of the Academy of Science of Amsterdam* 33 (1930), pp. 1106–1118.

[15] R. B. Dingle. "Some magnetic properties of metals II. The influence of collisions on the magnetic behaviour of large systems". In: *Proceedings of the Royal Society of London. Series A. Mathematical and Physical Sciences* 211.1107 (Mar. 1952), pp. 517–525. DOI: 10.1098/rspa.1952.0056.

[16] J. M. Kosterlitz and D. J. Thouless. "Long range order and metastability in two dimensional solids and superfluids. (Application of dislocation theory)". In: *Journal of Physics C: Solid State Physics* 5.11 (June 1972), pp. L124–L126. DOI: 10.1088/0022-3719/5/11/002.

[17] J M Kosterlitz and D. J. Thouless. "Ordering, metastability and phase transitions in two-dimensional systems". In: *Journal of Physics C: Solid State Physics* 6.7 (Apr. 1973), pp. 1181–1203. DOI: 10.1088/0022-3719/6/7/010.

[18] D. J. Thouless et al. "Quantized Hall Conductance in a Two-Dimensional Periodic Potential". In: *Physical Review Letters* 49.6 (Aug. 1982), pp. 405–408. DOI: 10.1103/PhysRevLett.49.405.

[19] F.D.M. Haldane. "Continuum dynamics of the 1-D Heisenberg antiferromagnet: Identification with the O(3) nonlinear sigma model". In: *Physics Letters A* 93.9 (Feb. 1983), pp. 464–468. DOI: 10.1016/0375-9601(83)90631-X.

[20] F. D. M. Haldane. "Nonlinear Field Theory of Large-Spin Heisenberg Antiferromagnets: Semiclassically Quantized Solitons of the One-Dimensional Easy-Axis Neel State". In: *Physical Review Letters* 50.15 (Apr. 1983), pp. 1153–1156. DOI: 10.1103/PhysRevLett.50.1153.

[21] B. Andrei Bernevig, Taylor L. Hughes, and S.-C. Zhang. "Quantum Spin Hall Effect and Topological Phase Transition in HgTe Quantum Wells". In: *Science* 314.5806 (Dec. 2006), pp. 1757–1761. DOI: 10.1126/science.1133734. eprint: 0611399 (cond-mat).

[22] M. Konig et al. "Quantum Spin Hall Insulator State in HgTe Quantum Wells". In: *Science* 318.5851 (Nov. 2007), pp. 766–770. DOI: 10.1126/science.1148047. eprint: 0710.0582.

[23] Bohm-Jung Yang and Naoto Nagaosa. "Classification of stable three-dimensional Dirac semimetals with nontrivial topology". In: *Nature Communications* 5.1 (Dec. 2014), p. 4898. DOI: 10.1038/ncomms5898. eprint: 1404.0754.

[24] Andrew C Potter, Itamar Kimchi, and Ashvin Vishwanath. "Quantum oscillations from surface Fermi arcs in Weyl and Dirac semimetals". In: *Nature Communications* 5 (Oct. 2014), p. 5161. DOI: 10.1038/ncomms6161.

[25] Zhijun Wang et al. "Dirac semimetal and topological phase transitions in A3Bi (A=Na, K, Rb)". In: *Physical Review B* 85.19 (May 2012), p. 195320. ISSN: 1098-0121. DOI: 10.1103/PhysRevB.85.195320. eprint: 1202.5636. URL: https://link.aps.org/doi/10.1103/PhysRevB.85.195320.

[26] Zhijun Wang et al. "Three-dimensional Dirac semimetal and quantum transport in Cd3As2". In: *Physical Review B* 88.12 (Sept. 2013), p. 125427. DOI: 10.1103/PhysRevB.88.125427.

[27] Xiangang Wan et al. "Topological semimetal and Fermi-arc surface states in the electronic structure of pyrochlore iridates". In: *Physical Review B* 83.20 (May 2011), p. 205101. DOI: 10.1103/PhysRevB.83.205101.

[28] Steven M. Girvin and Kun Yang. *Modern condensed matter physics*. Cambridge: Cambridge University Press, 2019, p. 697. ISBN: 9781107137394.

[29] Shin-Ming Huang et al. "A Weyl Fermion semimetal with surface Fermi arcs in the transition metal monopnictide TaAs class". In: *Nature Communications* 6.1 (Nov. 2015), p. 7373. DOI: 10.1038/ncomms8373.

[30] L. X. Yang et al. "Weyl semimetal phase in the non-centrosymmetric compound TaAs". In: *Nature Physics* 11.9 (2015), pp. 728–732. DOI: 10.1038/nphys3425. eprint: 1507.00521.

[31] B. Q. Lv et al. "Experimental Discovery of Weyl Semimetal TaAs". In: *Physical Review X* 5.3 (July 2015), p. 031013. DOI: 10.1103/PhysRevX.5.031013.

[32] N. Xu et al. "Observation of Weyl nodes and Fermi arcs in tantalum phosphide". In: *Nature Communications* 7.1 (Apr. 2016), p. 11006. DOI: 10.1038/ncomms11006.

[33] Su Yang Xu et al. "Discovery of a Weyl fermion state with Fermi arcs in niobium arsenide". In: *Nature Physics* 11.9 (Sept. 2015), pp. 748–754. DOI: 10.1038/nphys3437.

[34] Z. K. Liu et al. "Evolution of the Fermi surface of Weyl semimetals in the transition metal pnictide family". In: *Nature Materials* 15.1 (Jan. 2016), pp. 27–31. DOI: 10.1038/nmat4457.

[35] Thiti Taychatanapat et al. "Electrically tunable transverse magnetic focusing in graphene". In: *Nature Physics* 9.4 (Apr. 2013), pp. 225–229. DOI: 10.1038/nphys2549. eprint: 1301.1969.

[36] Jens Baringhaus et al. "Exceptional ballistic transport in epitaxial graphene nanoribbons". In: *Nature* 506.7488 (Feb. 2014), pp. 349–354. DOI: 10.1038/nature12952.

[37] P. J. W. Moll et al. "Evidence for hydrodynamic electron flow in PdCoO2". In: *Science* 351.6277 (Mar. 2016), pp. 1061–1064. DOI: 10.1126/science.aac8385.

[38] H. van Houten et al. "Coherent electron focusing with quantum point contacts in a two-dimensional electron gas". In: *Physical Review B* 39.12 (Apr. 1989), pp. 8556–8575. ISSN: 0163-1829. DOI: 10.1103/PhysRevB.39.8556.

[39] Gordon Moore. "Cramming More Components onto Integrated Circuits". In: *Electronics* 38.8 (1965), pp. 114–117.

[40] Philip J.W. Moll. "Focused Ion Beam Microstructuring of Quantum Matter". In: *Annual Review of Condensed Matter Physics* 9.1 (Mar. 2018), pp. 147–162. DOI: 10.1146/annurev-conmatphys-033117-054021.

[41] B. J. Ramshaw et al. "Quantum limit transport and destruction of the Weyl nodes in TaAs". In: *Nature Communications* 9.1 (Dec. 2018), p. 2217. DOI: 10.1038/s41467-018-04542-9. eprint: 1704.06944.

[42] Kenji Gamo et al. "Ion Beam Assisted Deposition of Metal Organic Films Using Focused Ion Beams". In: *Japanese Journal of Applied Physics* 23.Part 2, No. 1 (May 1984), pp. L293–L295. DOI: 10.1143/JJAP.23.L293.

[43] James F. Ziegler. "SRIM-2003". In: *Nuclear Instruments Methods in Physics Research Section B: Beam Interactions with Materials and Atoms* 219-220 (June 2004), pp. 1027–1036. DOI: 10.1016/j.nimb.2004.01.208.

[44] James F. Ziegler, M.D. Ziegler, and J.P. Biersack. "SRIM The stopping and range of ions in matter (2010)". In: *Nuclear Instruments Methods in Physics Research Section B: Beam Interactions with Materials and Atoms* 268.11-12 (June 2010), pp. 1818–1823. DOI: 10.1016/J.NIMB.2010.02.091.

[45] Arthur J. Rosenberg and Theodore C. Harman. "Cd3As2-A Noncubic Semiconductor with Unusually High Electron Mobility". In: *Journal of Applied Physics* 30.10 (Oct. 1959), pp. 1621–1622. DOI: 10.1063/1.1735019.

[46] Mazhar N Ali et al. "The Crystal and Electronic Structures of Cd3As2, the Three-Dimensional Electronic Analogue of Graphene". In: *Inorganic Chemistry* 53.8 (Apr. 2014), pp. 4062–4067. DOI: 10.1021/ic403163d.

[47] Tian Liang et al. "Ultrahigh mobility and giant magnetoresistance in the Dirac semimetal Cd3As2". In: *Nature materials* 14.3 (Mar. 2015), pp. 280–4. DOI: 10.1038/nmat4143.

[48] Madhab Neupane et al. "Observation of a three-dimensional topological Dirac semimetal phase in high-mobility Cd3As2". In: *Nature Communications* 5.1 (Sept. 2014), p. 3786. DOI: 10.1038/ncomms4786.

[49] Hemian Yi et al. "Evidence of Topological Surface State in Three-Dimensional Dirac Semimetal Cd3As2". In: *Scientific Reports* 4.1 (May 2014), p. 6106. DOI: 10.1038/srep06106.

[50] Sergey Borisenko et al. "Experimental Realization of a Three Dimensional Dirac Semimetal". In: (2014). DOI: 10.1103/PhysRevLett.113.027603.

[51] Sangjun Jeon et al. "Landau quantization and quasiparticle interference in the three-dimensional Dirac semimetal Cd3As2". In: *Nature Materials* 13.9 (June 2014), pp. 851–856. DOI: 10.1038/nmat4023. eprint: 1403.3446.

[52] I Crassee et al. "3D Dirac semimetal Cd3As2: A review of material properties". In: *Physical Review Materials* 2.12 (Dec. 2018), p. 120302. DOI: 10.1103/PhysRevMaterials.2.120302.

[53] L. P. He et al. "Quantum Transport Evidence for the Three-Dimensional Dirac Semimetal Phase in Cd3As2". In: *Physical Review Letters* 113.24 (Dec. 2014), p. 246402. DOI: 10.1103/PhysRevLett.113.246402.

[54] C.W.J. Beenakker and H. van Houten. "Quantum Transport in Semiconductor Nanostructures". In: *Solid State Physics*. Vol. 44. Academic Press, Jan. 1991, pp. 1–228. ISBN: 9780126077445. DOI: 10.1016/S0081-1947(08)60091-0.

[55] M. J. M. de Jong and L. W. Molenkamp. "Hydrodynamic electron flow in high-mobility wires". In: *Physical Review B* 51.19 (May 1995), pp. 13389–13402. DOI: 10.1103/PhysRevB.51.13389.

[56] T. J. Thornton et al. "Boundary scattering in quantum wires". In: *Physical Review Letters* 63.19 (Nov. 1989), pp. 2128–2131. DOI: 10.1103/PhysRevLett.63.2128.

[57] F. Arnold et al. "Chiral Weyl Pockets and Fermi Surface Topology of the Weyl Semimetal TaAs". In: *Physical Review Letters* 117.14 (Sept. 2016), p. 146401. DOI: 10.1103/PhysRevLett.117.146401. eprint: 1603.08846.

[58] Yan Sun, Shu-Chun Wu, and Binghai Yan. "Topological surface states and Fermi arcs of the noncentrosymmetric Weyl semimetals TaAs, TaP, NbAs, and NbP". In: *Physical Review B* 92.11 (Sept. 2015), p. 115428. DOI: 10.1103/PhysRevB.92.115428. eprint: 1508.06649.

[59] Hongming Weng et al. "Weyl semimetal phase in noncentrosymmetric transition-metal monophosphides". In: *Physical Review X* 5.1 (2015). DOI: 10.1103/PhysRevX.5.011029. eprint: 1501.00060.

[60] Hiroyuki Inoue et al. "Quasiparticle interference of the Fermi arcs and surface-bulk connectivity of a Weyl semimetal". In: *Science* 351.6278 (Mar. 2016), pp. 1184–1187. DOI: 10.1126/science.aad8766.

[61] Michael Binnewies et al. *Chemical Vapor Transport Reactions*. De Gruyter, Inc., 2012. ISBN: 9783110254648.

[62] Michael Binnewies, Marcus Schmidt, and Peer Schmidt. "Chemical Vapor Transport Reactions - Arguments for Choosing a Suitable Transport Agent". In: *Zeitschrift fur anorganische und allgemeine Chemie* 643.21 (Nov. 2017), pp. 1295–1311. ISSN: 00442313. DOI: 10.1002/zaac.201700055.

[63] Sukarno Ferreira, ed. *Advanced Topics on Crystal Growth*. InTech, Feb. 2013. ISBN: 978-953-51-1010-1. DOI: 10.5772/46151. URL: http://www.intechopen.com/books/advanced-topics-on-crystal-growth.

[64] Zhilin Li et al. "Weyl Semimetal TaAs: Crystal Growth, Morphology, and Thermodynamics". In: *Crystal Growth and Design* 16.3 (Mar. 2016), pp. 1172–1175. DOI: 10.1021/acs.cgd.5b01758.

[65] Natascia De Leo et al. "Thickness Modulated Niobium Nanoconstrictions by Focused Ion Beam and Anodization". In: *IEEE Transactions on Applied Superconductivity* 26.3 (Apr. 2016), pp. 1–5. DOI: 10.1109/TASC.2016.2542286.

[66] Martin Leijnse and Karsten Flensberg. "Introduction to topological superconductivity and Majorana fermions". In: *Semiconductor Science and Technology* 27.12 (Dec. 2012). DOI: 10.1088/0268-1242/27/12/124003. eprint: 1206.1736.

[67] Michael A. Nielsen and Isaac L. Chuang. *Quantum computation and quantum information*. Cambridge [u.a.]: Cambridge University Press, 2010, p. 676. ISBN: 9781107002173.

[68] M. H. Halloran et al. "Experimental Study of the Fermi Surfaces of Niobium and Tantalum". In: *Physical Review B* 1.2 (Jan. 1970), pp. 366–372. DOI: 10.1103/PhysRevB.1.366.

[69] M. G. Priestley et al. "De Haas-Van Alphen Effect and Fermi Surface in Arsenic". In: *Physical Review* 154.3 (Feb. 1967), pp. 671–682. DOI: 10.1103/PhysRev.154.671.

[70] Yongkang Luo et al. "Anomalous electronic structure and magnetoresistance in TaAs2". In: *Scientific Reports* 6.1 (July 2016), p. 27294. DOI: 10.1038/srep27294. eprint: 1601.05524.

[71] Yonghui Zhou et al. "Pressure-Induced New Topological Weyl Semimetal Phase in TaAs". In: *Physical Review Letters* 117.14 (Sept. 2016), p. 146402. DOI: 10.1103/PhysRevLett.117.146402.

[72] T Besara et al. "Coexistence of Weyl physics and planar defects in the semimetals TaP and TaAs". In: *Physical Review B* 93.24 (June 2016), p. 245152. DOI: 10.1103/PhysRevB.93.245152.

[73] Raman Sankar et al. "Crystal growth and transport properties of Weyl semimetal TaAs". In: *Journal of Physics: Condensed Matter* 30.1 (Jan. 2018), p. 015803. DOI: 10.1088/1361-648X/aa9a75.

[74] Mitsuru Suzuki, Hiroshi Bando, and Kokichi Oshima. "Phase Inversion of Shubnikov-de Haas Oscillation in Bismuth". In: *Japanese Journal of Applied Physics* 20.7 (July 1981), pp. 1323–1324. DOI: 10.1143/JJAP.20.1323.

[75] Naoki Satoh. "Anomalous Influence of a Small Amount of Impurities on the Shubnikov de Haas Oscillation Amplitude of Antimony". In: *Japanese Journal of Applied Physics* 37.Part 1, No. 1 (Jan. 1998), pp. 161–165. DOI: 10.1143/JJAP.37.161.

[76] Morrel H Cohen and L M Falicov. "Magnetic Breakdown in Crystals". In: *Physical Review Letters* 7.6 (Sept. 1961), pp. 231–233. DOI: 10.1103/PhysRevLett.7.231.

[77] M.I. Kaganov and A.A. Slutskin. "Coherent magnetic breakdown". In: *Physics Reports* 98.4 (Sept. 1983), pp. 189–271. DOI: 10.1016/0370-1573(83)90006-6.

[78] R W Stark and C. B. Friedberg. "Interfering electron quantum states in ultrapure magnesium". In: *Journal of Low Temperature Physics* 14.1-2 (Jan. 1974), pp. 111–146. DOI: 10.1007/BF00654814.

[79] N Harrison et al. "Magnetic breakdown and quantum interference in the quasi-two-dimensional superconductor in high magnetic fields". In: *Journal of Physics: Condensed Matter* 8.29 (July 1996), pp. 5415–5435. DOI: 10.1088/0953-8984/8/29/016.

[80] M V Kartsovnik et al. "Direct Observation of the Magnetic-Breakdown Induced Quantum Interference in the Quasi-Two-Dimensional Organic Metal κ(BEDT-TTF) 2CU(NCS)2". In: *Physical Review Letters* 77.12 (Sept. 1996), pp. 2530–2533. DOI: 10.1103/PhysRevLett.77.2530.

[81] Mark V. Kartsovnik. "High Magnetic Fields: A Tool for Studying Electronic Properties of Layered Organic Metals". In: *Chemical Reviews* 104.11 (Nov. 2004), pp. 5737–5782. DOI: 10.1021/cr0306891.

[82] Andras Gyenis et al. "Imaging electronic states on topological semimetals using scanning tunneling microscopy". In: *New Journal of Physics* 18.10 (Oct. 2016), p. 105003. DOI: 10.1088/1367-2630/18/10/105003.

[83] R.Y. Chen et al. "Magnetoinfrared Spectroscopy of Landau Levels and Zeeman Splitting of Three-Dimensional Massless Dirac Fermions in ZrTe5". In: *Physical Review Letters* 115.17 (Oct. 2015), p. 176404. DOI: 10.1103/PhysRevLett.115.176404.

[84] Qiang Li et al. "Chiral magnetic effect in ZrTe5". In: *Nature Physics* 12.6 (June 2016), pp. 550–554.

[85] Guolin Zheng et al. "Transport evidence for the three-dimensional Dirac semimetal phase in ZrTe5". In: *Physical Review B* 93 (11 Mar. 2016), p. 115414. DOI: 10.1103/PhysRevB.93.115414.

[86] Xiang Yuan et al. "Observation of quasi-two-dimensional Dirac fermions in ZrTe5". en. In: *NPG Asia Materials* 8.11 (Nov. 2016), e325. DOI: 10.1038/am.2016.166.

[87] Yanwen Liu et al. "Zeeman splitting and dynamical mass generation in Dirac semimetal ZrTe5". en. In: *Nature Communications* 7 (Aug. 2016), p. 12516. DOI: 10.1038/ncomms12516.

[88] Hongming Weng, Xi Dai, and Zhong Fang. "Transition-Metal Pentatelluride ZrTe5 and HfTe5: A Paradigm for Large-Gap Quantum Spin Hall Insulators". In: *Physical Review X* 4.1 (Jan. 2014), p. 011002. DOI: 10.1103/PhysRevX.4.011002.

[89] Zhi-Guo Chen et al. "Spectroscopic evidence for bulk-band inversion and three-dimensional massive Dirac fermions in ZrTe5". In: *Proceedings of the National Academy of Sciences* 114.5 (2017), pp. 816–821. DOI: 10.1073/pnas.1613110114.

[90] Xiang-Bing Li et al. "Experimental Observation of Topological Edge States at the Surface Step Edge of the Topological Insulator ZrTe5". In: *Physical Review Letters* 116.17 (Apr. 2016), p. 176803. DOI: 10.1103/PhysRevLett.116.176803.

[91] R. Wu et al. "Evidence for Topological Edge States in a Large Energy Gap near the Step Edges on the Surface of ZrTe5". In: *Physical Review X* 6.2 (May 2016), p. 021017. DOI: 10.1103/PhysRevX.6.021017.

[92] G. Manzoni et al. "Evidence for a Strong Topological Insulator Phase in ZrTe5". In: *Physical Review Letters* 117.23 (Nov. 2016), p. 237601. DOI: 10.1103/PhysRevLett.117.237601.

[93] L. Moreschini et al. "Nature and topology of the low-energy states in ZrTe5". In: *Physical Review B* 94.8 (Aug. 2016), p. 081101. DOI: 10.1103/PhysRevB.94.081101.

[94] Zongjian Fan et al. "Transition between strong and weak topological insulator in ZrTe5". In: *Scientific Reports* 7 (Apr. 2017), p. 45667. DOI: 10.1038/srep45667.

[95] Hang Chi et al. "Lifshitz transition mediated electronic transport anomaly in bulk ZrTe5". In: *New Journal of Physics* 19.1 (2017), p. 015005. DOI: 10.1088/1367-2630/aa55a3.

[96] J. L. Zhang et al. "Disruption of the Accidental Dirac Semimetal State in ZrTe5 under Hydrostatic Pressure". In: *Physical Review Letters* 118.20 (May 2017), p. 206601. DOI: 10.1103/PhysRevLett.118.206601.

[97] Jianwei Lu et al. "Thickness-tuned transition of band topology in ZrTe5 nanosheets". In: *Physical Review B* 95.12 (Mar. 2017), p. 125135. DOI: 10.1103/PhysRevB.95.125135.

[98] Philip J. W. Moll et al. "Magnetic torque anomaly in the quantum limit of Weyl semimetals". In: *Nature Communications* 7 (Aug. 2016), p. 12492. DOI: 10.1038/ncomms12492.

[99] Yuanbo Zhang et al. "Experimental observation of the quantum Hall effect and Berry's phase in graphene". en. In: *Nature* 438.7065 (Nov. 2005), pp. 201–204. DOI: 10.1038/nature04235.

[100] Laura M. Roth. "Semiclassical Theory of Magnetic Energy Levels and Magnetic Susceptibility of Bloch Electrons". In: *Physical Review* 145.2 (May 1966), pp. 434–448. DOI: 10.1103/PhysRev.145.434.

[101] Anthony R. Wright and Ross H. McKenzie. "Quantum oscillations and Berry's phase in topological insulator surface states with broken particle-hole symmetry". In: *Physical Review B* 87.8 (Feb. 2013), p. 085411. DOI: 10.1103/PhysRevB.87.085411.

[102] John Freserick Nye. *Physical Properties of Crystals: Their Representation by Tensors and Matrices*. Oxford: Oxford University Press, 1985. ISBN: 0198511655.

[103] Yan Zhang et al. "Electronic evidence of temperature-induced Lifshitz transition and topological nature in ZrTe5". en. In: *Nature Communications* 8 (May 2017), p. 15512. DOI: 10.1038/ncomms15512.

[104] Hongming Weng, Xi Dai, and Zhong Fang. "Transition-Metal Pentatelluride ZrTe5 and HfTe5: A Paradigm for Large-Gap Quantum Spin Hall Insulators". In: *Physical Review X* 4 (1 Jan. 2014), p. 011002. DOI: 10.1103/PhysRevX.4.011002.

[105] Kamil Olejnik et al. "Terahertz electrical writing speed in an antiferromagnetic memory". In: *Science Advances* 4.3 (Mar. 2018), eaar3566. DOI: 10.1126/sciadv.aar3566.

[106] Kevin Garello et al. "Ultrafast magnetization switching by spin-orbit torques". In: *Applied Physics Letters* 105.21 (Nov. 2014), p. 212402. DOI: 10.1063/1.4902443.

[107] T. Jungwirth et al. "Antiferromagnetic spintronics". In: *Nature Nanotechnology* 11.3 (Mar. 2016), pp. 231–241. DOI: 10.1038/nnano.2016.18. eprint: 1606.04284.

[108] J. Zelezny et al. "Spin transport and spin torque in antiferromagnetic devices". In: *Nature Physics* 14.3 (Mar. 2018), pp. 220–228. DOI: 10.1038/s41567-018-0062-7.

[109] D.C. Ralph and M.D. Stiles. "Spin transfer torques". In: *Journal of Magnetism and Magnetic Materials* 320.7 (Apr. 2008), pp. 1190–1216. DOI: 10.1016/j.jmmm.2007.12.019.

[110] Frances Hellman et al. "Interface-induced phenomena in magnetism". In: *Reviews of Modern Physics* 89.2 (June 2017), p. 025006. DOI: 10.1103/RevModPhys.89.025006.

[111] Chong Bi, Noriyuki Sato, and Shan X. Wang. *Advances in Non-Volatile Memory and Storage Technology*. Elsevier, 2019, pp. 203–235. ISBN: 9780081025840. DOI: 10.1016/C2017-0-02357-1.

[112] Alexander Makarov et al. "CMOS-compatible spintronic devices: a review". In: *Semiconductor Science and Technology* 31.11 (Nov. 2016), p. 113006. ISSN: 0268-1242. DOI: 10.1088/0268-1242/31/11/113006.

[113] Sabpreet Bhatti et al. "Spintronics based random access memory: a review". In: *Materials Today* 20.9 (Nov. 2017), pp. 530–548. ISSN: 13697021. DOI: 10.1016/j.mattod.2017.07.007.

[114] Helen V Gomonay and Vadim M Loktev. "Spin transfer and current-induced switching in antiferromagnets". In: *Physical Review B* 81.14 (Apr. 2010), p. 144427. DOI: 10.1103/PhysRevB.81.144427.

[115] H. Liu et al. "Dynamics of spin torque switching in all-perpendicular spin valve nanopillars". In: *Journal of Magnetism and Magnetic Materials* 358-359 (May 2014), pp. 233–258. DOI: 10.1016/j.jmmm.2014.01.061.

[116] J Zelezny et al. "Relativistic Neel-Order Fields Induced by Electrical Current in Antiferromagnets". In: *Physical Review Letters* 113.15 (Oct. 2014), p. 157201. DOI: 10.1103/PhysRevLett.113.157201.

[117] A Yu Silov et al. "Current-induced spin polarization at a single heterojunction". In: *Applied Physics Letters* 85.24 (Dec. 2004), pp. 5929–5931. DOI: 10.1063/1.1833565.

[118] Y K Kato et al. "Current-Induced Spin Polarization in Strained Semiconductors". In: *Physical Review Letters* 93.17 (Oct. 2004), p. 176601. DOI: 10.1103/PhysRevLett.93.176601.

[119] S. D. Ganichev et al. "Spin-galvanic effect". In: *Nature* 417.6885 (May 2002), pp. 153–156. DOI: 10.1038/417153a. eprint: 0204532 (cond-mat).

[120] P. Wadley et al. "Electrical switching of an antiferromagnet". In: *Science* 351.6273 (Feb. 2016), pp. 587–590. DOI: 10.1126/science.aab1031. eprint: 1503.03765.

[121] S Yu Bodnar et al. "Writing and reading antiferromagnetic Mn2Au by Neel spin-orbit torques and large anisotropic magnetoresistance". In: *Nature Communications* 9.1 (Dec. 2018), p. 348. DOI: 10.1038/s41467-017-02780-x.

[122] X. Z. Chen et al. "Antidamping-Torque Induced Switching in Biaxial Antiferromagnetic Insulators". In: *Physical Review Letters* 120.20 (May 2018), p. 207204. DOI: 10.1103/PhysRevLett.120.207204.

[123] Takahiro Moriyama et al. "Spin torque control of antiferromagnetic moments in NiO". In: *Scientific Reports* 8.1 (Dec. 2018), p. 14167. DOI: 10.1038/s41598-018-32508-w.

[124] R H Friend, A R Beal, and A D Yoffe. "Electrical and magnetic properties of some first row transition metal intercalates of niobium disulphide". In: *The Philosophical Magazine: A Journal of Theoretical Experimental and Applied Physics* 35.5 (May 1977), pp. 1269–1287. DOI: 10.1080/14786437708232952.

[125] Spencer Doyle et al. "Tunable Giant Exchange Bias in an Intercalated Transition Metal Dichalcogenide". In: *arXiv:1904.05872* (Apr. 2019). arXiv: 1904.05872.

[126] B Van Laar, H.M. Rietveld, and D.J.W. Ijdo. "Magnetic and crystallographic structures of MexNbS2 and MexTaS2". In: *Journal of Solid State Chemistry* 3.2 (May 1971), pp. 154–160. DOI: 10.1016/0022-4596(71)90019-3.

[127] O Gorochov et al. "Transport properties, magnetic susceptibility and Mossbauer spectroscopy of Fe0.25NbS2 and Fe0.33NbS2". In: *Philosophical Magazine B* 43.4 (Apr. 1981), pp. 621–634. DOI: 10.1080/01418638108222164.

[128] S. S. P. Parkin and R. H. Friend. "3d transition-metal intercalates of the niobium and tantalum dichalcogenides. I. Magnetic properties". In: *Philosophical Magazine B* 41.1 (Jan. 1980), pp. 65–93. DOI: 10.1080/13642818008245370.

[129] S S P Parkin and R H Friend. "3d transition-metal intercalates of the niobium and tantalum dichalcogenides. II. Transport properties". In: *Philosophical Magazine B* 41.1 (Jan. 1980), pp. 95–112. DOI: 10.1080/13642818008245371.

[130] Shan Wu. "Collinear to noncollinear canting magnetism in transition metal dichalcogenide Fe0.33NbS2". In: *Unpublished* (2019).

[131] T. McGuire and R. Potter. "Anisotropic magnetoresistance in ferromagnetic 3d alloys". In: *IEEE Transactions on Magnetics* 11.4 (July 1975), pp. 1018–1038. DOI: 10.1109/TMAG.1975.1058782.

[132] X. Marti et al. "Room-temperature antiferromagnetic memory resistor". In: *Nature Materials* 13.4 (Apr. 2014), pp. 367–374. DOI: 10.1038/nmat3861. eprint: 0402594v3.

[133] D Kriegner et al. "Multiple-stable anisotropic magnetoresistance memory in antiferromagnetic MnTe". In: *Nature Communications* 7.1 (Dec. 2016), p. 11623. DOI: 10.1038/ncomms11623.

[134] Arielle Little et al. "Observation of three-state nematicity in the triangular lattice antiferromagnet Fe1/3NbS2". In: (Aug. 2019). arXiv: 1908.00657.

[135] Y Togawa et al. "Chiral Magnetic Soliton Lattice on a Chiral Helimagnet". In: *Physical Review Letters* 108.10 (Mar. 2012), p. 107202. DOI: 10.1103/PhysRevLett.108.107202.

[136] Luis Seabra et al. "Phase diagram of the classical Heisenberg antiferromagnet on a triangular lattice in an applied magnetic field". In: *Physical Review B* 84 (2011), p. 214418. DOI: 10.1103/PhysRevB.84.214418.

[137] Satoshi Kokado and Masakiyo Tsunoda. "Anisotropic Magnetoresistance Effect: General Expression of AMR Ratio and Intuitive Explanation for Sign of AMR Ratio". In: *Advanced Materials Research* 750-752 (Aug. 2013), pp. 978–982. DOI: 10.4028/www.scientific.net/AMR.750-752.978.

[138] Sadamichi Maekawa et al. *Spin current*. Oxford: Oxford University Press, p. 541. ISBN: 0198787073.

[139] Eran Maniv et al. "Electrical Switching Driven by the Interplay of Order and Disorder". In: *Unpublished* (2019).

[140] Masakazu Matsubara et al. "Ultrafast optical tuning of ferromagnetism via the carrier density". In: *Nature Communications* 6 (Apr. 2015). DOI: 10.1038/ncomms7724.

[141] Qu Yang et al. "Ionic liquid gating control of RKKY interaction in FeCoB/Ru/FeCoB and (Pt/Co)2/Ru/(Co/Pt)2 multilayers". In: *Nature Communications* 9.1 (Dec. 2018). DOI: 10.1038/s41467-018-03356-z.

[142] B. G. Park et al. "A spin-valve-like magnetoresistance of an antiferromagnet-based tunnel junction". In: *Nature Materials* 10.5 (May 2011), pp. 347–351. DOI: 10.1038/nmat2983.

[143] T. Jungwirth et al. "Demonstration of molecular beam epitaxy and a semiconducting band structure for I-Mn-V compounds". In: *Physical Review B* 83.3 (Jan. 2011), p. 035321. DOI: 10.1103/PhysRevB.83.035321.

[144] A. B. Shick et al. "Spin-orbit coupling induced anisotropy effects in bimetallic antiferromagnets: A route towards antiferromagnetic spintronics". In: *Physical Review B* 81.21 (June 2010), p. 212409. DOI: 10.1103/PhysRevB.81.212409.

[145] Guolin Zheng et al. "Recognition of Fermi-arc states through the magnetoresistance quantum oscillations in Dirac semimetal Cd3As2". In: *Physical Review B* 96.12 (Sept. 2017), p. 121407. DOI: 10.1103/PhysRevB.96.121407.

[146] Cheng Zhang et al. "Evolution of Weyl orbit and quantum Hall effect in Dirac semimetal Cd3As2". In: *Nature Communications* 8.1 (Dec. 2017), p. 1272. DOI: 10.1038/s41467-017-01438-y.

[147] Cheng Zhang et al. "Quantum Hall effect based on Weyl orbits in Cd3As2". In: *Nature* 565.7739 (Jan. 2019), pp. 331–336. DOI: 10.1038/s41586-018-0798-3.